Thesis for the degree of Doctor of Philosophy

Periodized Thermal Greens Functions and Applications

Andro Sabashvili

Department of Physics
University of Gothenburg

September 2013

Front cover: contour plot of the periodized thermal Greens function.

ISBN 978-91-628-8766-7

Aidla Trading AB
Göteborg 2013

Periodized Thermal Greens Functions and Applications

Andro Sabashvili

Department of Physics
University of Gothenburg
SE-412 96 Göteborg, Sweden

Abstract

This work describes a new formalism for Fermionic thermal Greens functions that are discretized in imaginary time. The discretization makes the thermal Greens function periodic in imaginary (Matsubara) frequency space and requires a generalisation of the Dyson equation and Luttinger-Ward-Baym-Kadanoff functional. A Padé method is used to perform an analytic continuation of the periodized Matsubara Greens function to real frequencies which conserves the spectral weight and thus the discontinuity of the corresponding real time Greens function at $t = 0$. Due to the Matsubara Greens function periodicity, the discrete imaginary frequency space is relatively small which allows calculations at the extremely high precision which is necessary to perform a reliable Padé fit. We use the method to compute the single particle spectral function and energy loss function for doped bilayer graphene in the two-band limit, described by parabolic dispersion and Coulomb interaction. Calculations are performed in both the random phase approximation (RPA) and the fully self-consistent GW approximation. The formalism is also applied to dynamical mean field theory calculations using iterated perturbation theory (IPT) for the paramagnetic Hubbard model.

List of Papers

The thesis consists of an introductory text and the following three papers:

Paper I:
Dynamical mean field theory phase-space extension and critical properties of the finite temperature Mott transition, Hugo U. R. Strand, Andro Sabashvili, Mats Granath, Bo Hellsing, and Stellan Östlund, Phys. Rev. B 83, 205136 (2011)

Paper II:
Discretized Thermal Greens Functions M.Granath, A.Sabashvili, H.U.R.Strand, and S. Östlund, Ann. der Phys. 524, 147-152 (2012)

Paper III:
Bilayer graphene spectral function in the random phase approximation and self-consistent GW A.Sabashvili, S. Östlund, and M.Granath, arXiv:1301.3512, to be published in Phys. Rev. B.

Acknowledgments

This work has been done together with my supervisors Stellan Östlund and Mats Granath. I would like to express my gratitude to them for being encouraging and inspiring throughout this project.

It is a great pleasure to thank Gia Japaridze and Henrik Johannesson for their support.

Lastly, I wish to thank my family and friends.

To Ellene and Maggie

Contents

Chapter 1

Introduction

1.1 Paramagnetic Hubbard Model

The physics of strongly correlated Fermion systems plays a major role in the studies of various types of materials such as heavy Fermion compounds and high - temperature superconductors. Systems in which Fermion-Fermion interactions are comparable to or larger than the kinetic energy effectively are called strongly correlated Fermion systems.

These systems are connected to many unsolved issues because of the nonperturbative nature of the problem and the presence of interplay between quantum and spatial fluctuations and various competing long-range order. We can treat these types of systems exactly only in special cases such as certain one dimensional systems.

One of the problems which require a nonperturbative approach is the correlation-induced Mott metal-insulator transition that can occur when the potential and kinetic energies are of the same order. According to Mott, an electron-electron interaction can make a periodic crystal insulating even if the number of electrons is such that its energy bands are half-filled [1]. His proposition is now believed to explain the insulating behavior of many materials, in particular transition-metal oxides like NiO, MnO, and CoO. In those systems the effect of the Coulomb interaction is more pronounced than in conventional metals because electrons are more confined at the lattice sites and spatial fluctuations are suppressed.

The electrons in such a Mott insulator are localized at the atoms in the lattice. The excitations create or annihilate a local charge and require a certain minimum energy to overcome the Coulomb interaction. The typical spectrum of the Mott insulator thus consists of broad peaks well separated from the Fermi energy, which are called the Hubbard bands.

Usually we study model Hamiltonians that provide a very simplified description in terms of as few as possible relevant degrees of freedom and effective interactions. The minimal model that takes electron-electron interactions into account in crystals is the Hubbard model [2] which takes only one orbital per atom into account. All other orbitals can be imagined to be inaccessibly high in energy or otherwise are completely filled and have no influence on the physics of the valence band apart from screening the long range Coulomb interaction to an effective short range interaction. The model is fully specified only by the

number of electrons per lattice site, the Hubbard interaction and the hopping amplitudes that determine the overlap between the atomic orbitals and thus the band structure in the noninteracting case.

In spite of all these simplifications, the Hubbard model can not, in general, be solved analytically and numerical result require large computational effort even for very small systems. Some insights into the model can be obtained from the limits of either large or small effective Coulomb interaction for the square lattice in 2D. In both limits the ground state is antiferromagnetically ordered and insulating, but other properties, in particular the properties of the paramagnetic phase, are quite different.

Many approximation schemes and numerical methods have been developed to overcome the difficulties related to the strongly correlated systems. One of them is dynamical mean field theory (DMFT) [3], which has been developed in the '90s and made an important contribution to the investigation of strongly correlated electron systems. The idea is to map a lattice model onto a *single-site* quantum impurity surrounded by a *"bath"* (effective medium). This results in a single impurity Anderson model (SIAM) with parameters that have to be determined self-consistently. SIAM has been studied intensively and several technical tools are available to treat this problem.

This approximation is in a sense a generalization of mean-field theory, where not all fluctuations are eliminated. Only spatial fluctuations are frozen out, while the local quantum fluctuations (i.e. fluctuations between all possible quantum states on the lattice site) are fully taken into account and treated in a nonperturbative manner, which is an advantage for this method compare to the other approximations where *all* types of fluctuations are disregarded. Hence, the main difference compare to ordinary mean-field is that the on-site quantum problem is still a many-body problem. For this reason, the term "Dynamical mean-field theory" is used to describe this approach.

For the Hubbard model DMFT in fact predicts a first order transition from paramagnetic metal to paramagnetic insulator which ends in a second order finite temperature critical end point above which there is only a smooth crossover between metal and insulator. DMFT is also exact in the limit of large lattice coordination $d = \infty$ [4]. However, the method can be applied to more realistic models, taking into account the lattice structure and density of states. The limit of large coordination number allows us to test numerical methods and then use them for finite dimensional cases as an approximation. The dynamical mean field approach assumes that one should solve, so called, dynamical mean field equations self-consistently. The DMFT equations are conveniently written in terms of Greens functions defined in the imaginary Matsubara frequency space, which are Fourier forms of the imaginary time (thermal) Greens functions. A finite temperature Greens function is the key object in many-body physics and characterizes a wide range of experimentally accessible observables. Many numerical techniques have been used to solve DMFT equations: quantum Monte Carlo, exact diagonalization, iterative perturbation scheme (IPT), etc.

Self-consistent calculations (e.g. solving the DMFT equations) using imaginary time Greens functions are very difficult because a large number of discretization points is required to capture the characteristics of the thermal Greens function. Also, the convergence of the Greens function and self-energy becomes slow as the number of discretization points increases.

Solving the DMFT equations yields the Greens function and self-energy as

functions of the imaginary Matsubara frequencies, but physical observables are calculated using the real time (real frequency) Greens functions. Thus, another numerical problem emerges: performing an analytic continuation of the imaginary time (imaginary frequency) Greens function from the imaginary time (imaginary frequency) axis to the real time (real frequency) axis. Since we only know the Greens function values at the finite set of the Matsubara frequencies it is not obvious to do the analytic continuation numerically.

A widely used technique to handle this problem is a Padé approximant method [5], [6][1] in which ratios of polynomials or terminating continued fractions are used as the fitting functions. There are several Padé schemes which can be divided into two broad classes: (1) Those that return the value of the continued function point by point in the complex plane and (2) Those that yield the function itself by returning the polynomial (or continued fraction) coefficients. In this thesis a Padé scheme from the second class is used. The advantage of this scheme is that the problem is formulated as a matrix equation allowing us to use efficient routine for matrix inversion. The commonly used Padé method, which belongs to the first class, is a recursive algorithm called Thiele's Reciprocal Difference Method [5]. It is effective because it can be used to directly calculate the value of the approximant at a given point without computing the polynomial coefficients. Although the disadvantage of the latter is that a naively implemented recursion algorithm can lead to a propagation of an error since repeated operations are performed on the terms of very different orders of magnitude. Both Padé method are ill posed in a sense that it is extremely dependent on the accuracy of the original data. If the input data is not accurate enough it can lead to the non physical results.Therefore the Padé procedure can be carried out with high precision data. The required precision depends on the temperature and order of the polynomials.

This thesis describes a new approach to the Fermionic thermal Greens functions which can treat the numerical problems related to the discontinuity and analytic continuation of the Fermionic thermal Greens functions. By discretizing the imaginary time $\tau \in [0, \beta]$ into N evenly spaced points and performing a discrete Fourier transform to the Matsubara frequency space a periodic and N dimensional imaginary frequency Greens functions is obtained. The formalism describes how to appropriately work with such a periodized Greens function. The basic demands fulfilled by the method presented in the thesis are: the limit $N \to \infty$ gives standard formalism of the thermal Greens functions, for all values of N the Greens function obeys proper Luttinger-Ward variational principle, the free energy is exact in the non interacting limit and the analytic continuation provides the discontinuity in the real time space which is related to conservation of spectral weight. Using DMFT-IPT (see Chapter 8) approach written in terms of the periodized Greens functions we explore the Mott metal-insulator transition and calculate second order critical end-point for infinite dimensional paramagnetic Hubbard model at half-filling. The analytic continuation of the periodized Matsubara frequency Greens function is performed by means of the Padé method and spectral functions for both metallic and insulating phases are obtained. The results are presented in Chapter 8 and Papers I and II. The formalism itself is presented in Paper II.

[1] There are some other methods e. g. maximum-entropy method [7].

1.2 Single and Bi-layer Graphene

Since its fabrication, graphene [8, 9, 10, 11, 12] (a single layer of graphite) has been of interest for both theoreticians and experimentalists. Due to its unique property of high mobility even in highly doped cases it opens new perspectives for engineering and is a candidate material for future nanoelectronic and spintronic devices. For instance, observed mobilities turn out to be weakly dependent on the temperature causing ballistic transport on a micrometer scale at room temperature which enables a room-temperature ballistic transistors. Since the nanoscale structures made of graphene are stable one can use graphene as a conductive sheet and carve out conducting channels, quantum dots, nano-size structures to make single-electron transistor. The disadvantage of most materials is their instability at nanoscale [13], whereas graphite permits the creation of stable nanoscale structures.

In the low energy limit graphene is described by Lorentz invariant relativistic Hamiltonian for massless Fermions from quantum electro dynamics [14]. Thus graphene is a good candidate to test the quantum field theoretical models. The difference between graphene theory and true relativistic theory is that in the case of graphene the massless Fermions move with speed $v_F \approx 10^6 m/s$ which is 300 times smaller than the speed of light. In addition, from the point od view of external observer graphene, as a whole, is galilean invariant and non-relativistic because v_F is much smaller than the speed of light.

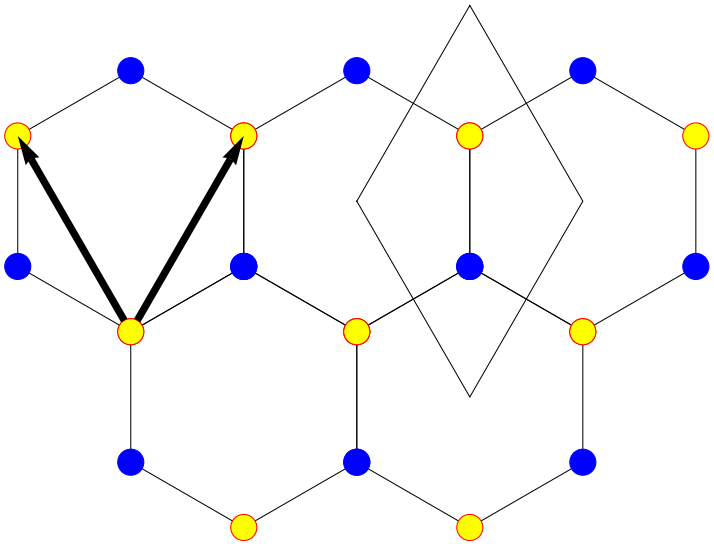

Figure 1.1: Monolayer graphene lattice structure. Blue and yellow dots denote carbon atoms residing on the different triangular sublattices.

Building block of graphene is carbon atom which is a constituent of most organic molecules therefore is responsible for life on Earth. It consists of six protons, six electrons and depending and depending on the number of neutrons in the nucleus there are different isotopes of carbon in nature. The stable isotopes have six or seven neutrons in the nucleus. The isotope with six neutrons

is wide spread in the nature than the one with seven neutrons. There is also another isotope of carbon with eight neutrons which is radioactive and used for dating.

The electron configuration for carbon atom in its ground state is $1s^2 2s^2 2p^2$. The $1s$ orbital is filled with two electrons and has the smallest energy thus it is irrelevant for chemical reactions. To get the first excited state an electron from $2s$ orbital is excited to the $2p$ orbital which has higher energy than $2s$ orbital. So it is not favorable for the system to have just one electron on $2s$ orbital. In the presence of another carbon atoms the system gains in energy by exciting an electron from $2s$ to $2p$ orbital which then forms covalent bond with other atoms. Therefore in the excited carbon atom there are four states $|2s\rangle, |2p_x\rangle, |2p_y\rangle$ and $|2p_z\rangle$. A superposition of $|2s\rangle$ and $|2p_j\rangle$ $(j = x, y, z)$ states is called sp hybridization. In particular, the hybridization between $|2s\rangle$ and one $|2p_j\rangle$, say $j = x$, is called sp^1 hybridization which forms strong σ bond after overlapping by another sp^1 orbital from neighboring atom. The rest of the unhybridized $|2p\rangle$ orbitals are free and form much weaker π orbitals. In the case of sp^2 hybridization, which takes place in graphene and other graphitic allotropes, $|2s\rangle$ state is in the superposition with two $|2p_j\rangle$ states forming σ bonds and the remaining $2p$ orbital, say $|2p_z\rangle$, overlaps with other orbital from neighboring carbon atom leading to the formation of π bands. Due to the strong σ bonds the lattice structure in all graphitic allotropes are robust. The σ bands are completely filled thus create a deep valence band. Since $|2p_z\rangle$ has jus one electron instead of two π band is half-filled.

One of the allotropes is the graphite, stack of graphene layers coupled by van der Waals force which is much weaker than the in-plane bonding. Due to this interlayer weak coupling we are able to draw a line by pressing a pencil against paper sheet. The first theoretical model for graphite was introduced by McClure [11], Slonczewski and Weiss [15] wich describes electronic properties of the material.

Other graphitic allotropes are Fullerenes [16] and nanotubes [17]. Fullerene was discovered in 1985. It consists of graphene sheet with some of the hexagons being replaced by pentagons which causes the crumbling of the sheet and thus fullerenes have spherical form. So, it can be viewed as wrapped up graphene sheet. Carbon nanotubes can be considered as rolled up graphene sheet along a given direction. It has only hexagons and can be thought of as a one-dimensional physical system.

In sp^3 hybridization $2s$ orbital is mixed with all three $2p$ orbitals. This hybridization is realized in diamonds. Despite the fact that both graphite and diamond consist of carbon atoms their physical properties are extremely different. Graphite, as I already mentioned, is soft material while diamond is one of the hardest materials in nature because all bonds in the crystal are strong σ bonds. Since all four electrons in the outer shell of the sp^3 hybridization participate in formation of the σ bands diamond is insulator whereas electrons in π bands of graphite are delocalized and thus provide good conductance properties.

Single sheet of graphene is a two-dimensional crystal and consists of carbon atoms arranged in a hexagonal lattice, Fig. 1.1. In general, a honeycomb lattice is not a Bravais lattice in a sense that the views from white and black dots, representing each sublattice, are not identical. The view from, say white dots, is the view from black dots rotated by 60 degrees. Hence there are two sets of Bravais lattice generators and each forms triangular lattice, A sublattice - blue

dots, B sublattice - yellow dots. The Bravais lattice vectors for B sublattice is shown on Fig. 1.1 with black arrows. There are two carbon atoms in the unit cell (see rhombus Fig. 1.1).

Bilayer graphene consists of two graphene monolayers weekly coupled by interlayer hopping.It is an intermediate material between single layer graphene and graphite. There are different ways of stacking two graphene layers, but this work considers so called Bernal stacking which means that the layers are rotated by 60 degrees relative to each other. In the case of the Bernal stacking, one of the sublattices (say, sublattice A) in the upper plane sits on top of the another sublattice (sublattice B) in the lower plane. The lattice of the bilayer graphene in real space is presented in Fig. 1.2.

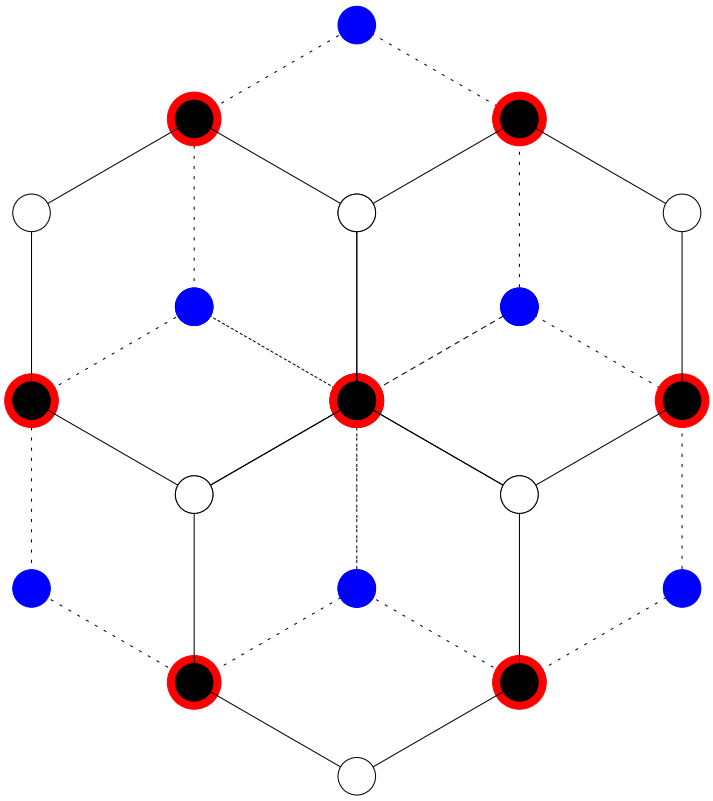

Figure 1.2: Bilayer graphene lattice structure. White (sublattice A) and black (sublattice B) dots belong to the upper plane whereas blue (sublattice B) and red (sublattice A) ones belong to the lower plane.

Bilayer graphene shares some features with both graphene and the ordinary two-dimensional electronic gas (2DEG). Its dispersion is quadratic, similar to a 2DEG but the effective Hamiltonian is chiral with zero band gap as in the case of graphene [18, 19]. In both single layer and bilayer graphene the charge carrier density can be controlled by application of a gate voltage, a fundamental effect for potential technological applications [20, 8]. In addition, for bilayer graphene even the band gap is tunable with great potential for device applications [20, 21].

Apart from the dispersion relation, the property which makes bilayer graphene different from that of a single layer is its coupling parameter being a function of the carrier density $r_s \sim n^{-1/2}$ [22, 9]. In other words the strength of Coulomb interaction is tunable, while the coupling parameter for the single layer graphene is constant $r_s \sim n^0$ and lies in the interval $0 \leq r_s \lesssim 2.2$. By comparing the values of r_s for single- and bilayer graphene ($r_s \approx 68.5 \times / \sqrt{n/10^{10} cm^{-2}}$, where n is the number of carriers per cm^{-2} with $n \approx 10^9 - 5 \times 10^{12}$ cm^{-2}) in vacuum it is clear that the strength of the Coulomb interaction can be much larger in bilayer graphene [9].

The periodized Greens function method was implemented to study the electronic structure of doped bilayer graphene in the low energy two-band limit in the fully self-consistent GW and random phase approximation (RPA) (see Chapter 7 and Paper III).

1.3 Outline

The structure of the thesis is presented below: In Chapter 2 the single-particle Fermionic real and imaginary time Greens functions are introduced. First, their definitions and properties are presented. Then using the definition an analytic expression for the non-interacting thermal Greens function is obtained in the imaginary time space. The expression for the Greens function in the imaginary (Matsubara) frequency space is derived after defining Fourier transformation from imaginary time to the frequency space and vice versa.

Chapter 3 covers analytic properties of the finite temperature (thermal) Greens functions. Since the physical quantities can be calculated by means of the real time Greens functions one has to do an analytic continuation from the imaginary time axis to the real time axis. In order to describe the real and imaginary time Greens functions, a Greens function with the complex argument is introduced. The real frequency Greens function is derived as the Fourier transformation of the real time Greens function and retarded and advanced Greens functions are defined. After that the Greens functions is written in the spectral representation using a spectral weight function. The relations between the retarded Greens function, advanced Greens function and spectral weight are also shown. The conservation of the total spectral weight and its relation to the Greens function discontinuity at the boundary in imaginary time space is presented.

Chapter 4 describes how the discretized thermal Greens function results in a periodized Greens function in the Matsubara frequency space. First, the calculations are done for the non-interacting limit and then the expression for the full periodized Greens function is derived. It is also shown that in the limit of infinitely large number of frequencies the standard expressions are recovered.

In Chapter 5 a Luttinger-Ward functional and variational principle is introduced followed by more general version written in terms of the periodized Greens functions which reduces to the former as the number of frequencies tends to infinity. It is shown for both the standard Luttinger-Ward functional and the one written in terms of the periodized Greens functions that the variational principle yields the proper Dyson equation and the free energy corresponds to the stationary point of the corresponding Luttinger-Ward functional. In the end of the chapter, particle number and the expectation value of the Hamiltonian

are derived using periodized and non periodized Luttinger-Ward functionals.

Chapter 6 describes an analytic continuation of the periodized Greens functions in analogy with the standard formalism covered in Chapter 2. The spectral weight expression and spectral representation of the Greens function is introduced. Then retarded and advanced Greens functions are defined in analogy with the standard formalism and all relations presented in Chapter 2 are rederived in the case of the periodized Greens functions, which yield standard expressions in the case of infinitely large number of frequencies. Then the spectral function is modeled by the sum of the "periodized Lorentzians" and the analytic expression for the Greens function is derived. Next, the transformation of the basis is done in order to rewrite the Greens function as the sum of the simple poles followed by a Padé fit description which is necessary to find unknown parameters contained in the analytic Greens function.

The introduction to mono and bilayer graphene, GW approximation, random phase approximation and the results for the bilayer graphene are covered in Chapter 7.

The results, obtained by applying our periodized Greens function formalism to the DMFT-IPT method to the half-filled paramagnetic Hubbard model are presented in Chapter 8.

The last chapter is the summary of the thesis.

Chapter 2

Greens Functions

Since we will be generalising many properties of the Greens functions it is instructive to start with reviewing of the basic finite temperature Greens function theory. Let us define $c_\alpha(t)$ and $c^\dagger_\alpha(t)$ to be Fermion annihilation and creation operators in the Heisenberg representation. Then the single-particle, Fermionic, real time Greens function is defined by [23]

$$G_{\alpha,\beta}(t-t') = -i\langle Tc_\alpha(t)c^\dagger_\beta(t')\rangle = -i\frac{1}{Z}Tr(e^{-\beta H}Te^{iHt}c_\alpha e^{-iHt}e^{iHt'}c^\dagger_\beta e^{-iHt'}) \tag{2.1}$$

T is time ordering, Tr - the sum over a complete set of states, β - inverse temperature, Z is the partition function $Z = Tr(e^{-\beta H})$. The brackets denote a thermal average. We can set t' to be zero because the Greens function depends only on the difference of t and t'. Since the real and imaginary times appear simultaneously in Eq. 2.1, it is useful to define the imaginary time or thermal Greens function because it can be written in terms of the well known imaginary time path integral and perturbation theory can be applied to evaluate thermal averages. Using this we are able to compute physical observables by doing an analytic continuation to the real time Greens function. Let "k" denote a complete set of quantum numbers that label the single particle state $|k\rangle$. The Fermionic, single particle, imaginary time Greens function is defined in the following way:

$$G_{k,k'}(\tau) = -\langle Tc_k(\tau)c^\dagger_{k'}(0)\rangle = -\frac{1}{Z}Tr(e^{-\beta H}e^{H\tau}c_k e^{-H\tau}c^\dagger_{k'}) \tag{2.2}$$

where $c_k(\tau)$ is in the imaginary time Heisenberg representation

$$c_k(\tau) = e^{H\tau}c_k e^{-H\tau}$$

$$c^\dagger_k(\tau) = e^{H\tau}c^\dagger_k e^{-H\tau}$$

Using the definition of the time ordering T one obtains:

$$G_{k,k'}(\tau) = \begin{cases} G_k^{>}(\tau) \equiv -\langle c_k(\tau) c_k^{\dagger}(0)\rangle & \tau > 0 \\ G_k^{<}(\tau) \equiv \quad \langle c_k^{\dagger}(0) c_k(\tau)\rangle & \tau < 0 \end{cases}$$

We note that (k index is dropped in the following expressions)

$$\begin{aligned} G^{>}(\tau) &= -\frac{1}{Z} Tr(e^{-\beta H} e^{H\tau} c e^{-H\tau} c^{\dagger}) \\ &= -\frac{1}{Z} Tr(e^{(\tau-\beta)H} c e^{(\beta-\tau)H} e^{-\beta H} c^{\dagger}) \\ &= -\frac{1}{Z} Tr(e^{-\beta H} c^{\dagger} e^{(\tau-\beta)H} c e^{(\beta-\tau)H}) \\ &= -\langle c^{\dagger}(0) c(\tau-\beta)\rangle \\ &= -G^{<}(\tau-\beta) \end{aligned}$$

As we see from the last equality, the Fermionic Greens function is anti-periodic with the period of β inside the domain $-\beta < \tau < \beta$, but it is periodic with the period of 2β.

Since the Greens function is anti-periodic one can define a Fourier transformation from the imaginary time to the frequency space and vice versa:

$$G(i\omega_n) = \int_0^{\beta} d\tau\, G(\tau) e^{i\omega_n \tau} \tag{2.3}$$

$$G(\tau) = \frac{1}{\beta} \sum_{n=-\infty}^{n=\infty} G(i\omega_n) e^{-i\omega_n \tau} \tag{2.4}$$

where ω_n is, the so called, Matsubara frequency defined as $\omega_n = \pi(2n+1)/\beta$, n is an integer. Such definition of the Matsubara frequencies is caused by the anti-periodicity of the Greens function , $G(-\tau) = -G(\beta - \tau)$.

In general, thermal Greens function does not have a simple form. Let us derive an explicit form of the simplest, non interacting Greens function,

$$\begin{aligned} G_0^{>}(\tau) &= -\langle c(\tau) c^{\dagger}\rangle \\ &= -\langle e^{H_0\tau} c\, e^{-H_0\tau} c^{\dagger}\rangle \\ &= -\langle e^{-\epsilon\tau} c\, c^{\dagger}\rangle \\ &= -e^{-\epsilon\tau}(1-n_f) \\ &= e^{-\epsilon\tau}(n_f - 1), \end{aligned}$$

where $H_0 = \epsilon c^\dagger c$ is the free-particle Hamiltonian, n_f represents Fermi-Dirac distribution, $n_f = 1/(e^{\beta\epsilon} + 1)$ and the following expression for $c(\tau)$ was used:

$$c(\tau) = e^{H_0\tau} c\, e^{-H_0\tau}$$

$$\frac{dc}{d\tau} = H_0 e^{H_0\tau} c\, e^{-H_0\tau} - e^{H_0\tau} c\, H_0\, e^{-H_0\tau}$$

$$\frac{dc}{d\tau} = e^{H_0\tau}[H_0, c] e^{-H_0\tau}$$

$$\frac{dc}{d\tau} = -\epsilon c(\tau)$$

$$c(\tau) = e^{-\epsilon\tau} c,$$

In the same manner $G_0^<(\tau)$ gives:

$$\begin{aligned} G_0^<(\tau) &= \langle c^\dagger(0) c(\tau)\rangle \\ &= \langle c^\dagger e^{H_0\tau} c\, e^{-H_0\tau}\rangle \\ &= \langle c^\dagger e^{-\epsilon\tau} c\rangle \\ &= e^{-\epsilon\tau} n_f \end{aligned}$$

By combining the last two results one gets

$$G_0(\tau) = e^{-\epsilon\tau}[(n_f - 1)\theta(\tau - 0^+) + n_f\theta(-\tau + 0^+)] \tag{2.5}$$

Eq. 2.5 shows that the Greens function has a discontinuity at $\tau = 0$ and the limits $\tau \to 0^-$and $\tau \to 0^+$ are not equal to each other. The Greens function is usually defined to be equal to the particle number n_f exactly at $\tau = 0$ [23]. To capture that feature infinitesimal quantity 0^+ is incorporated in the expression of $G_0(\tau)$.

The Fourier representation of the non interacting Greens function can be computed as:

$$\begin{aligned} G_0(i\omega_n) &= \int_0^\beta d\tau G_0(\tau) e^{i\omega_n\tau} \\ &= \int_0^\beta d\tau e^{i\omega_n\tau} e^{-\epsilon\tau}[(n_f - 1)\theta(\tau) + n_f\theta(-\tau)] \end{aligned}$$

$$= \frac{e^{\beta(i\omega_n-\epsilon)}-1}{i\omega_n-\epsilon}(n_f-1)$$

$$= \frac{-e^{-\beta\epsilon}-1}{i\omega_n-\epsilon}\frac{-e^{\beta\epsilon}}{e^{\beta\epsilon}+1}$$

$$= \frac{1}{i\omega_n-\epsilon}$$

Since the measure of the $\tau = 0$ point is zero the definition of the discontinuity at $\tau = 0$ does not affect the integral.

Let us now carry out the Fourier transformation from frequency to imaginary time:

$$G_0(\tau-0^+) = \frac{1}{\beta}\sum_{n=-\infty}^{\infty}\frac{e^{-i\omega_n(\tau-0^+)}}{i\omega_n-\epsilon} \tag{2.6}$$

Using standard contour integral technique Eq. 2.6 can be represented by:

$$I = \oint_C \frac{dz}{2\pi} f(z)h(z)$$

$$f(z) = \frac{1}{i}\frac{e^{-z(\tau-0^+)}}{e^{\beta z}+1}$$

$$h(z) = \frac{1}{z-\epsilon}$$

Function $f(z)$ has an infinite set of poles exactly at the Matsubara frequencies: $e^{\beta z}+1 = 0 \Rightarrow z = i\pi(2n+1)/\beta \equiv i\omega_n$. Function $h(z)$ has the pole at $z = \epsilon$. By assuming that τ is negative or zero (remember that τ ranges form $-\beta$ to β) and choosing contour C to encircle all poles of the function $f(z)$ in the negative (clockwise) direction one can show that the integral I yields Eq. 2.6:

$$\begin{aligned} I &= -2\pi i\frac{1}{2\pi}\sum_{n=-\infty}^{\infty} res(f(z)h(z)) \\ &= -\sum_{n=-\infty}^{\infty}\lim_{z\to i\omega_n}\frac{z-i\omega_n}{e^{\beta z}+1}\frac{e^{-z(\tau-0^+)}}{z-\epsilon} \\ &= -\sum_{n=-\infty}^{\infty}(-\frac{1}{\beta})\frac{e^{-i\omega_n(\tau-0^+)}}{i\omega_n-\epsilon} \\ &= \frac{1}{\beta}\sum_{n=-\infty}^{\infty}\frac{e^{-i\omega_n(\tau-0^+)}}{i\omega_n-\epsilon} \end{aligned}$$

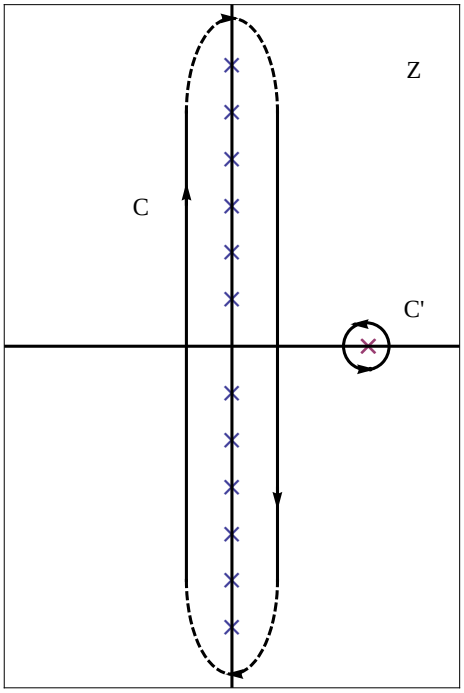

Figure 2.1: Blue crosses (Matsubara frequencies $z = i\omega_n$) represent poles for $f(z)$. A red one ($z = \epsilon$) is the pole for $h(z)$

On the other hand, since $zf(z)h(z) \to 0$ as $|z| \to \infty$ one can replace the contour C by the contour C' which encircles the pole of $h(z)$ in the positive (counterclockwise) direction (see Fig. 2.1). As one can see the factor e^{z0^+} in $f(z)$ ensures that this condition is fulfilled at $\tau = 0$. Replacing the contour C by C' yields:

$$\begin{aligned} I &= \oint_{C'} \frac{dz}{2\pi} f(z)h(z) \\ &= 2\pi i \frac{1}{2\pi} \sum_{n=-\infty}^{\infty} res(f(z)h(z)) \\ &= \lim_{z\to\epsilon} \frac{z-\epsilon}{z-\epsilon} \frac{e^{-z(\tau-0^+)}}{e^{\beta z}+1} \\ &= \frac{e^{-\epsilon(\tau-0^+)}}{e^{\beta\epsilon}+1} \\ &= e^{-\epsilon(\tau-0^+)} n_f \end{aligned}$$

To carry out the same procedure for positive τ-values we define $f(z)$ to be $e^{-z\tau}/(ie^{-\beta z}+i)$ and the contours C and C' should be positively and negatively

oriented, respectively.

$$\begin{aligned} I &= \oint_{C'} \frac{dz}{2\pi} f(z)h(z) \\ &= -2\pi i \frac{1}{2\pi} \sum_{n=-\infty}^{\infty} res(f(z)h(z)) \\ &= -\lim_{z\to\epsilon} \frac{z-\epsilon}{z-\epsilon} \frac{e^{-z\tau}}{e^{-\beta z}+1} \\ &= -\frac{e^{-\epsilon\tau}}{e^{-\beta\epsilon}+1} \\ &= e^{-\epsilon\tau}(n_f - 1) \end{aligned}$$

By combining the results for $\tau > 0$ and $\tau < 0$ one obtains the expression for the non interacting Greens function:

$$G_0(\tau) = e^{-\epsilon\tau}[(n_f - 1)\theta(\tau - 0^+) + n_f\theta(-\tau + 0^+)] \tag{2.7}$$

Chapter 3

Analytic Properties of the Greens Functions

In this chapter, we will review the standard analytic properties of the thermal Greens function since these formulas will be adapted later to the Greens function defined on the finite number of Matsubara frequencies.

In Chapter 2 we discussed real and imaginary time Greens functions as separate objects. In order to treat those Greens functions as one, we extend the argument of the real time Greens function t into the complex plane. Therefore a single function with complex time argument describes the real time Greens function along the real axis and the imaginary time (thermal) Greens function along the imaginary axis. Physical observables are calculated using the real time Greens functions [1], which can be obtained by performing an analytic continuation of the imaginary time Greens function to the real time axis. The thermal Greens functions can be computed by perturbation theory. To see the analytic continuation domain we replace t with $t - i\tau$:

$$G(t - i\tau) = \theta(t)G^{>}(t - i\tau) + \theta(-t)G^{<}(t - i\tau) \tag{3.1}$$

$$G^{>}(t - i\tau) = -i\frac{1}{Z}Tr[e^{itH}e^{(\tau-\beta)H}ce^{-(\tau+it)H}c^{\dagger}] \tag{3.2}$$

$$G^{<}(t - i\tau) = i\frac{1}{Z}Tr[e^{-itH}e^{-(\tau+\beta)H}c^{\dagger}e^{(\tau+it)H}c] \tag{3.3}$$

One can conclude from the expressions of $G^{<}$ and $G^{>}$ that the exponentials in the *trace* should have negative real parts, provided that the spectrum of the Hamiltonian is positive definite, in order to converge. Hence, $G^{>}$ can be continued into the domain where $\tau-\beta < 0$ and $\tau > 0$ ($0 < \tau < \beta$). Analogously, $G^{<}$ can be continued into the domain where $\tau + \beta > 0$ and $\tau < 0$ ($-\beta < \tau < 0$).

Fig. 3.1 shows that $G^{<}(t)$ is defined on the negative part of the real time axis and analytically continued to the positive part of the imaginary time axis

[1] The real time Greens functions can be computed using Keldysh formalism.

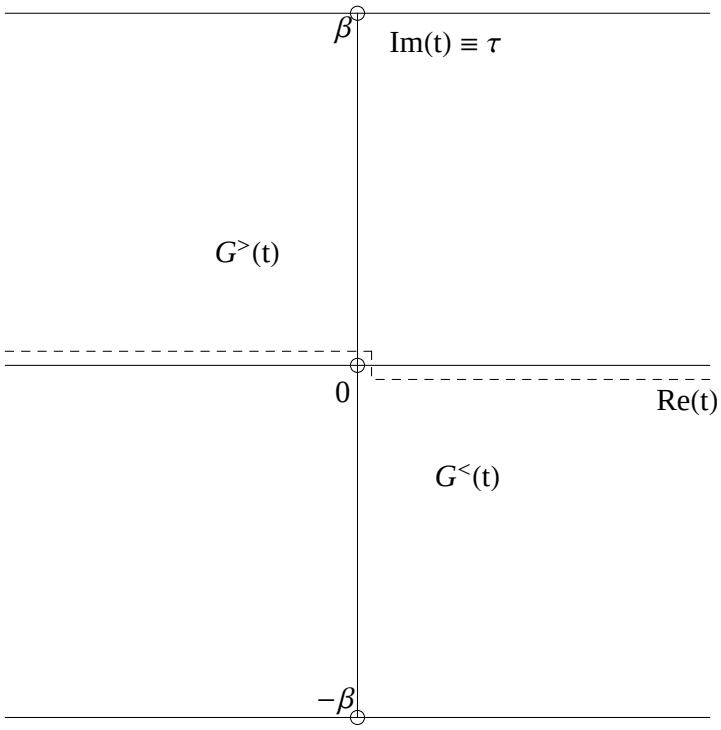

Figure 3.1: Analytic continuation domain for the real time Greens function

and $G^{>}(t)$ is defined on the positive part of the real time axis and analytically continued to the negative part of the imaginary time axis.

We have shown in Chapter 1 that the thermal Greens functions are antiperiodic with the period of β. The same holds for the complex time Greens function when its argument is shifted by $i\beta$. Using Eq. 3.3 and the cyclic property of the *trace* we find:

$$\begin{aligned} G^{<}(t+i\tau) &= \frac{i}{Z}Tr\{e^{-\beta H}c^{\dagger}e^{\tau H}(e^{itH}ce^{-itH})e^{-\tau H}\} \\ &= \frac{i}{Z}Tr\{e^{-\beta H}e^{\beta H}e^{\tau H}c(t)e^{-(\tau+\beta)H}c^{\dagger}\} \\ &= \frac{i}{Z}Tr\{e^{-\beta H}e^{(\tau+\beta)H}c(t)e^{-(\tau+\beta)H}c^{\dagger}\} \\ &= -G^{>}(t-i(\tau+\beta)) \end{aligned}$$

The complex time Greens function having the same properties as the imaginary time Greens function means that the thermal and finite temperature real time Greens function can be unified in one object.

In order to explore the analytic behaviour in frequency space we insert a complete set of eigenstates ($\{|\Psi_n\rangle\}$, $H|\Psi_n\rangle = (E_n - \mu N_n)|\Psi_n\rangle$) in the definition

of the real time Greens function to extract the time dependence explicitly and then do the Fourier transformation:

$$\begin{aligned} G(t) &= -\frac{i}{Z}[\theta(t)\sum_{m,n}\langle\Psi_m|e^{-\beta H}e^{itH}ce^{-itH}|\Psi_n\rangle\langle\Psi_n|c^\dagger|\Psi_m\rangle - \\ &\quad \theta(-t)\sum_{m,n}\langle\Psi_n|e^{-\beta H}c^\dagger|\Psi_m\rangle\langle\Psi_m|e^{itH}ce^{-itH}|\Psi_n\rangle] \\ &= -\frac{i}{Z}[\theta(t)\sum_{m,n}\langle\Psi_m|c|\Psi_n\rangle\langle\Psi_n|c^\dagger|\Psi_m\rangle e^{(-\beta+it)(E_m-\mu N_m)}e^{-it(E_n-\mu N_n)} - \\ &\quad -\theta(-t)\sum_{m,n}\langle\Psi_n|c^\dagger|\Psi_m\rangle\langle\Psi_m|c|\Psi_n\rangle e^{it(E_m-\mu N_m)}e^{(-\beta-it)(E_n-\mu N_n)}] \end{aligned}$$

Expectation value of the creation operator $\langle\Psi_n|c^\dagger|\Psi_m\rangle$ is nonzero if $N_n = N_m+1$ (N_n - number of particles in state $|\Psi_n\rangle$). So, one can see that

$$\begin{aligned} G(t) = -\frac{i}{Z}\sum_{m,n}|\langle\Psi_n|c^\dagger|\Psi_m\rangle|^2[\theta(t)e^{-\beta(E_m-\mu N_m)}e^{-it(E_n-E_m-\mu)} - \\ -\theta(-t)e^{-\beta(E_n-\mu N_n)}e^{-it(E_n-E_m-\mu)}] \end{aligned}$$

Before we carry out the Fourier transformation let us solve following integrals. An infinitesimal quantity $i\eta$ is introduced to guarantee the convergence of the integrand:

$$\begin{aligned} I_1 &= -i\int_{-\infty}^{\infty} dte^{i\omega t}\theta(t)e^{-it(E_n-E_m-\mu)} \\ &= -i\int_0^{\infty} dte^{it(\omega-(E_n-E_m-\mu))} \\ &= -i\int_0^{\infty} dte^{it(\omega-(E_n-E_m-\mu)+i\eta)} \\ &= -i\frac{-1}{i(\omega-(E_n-E_m-\mu)+i\eta)} \\ &= \frac{1}{\omega-(E_n-E_m-\mu)+i\eta} \end{aligned}$$

$$
\begin{aligned}
I_2 &= i\int_{-\infty}^{\infty} dt e^{i\omega t}\theta(-t)e^{-it(E_n-E_m-\mu)} \\
&= i\int_{-\infty}^{0} dt e^{it(\omega-(E_n-E_m-\mu))} \\
&= i\int_{-\infty}^{0} dt e^{it(\omega-(E_n-E_m-\mu)-i\eta)} \\
&= i\frac{1}{i(\omega-(E_n-E_m-\mu)-i\eta)} \\
&= \frac{1}{\omega-(E_n-E_m-\mu)-i\eta}
\end{aligned}
$$

Given I_1 and I_2 one can easily perform Fourier transformation for $G(t)$:

$$
\begin{aligned}
G(\omega) &= \frac{1}{Z}\sum_{m,n}|\langle\Psi_n|c^\dagger|\Psi_m\rangle|^2\Bigg(\frac{e^{-\beta(E_m-\mu N_m)}}{\omega-(E_n-E_m-\mu)+i\eta}+ \\
&\qquad +\frac{e^{-\beta(E_n-\mu N_n)}}{\omega-(E_n-E_m-\mu)-i\eta}\Bigg)
\end{aligned}
$$

It is useful to define, so called, *retarded* and *advanced* Greens functions in the real time space [23]:

$$G^R(t) = \theta(t)(G^>(t) - G^<(t))$$

$$G^A(t) = \theta(-t)(G^<(t) - G^>(t))$$

and correspondingly in the frequency space

$$
\begin{aligned}
G^R(\omega) = \frac{1}{Z}\sum_{m,n}|\langle\Psi_n|c^\dagger|\Psi_m\rangle|^2\Bigg(&\frac{e^{-\beta(E_m-\mu N_m)}}{\omega-(E_n-E_m-\mu)+i\eta}+ \\
&+\frac{e^{-\beta(E_n-\mu N_n)}}{\omega-(E_n-E_m-\mu)+i\eta}\Bigg)
\end{aligned}
$$

$$
\begin{aligned}
G^A(\omega) = \frac{1}{Z}\sum_{m,n}|\langle\Psi_n|c^\dagger|\Psi_m\rangle|^2\Bigg(&\frac{e^{-\beta(E_m-\mu N_m)}}{\omega-(E_n-E_m-\mu)-i\eta}+ \\
&+\frac{e^{-\beta(E_n-\mu N_n)}}{\omega-(E_n-E_m-\mu)-i\eta}\Bigg)
\end{aligned}
$$

Since the retarded Greens function includes only $\theta(t)$ and the advanced Greens function only $\theta(-t)$ their poles are in lower and upper half of the complex frequency plane, respectively. Therefore, one has to do the analytic continuation of the discrete Matsubara frequency Greens function in the upper half plane to determine the retarded Greens function and in the lower half plane to determine the advanced Greens function.

We also introduce another useful quantity: a finite temperature spectral function

$$A(\omega) = \frac{1}{Z}\sum_{m,n}|\langle\Psi_n|c^\dagger|\Psi_m\rangle|^2 e^{-\beta(E_m-\mu N_m)}(1+e^{-\beta\omega})2\pi\delta(E_n-E_m-\mu-\omega)$$

$$= \frac{1}{Z}\sum_{m,n}|\langle\Psi_n|c^\dagger|\Psi_m\rangle|^2(e^{-\beta(E_m-\mu N_m)}+ \\ + e^{-\beta(\omega+E_m-\mu N_m)})2\pi\delta(E_n-E_m-\mu-\omega) \tag{3.4}$$

Index k (quantum numbers) is suppressed in the definition of the spectral function as in the rest of the expressions. Note that due to the Dirac delta function we have: $\omega = E_n - E_m - \mu$. Thus, the spectral function can be written in the following form:

$$A(\omega) = \frac{1}{Z}\sum_{m,n}|\langle\Psi_n|c^\dagger|\Psi_m\rangle|^2(e^{-\beta(E_m-\mu N_m)}+e^{-\beta(E_n-\mu N_n)})2\pi\delta(E_n-E_m-\mu-\omega)$$

The spectral function allows us to rewrite the retarded and advanced Greens functions in a compact form:

$$G^R(\omega) = \int_{-\infty}^{\infty}\frac{d\omega'}{2\pi}\frac{A(\omega')}{\omega-\omega'+i\eta} \tag{3.5}$$

$$G^A(\omega) = \int_{-\infty}^{\infty}\frac{d\omega'}{2\pi}\frac{A(\omega')}{\omega-\omega'-i\eta} \tag{3.6}$$

Using the relation $\frac{1}{\omega\pm i\eta} = P\frac{1}{\omega} \mp i\pi\delta(\omega)$ one can identify real and imaginary parts of $G(\omega), G^R(\omega), G^A(\omega)$:

$$Re\left\{\begin{array}{c} G(\omega) \\ G^R(\omega) \\ G^A(\omega)\end{array}\right\} = P\int_{-\infty}^{\infty}\frac{d\omega'}{2\pi}\frac{A(\omega')}{\omega-\omega'} \tag{3.7}$$

$$Im\left\{\begin{array}{c} G^R(\omega) \\ G^A(\omega)\end{array}\right\} = \left\{\begin{array}{c} -\frac{1}{2}A(\omega) \\ \frac{1}{2}A(\omega)\end{array}\right\} \tag{3.8}$$

We extract the imaginary part of $G(\omega)$ in more detail:

$$
\begin{aligned}
Im[G(\omega)] &= \frac{-\pi}{Z}\sum_{m,n}\langle\Psi_n|c^\dagger|\Psi_m\rangle|^2[\delta(E_n-E_m-\mu-\omega)e^{-\beta(E_m-\mu N_m)}- \\
&\qquad -\delta(E_n-E_m-\mu-\omega)e^{-\beta(E_n-\mu N_n)}] \\
&= \frac{-\pi}{Z}\sum_{m,n}\langle\Psi_n|c^\dagger|\Psi_m\rangle|^2\delta(E_n-E_m-\mu-\omega)(e^{-\beta(E_m-\mu N_m)}- \\
&\qquad -e^{-\beta(E_n-\mu N_n)}) \\
&= \frac{-\pi}{Z}\sum_{m,n}\langle\Psi_n|c^\dagger|\Psi_m\rangle|^2\delta(E_n-E_m-\mu-\omega)(e^{-\beta(E_m-\mu N_m)}- \\
&\qquad -e^{-\beta(E_m-\mu N_m+\omega)}) \\
&= \frac{-\pi}{Z}\sum_{m,n}\langle\Psi_n|c^\dagger|\Psi_m\rangle|^2\delta(E_n-E_m-\mu-\omega)e^{-\beta(E_m-\mu N_m)}\times \\
&\qquad \times(1-e^{-\beta\omega}) \\
&= \frac{-\pi}{Z}\sum_{m,n}\langle\Psi_n|c^\dagger|\Psi_m\rangle|^2\delta(E_n-E_m-\mu-\omega)e^{-\beta(E_m-\mu N_m)}\times \\
&\qquad \times(1+e^{-\beta\omega})\frac{1-e^{-\beta\omega}}{1+e^{-\beta\omega}} \\
&= -\frac{1}{2}\tanh(\frac{\beta\omega}{2})A(\omega) \qquad (3.9)
\end{aligned}
$$

Using Eq. 3.7, 3.8, 3.9 and the identity $1/(1+e^{\beta\omega}) - 1/(1+e^{-\beta\omega}) = -\tanh(\frac{\beta\omega}{2})$ one can express $G(\omega)$ by $G^R(\omega)$ and $G^A(\omega)$ and obtain Kramers-Kronig relation:

$$G(\omega) = \frac{G^R(\omega)}{1+e^{-\beta\omega}} + \frac{G^A(\omega)}{1+e^{\beta\omega}} \qquad (3.10)$$

$$= (1-n_f)G^R(\omega) + n_f G^A(\omega) \qquad (3.11)$$

$$Re[G^R(\omega)] = -\frac{1}{\pi}P\int_{-\infty}^{\infty}\frac{d\omega'}{\omega-\omega'}Im[G^R(\omega)] \qquad (3.12)$$

Note that using Eq. 3.4 one can show the following:

$$1 = \frac{1}{Z} Tr\{e^{-\beta H}\{c, c^\dagger\}\} = \frac{1}{Z}\sum_{m,n}[\langle\Psi_m|e^{-\beta H}c|\Psi_n\rangle\langle\Psi_n|c^\dagger|\Psi_m\rangle + \\ + \langle\Psi_n|e^{-\beta H}c\dagger|\Psi_m\rangle\langle\Psi_m|c|\Psi_n\rangle]$$

$$= \frac{1}{Z}\sum_{m,n}[e^{-\beta(E_m-\mu N_m)}|\langle\Psi_n|c^\dagger|\Psi_m\rangle|^2 + \\ + e^{-\beta(E_n-\mu N_n)}|\langle\Psi_n|c^\dagger|\Psi_m\rangle|^2]$$

$$= \frac{1}{Z}\sum_{m,n}|\langle\Psi_n|c^\dagger|\Psi_m\rangle|^2[e^{-\beta(E_m-\mu N_m)} + e^{-\beta(E_n-\mu N_n)}]$$

$$= \int_{-\infty}^{\infty}\frac{d\omega}{2\pi}A(\omega)$$

The last equality represents the conservation (sum rule) of the spectral function. According to Eq. 3.4 the spectral function is positively defined quantity and therefore, can be interpreted as a probability distribution. The sum rule for the spectral function can also be obtained using $G(t = 0^-)$ and $G(t = 0^+)$:

$$G(t = 0^-) = \int\frac{d\omega}{2\pi}e^{-i\omega 0^-}\{(1 - n_f)G^R(\omega) + n_f G^A(\omega)\}$$

$$= \oint\frac{dz}{2\pi}e^{-iz0^-}(1 - n_f)G^R(z) + \int\frac{d\omega}{2\pi}e^{-i\omega 0^-}n_f G^A(\omega)$$

$$= \int\frac{d\omega}{2\pi}n_f(G^A(\omega) - G^R(\omega))$$

$$= \int\frac{d\omega}{2\pi}i\ n_f A(\omega) \tag{3.13}$$

were the integration curve is a semi-circle extended to $+\infty$ and we used Eq. 3.10, 3.8 and the following equality:

$$\oint\frac{dz}{2\pi}(1 - n_f)G^R(z) = -\oint\frac{dz}{2\pi}n_f G^R(z) \tag{3.14}$$

The latter is true because $1 - n_f$ and n_f have exactly same poles with opposite-sign residues. Analogously, for $G(t = 0^+)$:

$$
\begin{aligned}
G(t=0^+) &= \int \frac{d\omega}{2\pi} e^{-i\omega 0^+} \{(1-n_f)G^R(\omega) + n_f G^A(\omega)\} \\
&= \oint \frac{dz}{2\pi} e^{-iz0^+} n_f G^A(z) + \int \frac{d\omega}{2\pi} e^{-i\omega 0^+} (1-n_f) G^R(\omega) \\
&= \int \frac{d\omega}{2\pi} (1-n_f)(G^R(\omega) - G^A(\omega)) \\
&= \int \frac{d\omega}{2\pi} i\ (n_f - 1) A(\omega) \qquad (3.15)
\end{aligned}
$$

On the other hand, according to the definition of $G(t)$ we have:

$$G(t=0^-) = -i\langle T c(0^-) c^\dagger(0)\rangle = i\langle c^\dagger(0) c(0^-)\rangle = i\ n \qquad (3.16)$$

$$G(t=0^+) = -i\langle T c(0^+) c^\dagger(0)\rangle = -i\langle c(0^+) c^\dagger(0)\rangle = i\ (n-1) \qquad (3.17)$$

where n is the particle number. By combining Eq. 3.15, 3.13, 3.16 , 3.17 one can show that:

$$i = G(t=0^-) - G(t=0^+) = \int \frac{d\omega}{2\pi} i A(\omega)(n_f - n_f + 1) = \int \frac{d\omega}{2\pi} i A(\omega)$$

Thus, the Greens function discontinuity provides the sum rule for the spectral function:

$$\int \frac{d\omega}{2\pi} A(\omega) = 1$$

The sum rule tells us that for large frequencies we have

$$\lim_{\omega\to\infty} \left\{ \begin{array}{c} G(\omega) \\ G^R(\omega) \\ G^A(\omega) \end{array} \right\} = \int_{-\infty}^{\infty} \frac{d\omega'}{2\pi} \frac{A(\omega')}{\omega} = \frac{1}{\omega}$$

Now, let us relate the thermal Greens function to the real time Greens function. We start with extracting the time dependent part from the thermal Greens function to perform the Fourier transformation to the Matsubara frequency space:

$$
\begin{aligned}
G(\tau > 0) &= -\langle c(\tau)\ c^\dagger\rangle \\
&= -\frac{1}{Z} \sum_{m,n} \langle \Psi_m | e^{-\beta H} e^{\tau H} c e^{-\tau H} | \Psi_n\rangle \langle \Psi_n | c^\dagger | \Psi_m\rangle \\
&= -\frac{1}{Z} \sum_{m,n} |\langle \Psi_n | c^\dagger | \Psi_m\rangle|^2 e^{-\beta(E_m - \mu N_m)} e^{-\tau(E_n - E_m - \mu)} \qquad (3.18)
\end{aligned}
$$

$$G(i\omega_n) = \int_0^\beta d\tau e^{i\omega_n \tau} G(\tau) =$$

$$= -\frac{1}{Z}\sum_{m,n} |\langle \Psi_n | c^\dagger | \Psi_m \rangle|^2 e^{-\beta(E_m - \mu N_m)} \int_0^\beta d\tau e^{i\omega_n \tau} e^{-\tau(E_n - E_m - \mu)}$$

$$= -\frac{1}{Z}\sum_{m,n} |\langle \Psi_n | c^\dagger | \Psi_m \rangle|^2 e^{-\beta(E_m - \mu N_m)} \frac{e^{i\beta\omega_n} e^{-\beta(E_n - E_m - \mu)} - 1}{i\omega_n - (E_n - E_m - \mu)}$$

$$= \frac{1}{Z}\sum_{m,n} |\langle \Psi_n | c^\dagger | \Psi_m \rangle|^2 \frac{e^{-\beta(E_n - \mu N_n)} + e^{-\beta(E_m - \mu N_m)}}{i\omega_n - (E_n - E_m - \mu)}$$

$$= \int \frac{d\omega'}{2\pi} \frac{A(\omega')}{i\omega_n - \omega'} \tag{3.19}$$

During the derivation we used the identity: $e^{i\beta\omega_n} = e^{i\pi(2n+1)} = -1$.

Taking into account the domains of the analyticity for $G^R(\omega)$ (analytic in the upper half plane) and $G^A(\omega)$ (analytic in the lower half plane), we see that, $G(i\omega_n)$ should be continued in the upper half plane to determine retarded Greens function and in the lower half plane to determine advanced Greens function. After determining $G^R(\omega)$ and $G^A(\omega)$ one can calculate $G(\omega)$ using Eq. 3.10 .

$G(i\omega_n)$ (Eq. 3.19) is analogous to the retarded (advanced) Greens function, but it has $i\omega_n$ in the denominator instead of $\omega + i\eta$ ($\omega - i\eta$). So, If the analytic form of the thermal Greens function is given then the procedure of the analytic continuation is equivalent to the replacing of $i\omega_n$ by $\omega \pm i0^+$.

The analytic properties of the standard thermal Greens functions described in this chapter will be adapted to the Greens function defined on the finite number of Matsubara frequencies as shown in the following chapters.

Although the thermal Greens function is defined on the discrete set of points the analytic continuation is unique, because it has the following behaviour at infinity: $G(z) \sim 1/z$. One can prove the latter statement using Carlson's theorem [23]: if a function $\phi(z)$ is regular and zero on a discrete set of points and at the accumulation point of that set then $\phi(z)$ is identically zero. For example, a function $f(z) = 1/(z-(\epsilon-\mu))$ coincides with the non interacting thermal Greens function $G_0(i\omega_n)$ at Matsubara frequencies $z = i\omega_n$, where $\omega_n = (2n+1)\pi/\beta$ and n is an integer. Now, assume that $\phi(z)$ vanishes at the Matsubara frequencies and consider $f(z) = 1/(z - (\epsilon - \mu)) + \phi(z)$, which also coincides with $G_0(i\omega_n)$ at $z = i\omega_n$. Since $G_0(i\omega_n)$ vanishes at infinitely large $i\omega_n$ the function $\phi(i\omega_n)$ should also do so in the same limit in order $f(i\omega_n)$ to be equal to $G_0(i\omega_n)$. According to the Carlson's theorem $\phi(z)$ is identically zero, because it is zero at the discrete set of points and infinity, which is the accumulation point of the set of the Matsubara frequencies. To conclude, there is no way to modify the analytically continued Greens function and recover the original thermal Greens function values by evaluating it at the Matsubara frequencies without destroying the Greens function behaviour at infinity. The same was proved By G. Baym and N. D. Mermin [24] but in a different way.

3.1 Calculation of the Spectral Weight Function

To compute the spectral weight function using 3.4 one has to know a complete set of states for a given system which, in most cases, is impossible. Common way of obtaining the spectral function is through the real frequency Greens function. Obviously, computation of the real frequency Greens function requires an analytic continuation of the thermal Greens function commonly achieved by introducing an ansatz for the spectral function which depends on a set of unknown parameters. These parameters are determined by putting demands on the ansatz which has to be fulfilled by the physical spectral weight function.

Let us model the spectral weight function by a Lorentzian

$$A(\omega) = \frac{2\gamma}{(\omega - \epsilon_0)^2 + \gamma^2} \tag{3.20}$$

ϵ_0 is the location and γ - the width of the Lorentzian. By using the Lorentzian in Eq. 3.19 one gets

$$\begin{aligned} G(i\omega_n) &= \int \frac{d\omega'}{2\pi} \frac{2\gamma}{(\omega' - \epsilon_0)^2 + \gamma^2} \frac{1}{i\omega_n - \omega'} \\ &= \int \frac{d\omega'}{2\pi i} \left(\frac{1}{\omega' - \epsilon_0 - i\gamma} - \frac{1}{\omega' - \epsilon_0 + i\gamma} \right) \frac{1}{i\omega_n - \omega'} \end{aligned}$$

Since the integrand decays as $1/z^2$ it can be continued to the entire complex plane and the integration can be performed along the semicircle with an infinite radius. It is clear that the integrand has three poles. Depending on the sign of ω_n two poles are in the upper half plane and one is in the lower half plane or vice versa. If ω_n is positive than it is convenient to do integration along C_2 curve, because it encircles only one pole (see Fig. 3.2):

$$\begin{aligned} G(i\omega_n) &= \oint_{C_2} \frac{dz}{2\pi i} \left(\frac{1}{z - \epsilon_0 - i\gamma} - \frac{1}{z - \epsilon_0 + i\gamma} \right) \frac{1}{i\omega_n - z} \\ &= -2\pi i \, \frac{1}{2\pi i} \lim_{z \to \epsilon_0 - i\gamma} \frac{z - (\epsilon_0 - i\gamma)}{i\omega_n - z} \left(\frac{1}{z - \epsilon_0 - i\gamma} - \frac{1}{z - \epsilon_0 + i\gamma} \right) \\ &= \frac{1}{i\omega_n - (\epsilon_0 - i\gamma)} \end{aligned} \tag{3.21}$$

It is obvious that when ω_n is negative it is more convenient to do integration along C_1:

$$G(i\omega_n) = \oint_{C_1} \frac{dz}{2\pi i} \left(\frac{1}{z - \epsilon_0 - i\gamma} - \frac{1}{z - \epsilon_0 + i\gamma} \right) \frac{1}{i\omega_n - z}$$

$$= 2\pi i \, \frac{1}{2\pi i} \lim_{z \to \epsilon_0 + i\gamma} \frac{z - (\epsilon_0 + i\gamma)}{i\omega_n - z} \left(\frac{1}{z - \epsilon_0 - i\gamma} - \frac{1}{z - \epsilon_0 + i\gamma} \right)$$

$$= \frac{1}{i\omega_n - (\epsilon_0 + i\gamma)} \tag{3.22}$$

One can generalize Eq. 3.20 and assume that the spectral weight function is a sum of the Lorentzian resonances

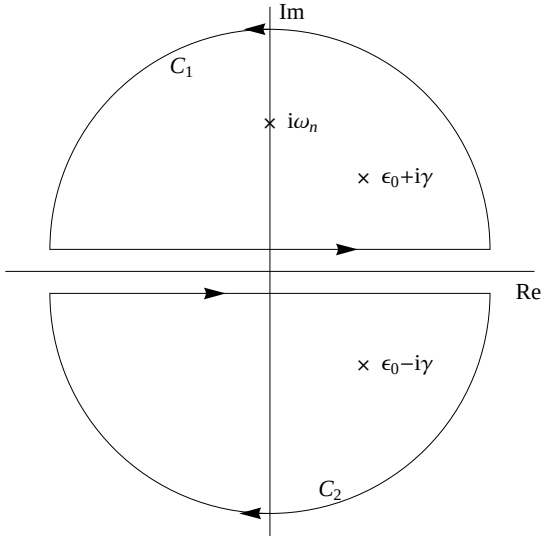

Figure 3.2: C_1 and C_2 are the integration contours for $G(i\omega_n)$. Crosses are the poles of the integrand when $\omega_n > 0$

$$A(\omega) = 2 \sum_\nu \frac{\gamma_\nu \alpha_\nu + \beta_\nu(\omega - \epsilon_\nu)}{(\omega - \epsilon_\nu)^2 + \gamma_\nu^2} = \frac{1}{i} \sum_\nu \left(\frac{a_\nu}{\omega - b_\nu} - \frac{a_\nu^*}{\omega - b_\nu^*} \right) \tag{3.23}$$

where $\alpha_\nu, \beta_\nu, \epsilon_\nu, \gamma_\nu$ are real parameters, $a_\nu = \alpha_\nu + i\beta_\nu$ and $b_\nu = \epsilon_\nu + i\gamma_\nu$. The parameter ϵ_ν characterizes the location of the resonance and γ_ν - the width. After inserting Eq 3.23 in Eq. 3.19 and performing contour integrals separately for each term of the sum (Eq. 3.23) in the same manner as we did in Eq. 3.21 and 3.22 (in this case poles $\epsilon_0 + i\gamma$ and $\epsilon_0 - i\gamma$ are replaced by b_ν and b_ν^*), one obtains:

$$G(i\omega_n) = \begin{cases} \sum_\nu \frac{a_\nu^*}{i\omega_n - b_\nu^*} & \omega_n > 0 \\ \sum_\nu \frac{a_\nu}{i\omega_n - b_\nu} & \omega_n < 0 \end{cases}$$

The sum rule for the spectral weight function puts constraints on the parameters a_ν. Namely, they obey the following relation: $\sum_\nu a_\nu = \sum_\nu a_\nu^* = 1$. This can be shown by evaluating the contour integral along the curves C_1 and C_2 over the spectral weight function:

$$\begin{aligned}
1 &= \sum_\nu \int \frac{d\omega}{2\pi i} \left(\frac{a_\nu}{\omega - b_\nu} - \frac{a_\nu^*}{\omega - b_\nu^*} \right) \\
&= \sum_\nu \oint_{C_1} \frac{dz}{2\pi i} \left(\frac{a_\nu}{z - b_\nu} - \frac{a_\nu^*}{z - b_\nu^*} \right) \\
&= \sum_\nu \lim_{z \to b_\nu} (z - b_\nu) \left(\frac{a_\nu}{z - b_\nu} - \frac{a_\nu^*}{z - b_\nu^*} \right) \\
&= \sum_\nu a_\nu
\end{aligned}$$

Analogously, performing integration along C_2 yields: $\sum_\nu a_\nu^* = 1$.

Chapter 4

Discretized Thermal Greens Functions

In this chapter I present a new numerical method for the Fermionic thermal Greens functions. The formalism describes how periodized Greens functions should be treated appropriately and the procedure of analytic continuation which gives the discontinuity of the Greens function. As we will see below the discontinuity is related to the conservation of the spectral function.

We start with discretizing the argument of the imaginary time Greens functions. As we see, the thermal Greens function $G(\tau)$ is well behaved apart form a discontinuous boundary. So we discretize imaginary time $i\tau$ into N evenly spaced points on the interval $[0, i\beta]$. Recalling, that the imaginary time Greens function domain is $\tau \in [-\beta, \beta]$ we see it must remain antiperiodic on this domain with a period of β.

The discrete Fourier transformation can be applied to the imaginary time Greens function data points. The Fourier transform of a discrete periodic function is itself periodic and thus yields a periodic, discrete set of the Greens function values in the frequency space. However, if we look at the simplest, noninteracting Greens function $G(i\omega_n) = 1/(i\omega_n - \epsilon)$ it is clear that it is not periodic and in addition has a long frequency tail, necessary to obtain the discontinuous boundary in τ-space. This means that the periodization in the frequency space causes problems with the discontinuity in the imaginary time space.

In this chapter we will show how to periodize the noninteracting Greens function when the argument of the imaginary time Greens function is discretized into N evenly spaced points and preserve the discontinuity in τ-space.

We discretize the interval $\tau \in [0, \beta]$ in the obvious way: $\tau_j = \beta j/N, \quad 0 < j < N-1$, which represents set of N evenly spaced points on the imaginary time axis. We note that $\tau = \beta$ doesn't belong to this set. The discrete imaginary time Greens function is antiperiodic in the same way as its continuous version,

which means that it is representable as a discrete Fourier transformation:

$$G(\tau_j) = \frac{1}{\beta}\sum_{n=0}^{N-1} e^{-i\omega_n\tau_j} G(i\omega_n) \tag{4.1}$$

$$G(i\omega_n) = \frac{\beta}{N}\sum_{j=0}^{N-1} e^{i\omega_n\tau_j} G(\tau_j) \tag{4.2}$$

where $\omega_n = (2n+1)\pi/\beta$ are Matsubara frequencies and the pre-factor β/N in Eq. 4.2 is due to the discretization of the integral in Eq. 2.3.

Since the imaginary time Greens function has the discontinuity at $\tau = 0$ (limits $\tau \to 0^-$ and $\tau \to 0^+$ differ from each other) we must uniquely assign the value to $G(\tau_j = 0)$. We define $G(\tau_j = 0)$ by the average of the two limits:

$$G(\tau_j = 0) = (G(\tau_j = 0^-) + G(\tau_j = 0^+))/2 = (n + n - 1)/2 = n - 1/2 \tag{4.3}$$

where n is an occupation number.

Let us calculate explicitly the discrete Fourier transform of the discretized, noninteracting imaginary time Greens function $G_0(\tau_j > 0) = e^{-\tau_j\epsilon}(n_f - 1)$ taking into account our definition of $G(\tau_j = 0)$:

$$\begin{aligned}
G_0(i\omega_n) &= \frac{\beta}{N}\sum_{j=0}^{N-1} e^{i\tau_j\omega_n} G_0(\tau_j) \\
&= \frac{\beta}{N}[G_0(0) + \sum_{j=1}^{N-1} e^{i\tau_j\omega_n} G_0(\tau_j)] \\
&= \frac{\beta}{N}[n_f - \frac{1}{2} + \sum_{j=1}^{N-1} e^{\tau_j(i\omega_n-\epsilon)}(n_f - 1)] \\
&= \frac{\beta}{N}[n_f - \frac{1}{2} + \sum_{j=1}^{N-1} e^{\frac{\beta}{N}(i\omega_n-\epsilon)j}(n_f - 1)]
\end{aligned}$$

Now we use the formula for the sum of the geometric progression: $\sum_{n=0}^{N} ar^n = a(1 - r^{N+1})/(1 - r)$:

$$\begin{aligned}
G_0(i\omega_n) &= \frac{\beta}{N}\left(n_f - \frac{1}{2} + (n_f - 1)\frac{e^{\frac{\beta}{N}(i\omega_n-\epsilon)} - e^{\beta(i\omega_n-\epsilon)}}{1 - e^{\frac{\beta}{N}(i\omega_n-\epsilon)}}\right) \\
&= \frac{\beta}{N}\left(n_f - \frac{1}{2} + (n_f - 1)\frac{e^{\frac{\beta}{N}(i\omega_n-\epsilon)} + e^{-\beta\epsilon}}{1 - e^{\frac{\beta}{N}(i\omega_n-\epsilon)}}\right)
\end{aligned} \tag{4.4}$$

$$= \frac{\beta}{N} \frac{(n_f - 1/2)(1 - e^{\frac{\beta}{N}(i\omega_n - \epsilon)}) + (n_f - 1)(e^{\frac{\beta}{N}(i\omega_n - \epsilon)} + e^{-\beta\epsilon})}{1 - e^{\frac{\beta}{N}(i\omega_n - \epsilon)}}$$

$$= \frac{\beta}{N} \frac{-\frac{1}{2}e^{\frac{\beta}{N}(i\omega_n - \epsilon)} + n_f - \frac{1}{2} + (n_f - 1)e^{-\beta\epsilon}}{1 - e^{\frac{\beta}{N}(i\omega_n - \epsilon)}}$$

$$= \frac{\beta}{N} \frac{-\frac{1}{2}(e^{\frac{\beta}{N}(i\omega_n - \epsilon)} + 1) + \frac{1}{e^{\beta\epsilon}+1} - \frac{e^{-\beta\epsilon}}{1+e^{-\beta\epsilon}}}{1 - e^{\frac{\beta}{N}(i\omega_n - \epsilon)}}$$

$$= \frac{\beta}{2N} \frac{e^{\frac{\beta}{N}(i\omega_n - \epsilon)} + 1}{e^{\frac{\beta}{N}(i\omega_n - \epsilon)} - 1}$$

$$= \frac{\beta}{2N} \coth \frac{\beta}{2N}(i\omega_n - \epsilon)$$

$$= \eta \coth \eta(i\omega_n - \epsilon) \tag{4.5}$$

where $\eta \equiv \frac{\beta}{2N}$. It is obvious that Eq. 4.4 is periodic under $i\omega_n \to i\omega_n + i\Omega_N$, $\Omega_N \equiv \frac{\pi}{\eta}$. In the limit $N \to \infty$ ($\eta \to 0$) we recover the continuum expression for the noninteracting Greens function:

$$\lim_{\eta \to 0} \eta \coth \eta(i\omega_n - \epsilon) = \frac{1}{i\omega_n - \epsilon}$$

The next step would be to carry out the analogous periodization procedure for the interacting thermal Greens functions. It is well known that the full Greens function can be written in terms of the self-energy and noninteracting Greens function, which is called Dyson equation [23]:

$$G(i\omega_n) = G_0 + G_0 \Sigma G = G_0 + G_0 \Sigma G_0 + G_0 \Sigma G_0 \Sigma G_0 + ... \tag{4.6}$$

The Dyson equation is usually obtained from the definition of the self-energy, $\Sigma = G_0^{-1}(i\omega_n) - G^{-1}(i\omega_n)$, by multiplying it with $G_0(i\omega_n)$ and $G(i\omega_n)$. But there is an alternative way to derive Eq. 4.6. Let us define $g(x) = 1/x$. A Taylor expansion of $G(i\omega_n)$

$$G(i\omega_n) = \frac{1}{G_0^{-1}(i\omega_n) - \Sigma(i\omega_n)} = \frac{1}{g^{-1}(i\omega_n - \epsilon) - \Sigma(i\omega_n)} = \frac{1}{i\omega_n - \epsilon - \Sigma(i\omega_n)}$$

$$\equiv g(i\omega_n - \epsilon - \Sigma) \tag{4.7}$$

around $G_0(i\omega_n)$ in the self-energy $\Sigma(i\omega_n)$ yields the Dyson equation:

$$G = \sum_{n=0}^{\infty} \frac{\Sigma^n}{n!} \left. \frac{d^n g}{d\Sigma^n} \right|_{\Sigma=0} = G_0 + G_0 \Sigma G_0 + G_0 \Sigma G_0 \Sigma G_0 + ...$$

$G_0(i\omega_n)$ and $\Sigma(i\omega_n)$ are placed in such order (as shown in the latter expression) to identify the series with the diagrammatic expansion. By analogy, we can derive the "Dyson equation" for the periodized Greens functions. In this case $g(x)$ would be $g(x) = \eta \coth(\eta x)$ and for the full Greens function we get:

$$G(i\omega_n) \equiv g(i\omega_n - \epsilon - \Sigma) = \eta \coth \eta(i\omega_n - \epsilon - \Sigma) \tag{4.8}$$

Due to the nontrivial hyperbolic function in Eq. 4.8 one can not define the self-energy using simply G_0^{-1} and G^{-1} as before. In this case the self-energy is defined by the amputated skeleton diagrams ([23], see Sec. 5.1) and through Eq. 4.8. It is clear that Eq. 4.8 is more general and reduces to Eq. 4.7 in the limit $\eta \to 0$.

After Taylor expanding Eq. 4.8 in Σ around the free Greens function we find a series that plays the same role the ordinary Dyson series:

$$\begin{aligned} G(i\omega_n) = G_0(i\omega_n) &+ G_0^+(i\omega_n)\Sigma(i\omega_n)G_0^-(i\omega_n) + \\ &+ G_0^+(i\omega_n)\Sigma(i\omega_n)G_0\Sigma(i\omega_n)G_0^-(i\omega_n) + \\ &+ G_0^+(i\omega_n)\Sigma(i\omega_n)\left[G_0(i\omega_n) + \frac{\beta}{2N\sqrt{3}}\right]\Sigma(i\omega_n)\left[G_0(i\omega_n) - \right. \\ &\left. - \frac{\beta}{2N\sqrt{3}}\right]\Sigma(i\omega_n)G_0^-(i\omega_n) + ... \end{aligned}$$

where $G_0^{\pm}$ is $G_0 \pm \eta$. As one can see the third and higher order terms involve legs $G_0(i\omega_n) + a\frac{\beta}{2N}$, with $-1 \leq a \leq 1$. The latter expression is consistent with the ordinary Dyson equation and with the self-energy being the one particle irreducible amputated diagrams but with specific choice of the free Greens functions. This definition of the self-energy is different from the standard definition in terms of the inverse Greens functions but is analogous to the alternative definition in terms of a Taylor series. In continuum case these two definitions are equivalent but in the discretized case they are not.

Performing the Fourier transformation on $G_0^{\pm}(i\omega_n)$ yields:

$$\frac{1}{\beta}\sum_{n=0}^{N-1} G_0^+(i\omega_n) = \frac{1}{\beta}\sum_{n=0}^{N-1}(G_0(i\omega_n) + \eta) = n_f - \frac{1}{2} + \frac{1}{2} = n_f = G_0(\tau = 0^-)$$

$$\frac{1}{\beta}\sum_{n=0}^{N-1} G_0^-(i\omega_n) = \frac{1}{\beta}\sum_{n=0}^{N-1}(G_0(i\omega_n) - \eta) = n_f - \frac{1}{2} - \frac{1}{2} = n_f - 1 = G_0(\tau = 0^+)$$

which shows the correspondence between $G^{\pm}(i\omega_n)$ and $G(\tau = 0^{\mp})$.

The next chapter shows how to consistently replace the Dyson series through the Luttinger-Ward functional theorem rather through a direct sum of an infinite number of diagrams.

Chapter 5

Luttinger-Ward Functional Theory

5.1 Standard Luttinger-Ward Functional Theory

We start by reviewing ordinary Luttinger-Ward functional theory and adapt it in the next section to the periodized Greens functions.

It is known from the linked cluster theorem that the free energy can be written as a sum of all connected (linked) diagrams [23]:

$$\Omega - \Omega_0 = -\frac{1}{\beta} \sum \textit{all connected diagrams} =$$

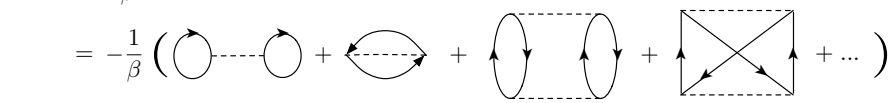

The solid lines in the diagrams represent bare (non interacting) Greens functions, G_0. In order to rewrite the free energy in terms of the interacting Greens functions it is convenient to introduce the definition for the self-energy in terms of diagrams: the self-energy is the sum of all amputated one-particle irreducible diagrams [23]:

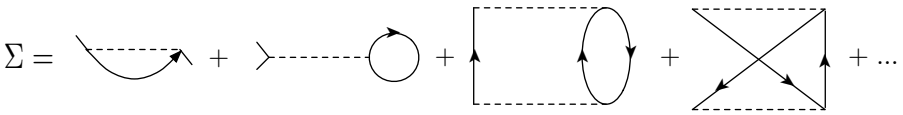

We introduce another class of the diagrams which is called skeleton diagrams which does not have any self-energy insertions, that is there is no part in the diagram which can be absorbed by the legs (Greens function lines) of the diagram. Self-energy can therefore be obtained by drawing all skeleton diagrams

and replacing the free Greens functions with the interacting ones [25]:

$$\Sigma = \sum \textit{all possible amputated skeleton diagrams with } G_0 \textit{ replaced by } G \tag{5.1}$$

For example, the diagram (a) on Fig. 5.1 is one-particle irreducible amputated, but not skeleton diagram because it has the self-energy insertion. The diagram (b) is a skeleton diagram, it doesn't have a self-energy insertion like diagram (a), written in terms of the interacting Greens functions (double lines), which, after expanding G using the Dyson series, reproduces infinite series of the one-particle irreducible amputated diagrams and one of them is diagram (a).

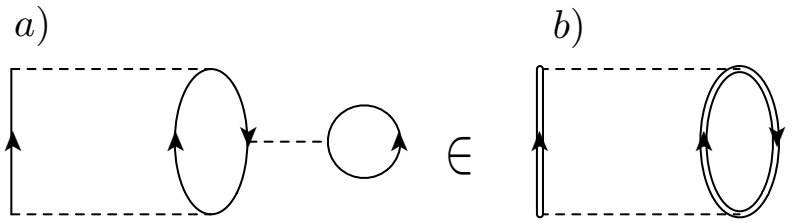

Figure 5.1: a) One-particle irreducible amputated (non skeleton) diagram contributing to the self-energy. b) A skeleton diagram

One might think that the linked cluster theorem is equivalent to writing the free energy as the sum of all closed linked skeleton diagrams and replace G_0 by G. This is not true, because after expanding interacting Greens function G the same diagram appear several times, whereas according to the linked cluster theorem each closed linked diagram must appear once in the sum. For instance, the diagram (a) on Fig. 5.2 is closed linked skeleton diagram, which reproduces the diagram (b) multiple times.

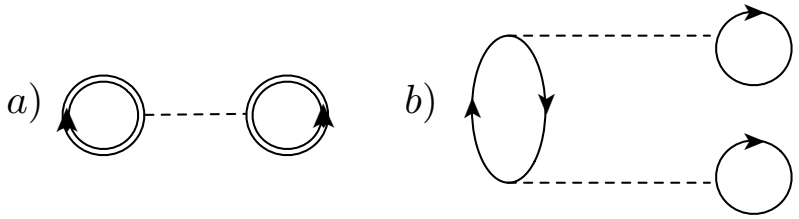

Figure 5.2: a) First order closed linked skeleton diagram with full Greens function G. b) Second order closed linked diagram contributing to the free energy Ω.

To write the free energy in terms of the interacting Greens function and self-energy Luttinger and Ward introduce the "total self-energy" $\Sigma'(i\omega_n)$ [25], sum of all amputated one-particle irreducible and reducible diagrams:

$$\begin{aligned}\Sigma'(i\omega_n) &= \Sigma(i\omega_n) + \Sigma(i\omega_n)G_0(i\omega_n)\Sigma(i\omega_n)+ \\ &+ \Sigma(i\omega_n)G_0(i\omega_n)\Sigma(i\omega_n)G_0(i\omega_n)\Sigma(i\omega_n) + ... \\ &= G_0^{-1}(i\omega_n)\Sigma(i\omega_n)G(i\omega_n)\end{aligned}$$

and then they write the mth order free energy in the following form

$$\Omega_m = \frac{1}{2m}\frac{1}{\beta} Tr\ G_0(i\omega_n)\Sigma'_m(i\omega_n) \tag{5.2}$$

where Tr is the sum over all quantum numbers and Matsubara frequencies (remember that each Greens function and self-energy has k index which is not written out explicitly). If we close all mth order diagrams of Σ' the same closed linked diagram will be generated 2m times. For example, four second order diagrams, namely, the diagram (a) with the same diagram where the direction of the straight line is flipped and the diagram (b) with the one where the lower loop is disconnected gives the diagram (c) four times (see Fig. 5.3). The prefactor $1/2m$ in Eq. 5.2 ensures that we do not over-count the diagrams. It is not straightforward to understand why one should use Σ' and not Σ itself in Eq. 5.2. To make it clear look at the Fig. 5.3: the diagram (a) is the one-particle reducible diagram which is involved in Σ', but not in the proper self-energy. After multiplying by the free Greens function G_0 we get the diagram (c) which contributes to the free energy according to the linked cluster theorem.

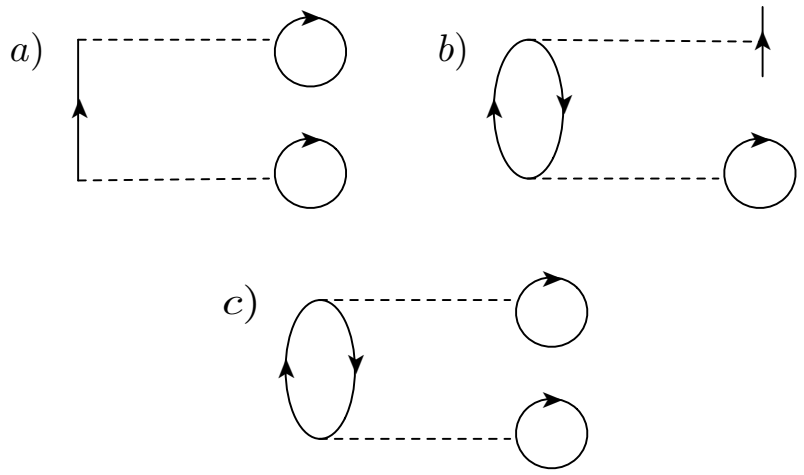

Figure 5.3: a) Second order reducible diagram contributing to Σ' not Σ. b) Second order irreducible diagram contributing to Σ. c) Second order closed linked diagram contributing to the free energy Ω.

Eq. 5.2 leads us to the following expression for the free energy:

$$\Omega = \sum_m \Omega_m = \frac{1}{\beta}\sum_m \frac{1}{2m} Tr\ G_0(i\omega_n)\Sigma'_m(i\omega_n) \tag{5.3}$$

The presence of the pre-factor $1/2m$ makes it difficult to perform the summation over m. To avoid the summation one can do the following: let us say λ is the strength of the interaction, then it is clear that Σ'_m is proportional to λ^m and $\lambda\frac{d\Sigma'}{d\lambda} = m\Sigma'$. Now take the derivative of the free energy with respect of λ:

$$\begin{aligned}\lambda\frac{d\Omega}{d\lambda} &= \frac{1}{2\beta}Tr\ G_0(i\omega_n)\Sigma'(i\omega_n) = \frac{1}{2\beta}Tr\ G_0(i\omega_n)G_0^{-1}(i\omega_n)\Sigma(i\omega_n)G(i\omega_n) \\ &= \frac{1}{2\beta}Tr\ \Sigma(i\omega_n)G(i\omega_n) \end{aligned} \tag{5.4}$$

According to Luttinger and Ward, we define the following functional [25]

$$\Gamma = \Phi[G] + Tr\ e^{i\omega_n 0^+}[-\Sigma(i\omega_n)G(i\omega_n) + \log(-G(i\omega_n)/\beta)] \tag{5.5}$$

The functional $\Phi[G]$ is sum of all closed linked skeleton diagrams with G_0 replaced by G.

Let us take the derivative of Γ with respect to the self-energy $\Sigma(i\omega_n)$:

$$\begin{aligned}\frac{\partial\Gamma}{\partial\Sigma(i\omega_n)} &= \frac{\partial\Phi}{\partial\Sigma(i\omega_n)} - G(i\omega_n) - \Sigma(i\omega_n)\frac{\partial G(i\omega_n)}{\partial\Sigma(i\omega_n)} + \frac{1}{G(i\omega_n)}\frac{\partial G(i\omega_n)}{\partial\Sigma(i\omega_n)} \\ &= \frac{\partial\Phi}{\partial\Sigma(i\omega_n)} - \Sigma(i\omega_n)G^2(i\omega_n) \end{aligned} \tag{5.6}$$

Here we used the following relation: $\partial G(i\omega_n)/\partial\Sigma(i\omega_n) = G^2(i\omega_n)$. In analogy with Eq. 5.2 one can write down the similar expression for the functional $\Phi[G]$

$$\Phi[G] = \sum_{m,n}\frac{1}{2m}Tr\ G(i\omega_n)\Sigma''_m(i\omega_n) \tag{5.7}$$

where $\Sigma''_m(i\omega_n)$ is the mth order contribution to the self-energy according to Eq. 5.1 where the order is given by the order of the skeleton diagram (not counting the vertices in the full Greens function). Taking the derivative of Eq. 5.7 with respect to $\Sigma(i\omega_n)$ and $G(i\omega_n)$ yields:

$$\begin{aligned}\frac{\partial\Phi}{\partial G(i\omega_n)} &= \sum_m\frac{1}{2m}\left[\Sigma''_m(i\omega_n) + \sum_l G(i\omega_l)\frac{\partial\Sigma''_m(i\omega_l)}{\partial G(i\omega_n)}\right] \\ &= \sum_m\frac{1}{2m}\left[\Sigma''_m(i\omega_n) + (2m-1)\Sigma''_m(i\omega_n)\right] = \Sigma(i\omega_n) \end{aligned} \tag{5.8}$$

$$\frac{\partial\Phi}{\partial\Sigma(i\omega_n)} = \frac{\partial\Phi}{\partial G(i\omega_n)}\frac{\partial G(i\omega_n)}{\partial\Sigma(i\omega_n)} = G^2(i\omega_n)\Sigma(i\omega_n) \tag{5.9}$$

After inserting $\partial\Phi/\partial\Sigma(i\omega_n)$ back into Eq. 5.6 we find that if the self-energy in Γ obeys the Dyson equation it is the stationary point for the Γ functional:

$$\frac{\partial\Gamma}{\partial\Sigma(i\omega_n)} = 0. \tag{5.10}$$

One can also say that the stationarity condition for Γ gives Eq. 5.1, which means that we have a variational principle for computing the self-energy.

Now let us take the derivative of Γ with respect to λ (interaction strength), taking into account Eq. 5.10, 5.7 , $\Sigma''_m(i\omega_n) \propto \lambda^m$ and the fact that only $\Phi[G]$ has explicit λ-dependence:

$$\lambda \frac{d}{d\lambda}\Gamma(\Sigma(\lambda), \Phi(\Sigma(\lambda), \lambda)) = \lambda \left(\frac{\partial \Gamma}{\partial \Sigma}\frac{d\Sigma}{d\lambda} + \frac{\partial \Gamma}{\partial \lambda} \right) = \lambda \frac{\partial \Phi}{\partial \lambda} = \frac{1}{2} Tr\ G(i\omega_n)\Sigma(i\omega_n) \tag{5.11}$$

It is clear from the Eq. 5.4 and 5.11 that

$$\lambda \frac{d(\beta\Omega)}{d\lambda} = \lambda \frac{d\Gamma}{d\lambda} \tag{5.12}$$

Since the last expression is a differential equation the functional Γ is equal to $\beta\Omega$ if Γ is equal to Ω_0 in the non interacting limit:

$$\begin{aligned}
\Gamma(\lambda = 0) &= Tr\ [e^{i\omega_n 0^+} \log(-G_0(i\omega_n)/\beta)] \\
&= Tr\ [e^{i\omega_n 0^+} \log(-G_0(i\omega_n))] - \log(\beta) Tr\ e^{i\omega_n 0^+} \\
&= -Tr\ [e^{i\omega_n 0^+} \log(\epsilon_k - i\omega_n)] \\
&= -\frac{\beta}{2\pi i} \sum_k \oint_C dz\ e^{z0^+} \frac{\log(\epsilon_k - z)}{e^{\beta z} + 1} \\
&= -\frac{\beta}{2\pi i} \sum_k \frac{1}{\beta} \oint_{C'} dz\ e^{z0^+} \frac{\log(1 + e^{-\beta z})}{z - \epsilon_k} \\
&= -\sum_k lim_{z \to \epsilon_k} (z - \epsilon_k) \frac{\log(1 + e^{-\beta z})}{z - \epsilon_k} \\
&= -\sum_k \log(1 + e^{-\beta \epsilon_k}) \\
&= \beta\Omega_0
\end{aligned}$$

Here we used the same contour integral technique as for deriving Eq. 2.7, the method of integration by parts and the following relation: $\sum_n e^{i\omega_n \tau} = \beta\delta(\tau)$ (see Appendix B).

Finally, we see that

$$\Gamma = \beta\Omega. \tag{5.13}$$

The functional Γ provides us with a variational principle. In particular, one can obtain the Dyson equation by demanding $\partial\Gamma/\partial G(i\omega_n) = 0$ and $\partial\Phi/\partial G(i\omega_n) = \Sigma(i\omega_n)$:

$$\frac{\partial\Phi}{\partial G(i\omega_n)} - \Sigma(i\omega_n) - \frac{\partial\Sigma(i\omega_n)}{\partial G(i\omega_n)}G(i\omega_n) + \frac{1}{G(i\omega_n)} = \frac{\partial\Gamma}{\partial G(i\omega_n)} = 0$$

$$\frac{1}{G(i\omega_n)} - \frac{\partial\Sigma(i\omega_n)}{\partial G(i\omega_n)}G(i\omega_n) = 0$$

$$\frac{\partial\Sigma(i\omega_n)}{\partial G(i\omega_n)} = G^{-2}(i\omega_n)$$

$$\Sigma(i\omega_n) = \frac{1}{G_0(i\omega_n)} - \frac{1}{G(i\omega_n)}$$

$$G(i\omega_n) = G_0(i\omega_n) + G_0(i\omega_n)\Sigma(i\omega_n)G(i\omega_n).$$

Using the Luttinger-Ward functional the total particle number N_μ, which is a thermodynamic quantity can be expressed in terms of the thermal Greens function:

$$\begin{aligned}
N_\mu &\equiv -\frac{d\Omega}{d\mu} \\
&= -\frac{1}{\beta}Tr\left(\frac{\partial\Phi}{\partial G(i\omega_n)}\frac{dG(i\omega_n)}{d\mu} - \frac{dG(i\omega_n)}{d\mu}\Sigma(i\omega_n) - \right. \\
&\qquad \left. -\frac{d\Sigma(i\omega_n)}{d\mu}G(i\omega_n) + \frac{1}{G(i\omega_n)}\frac{dG(i\omega_n)}{d\mu}\right) \\
&= -\frac{1}{\beta}Tr\left(-\frac{d(G_0^{-1} - G^{-1})}{d\mu}G(i\omega_n) + \frac{1}{G(i\omega_n)}\frac{dG(i\omega_n)}{d\mu}\right) \\
&= \frac{1}{\beta}Tr\left(\frac{dG_0^{-1}}{d\mu}G(i\omega_n)\right) \\
&= \frac{1}{\beta}Tr\left(\frac{d(i\omega_n - \epsilon + \mu)}{d\mu}G(i\omega_n)\right) \\
&= \frac{1}{\beta}Tr\, G(i\omega_n) \qquad (5.14)
\end{aligned}$$

On the other hand $\frac{1}{\beta}TrG(i\omega_n)$ is "microscopic" definition of the particle number N_{mic}. Thus, the Luttinger-Ward functional yields the consistency between the thermodynamic and "microscopic" particle numbers.

Another quantity we calculate using the functional Γ is the thermodynamic average of the energy:

$$\langle H-\mu N_\mu\rangle = \frac{1}{Z}Tr[(H-\mu N_\mu)e^{-\beta(H-\mu N_\mu)}] = -\frac{d(\log Z)}{d\beta} = \frac{d(\beta\Omega)}{d\beta} =$$

$$= \frac{d}{d\beta}(\Phi[G] - Tr(e^{i\omega_n 0^+}[G(i\omega_n)\Sigma(i\omega_n) + \log(-G(i\omega_n)/\beta)])$$

$$= \frac{\partial\Phi}{\partial G}\frac{dG}{d\beta} - Tr\left(e^{i\omega_n 0^+}\left[\frac{dG}{d\beta}\Sigma - \frac{d\Sigma}{d\beta}G + \frac{d}{d\beta}\log(-G/\beta)\right]\right)$$

Since the Greens function and self-energy obey the variational principle they fulfil the variational conditions and Dyson equation. Hence, the first two terms in the last expression cancel each other

$$\langle H-\mu N_\mu\rangle = Tr\left(e^{i\omega_n 0^+}\left[G\frac{d}{d\beta}(G^{-1}-G_0^{-1}) + \frac{d}{d\beta}\log\left(\frac{-G}{\beta}\right)\right]\right)$$

$$= -Tr\left(e^{i\omega_n 0^+}\left[G^{-1}\frac{dG}{d\beta} + \frac{1}{G}\left(\frac{dG}{d\beta} - \frac{G}{\beta}\right) - G\frac{dG_0^{-1}}{d\beta}\right]\right)$$

$$= -Tr\left(e^{i\omega_n 0^+}\left[\frac{1}{\beta} - G\frac{d}{d\beta}(i\omega_n - \epsilon + \mu)\right]\right)$$

$$= \frac{1}{\beta}\sum_n e^{i\omega_n 0^+}(i\omega_n G(i\omega_n) - 1)$$

This expression can be rewritten in terms of the self-energy if we replace $i\omega_n$ and 1 by $G_0^{-1}(i\omega_n)+\epsilon$ and $G(i\omega_n)/G(i\omega_n)$, respectively:

$$\langle H-\mu N_\mu\rangle = \frac{1}{\beta}\sum_n e^{i\omega_n 0^+}G(i\omega_n)\left(G_0(i\omega_n)^{-1} - G(i\omega_n)^{-1} + \epsilon\right)$$

$$= \frac{1}{\beta}\sum_n e^{i\omega_n 0^+}G(i\omega_n)(\Sigma(i\omega_n) + \epsilon - \mu) \tag{5.15}$$

In order to obtain standard thermodynamic expression for the free energy we compute the entropy:

$$S = -\frac{d\Omega}{dT} = -\frac{d\Omega}{d\beta}\frac{d\beta}{dT} = \frac{d\Omega}{d\beta}\beta^2$$

and write the expectation value of the energy in the following form:

$$E = \langle H\rangle = \frac{d(\beta\Omega)}{d\beta} + \mu\langle N_\mu\rangle = \Omega + \beta\frac{d\Omega}{d\beta} + \mu\langle N_\mu\rangle$$

Using the last two expressions we find

$$E - TS - \mu\langle N_\mu\rangle = \Omega + \beta\frac{d\Omega}{d\beta} + \mu\langle N_\mu\rangle - \frac{1}{\beta}\frac{d\Omega}{d\beta}\beta^2 - \mu\langle N_\mu\rangle = \Omega$$

An important observation regarding the Luttinger-Ward functional made by Baym and Kadanoff is that all correlations computed as variational derivatives of the Γ-functional obey conservation laws of charge, momentum and energy even if Γ includes only a finite number of diagrams [26], [27], [28].

5.2 Generalisation of the Luttinger-Ward Functional Theory

Let us generalize the variational principle and rewrite it in terms of the periodized Greens functions. In order to do this we first put the following demands on the Γ-functional:

- The Γ-functional written in terms of the periodized Greens functions must give ordinary Γ-functional written in terms of the continuous Greens functions, Eq. 5.5, in the limit $N \to \infty$
- The periodized Greens functions must be consistent with the variational principle
- The free energy written in terms of the periodized Greens functions must be exact in the noninteracting limit ($\Sigma \to 0$).

If one just replaces the ordinary Greens functions by periodized ones in Eq. 5.5 the third condition is not fulfilled and therefore the last term in the Γ-functional has to be altered (the first two terms are zero in the non interacting limit). To satisfy the third condition the last term in the Luttinger-Ward functional is modified in the following form:

$$Tr\ \log(-G^-(i\omega_n)/(2\eta)), \quad \eta \equiv \beta/(2N)$$

By definition $G^{\pm}(i\omega_n)$ is equal to $G(i\omega_n) \pm \eta$. It is remarkable that this expression in the non interacting limit yields exact free energy for all values of N:

$$\begin{aligned}
\sum_{n=0}^{N-1} \log(-G_0^-(i\omega_n)/(2\eta)) &= \sum_{n=0}^{N-1} \log\left(\frac{N}{\beta}(-\eta\ \coth\ \eta(i\omega_n - \epsilon) + \eta)\right) \\
&= \sum_{n=0}^{N-1} \log\left(\frac{1}{2}(\coth\ \eta(\epsilon - i\omega_n) + 1)\right) \\
&= \sum_{n=0}^{N-1} \log\frac{1}{2}\left(\frac{e^{\epsilon\beta/(2N)}e^{-i\beta\omega_n/(2N)} + e^{-\beta\epsilon/(2N)}e^{i\beta\omega_n/(2N)}}{e^{\epsilon\beta/(2N)}e^{-i\beta\omega_n/(2N)} - e^{-\beta\epsilon/(2N)}e^{i\beta\omega_n/(2N)}} + 1\right)
\end{aligned}$$

$$= \sum_{n=0}^{N-1} \log \frac{e^{\epsilon\beta/(2N)} e^{-i\beta\omega_n/(2N)}}{e^{\epsilon\beta/(2N)} e^{-i\beta\omega_n/(2N)} - e^{-\beta\epsilon/(2N)} e^{i\beta\omega_n/(2N)}}$$

$$= -\sum_{n=0}^{N-1} \log(1 - e^{-\beta\epsilon/N} e^{i\beta\omega_n/N})$$

$$= -\sum_{n=0}^{N-1} \log(1 - e^{-\beta\epsilon/N} e^{i(2n+1)\pi/N})$$

$$= -\sum_{n=0}^{N-1} \log(1 - e^{(-\beta\epsilon+i\pi)/N} (e^{2i\pi/N})^n)$$

$$= -\log \prod_n (1 - e^{(-\beta\epsilon+i\pi)/N} (e^{2i\pi/N})^n)$$

In order to proceed consider the roots of the polynomial $x^N - a^N$, which are $a(e^{2i\pi/N})^n$. Using the roots one can represent the polynomial in an alternative form: $x^N - a^N \equiv \prod_n (x - a(e^{2i\pi/N})^n)$. If we let x and a to be 1 and $e^{(-\beta\epsilon+i\pi)/N}$, respectively we see that the last expression is equal to

$$\sum_{k,n} \log(-G^-_{0,k}(i\omega_n)/(2\eta)) = -\sum_k \log(1 - e^{-\beta\epsilon_k + i\pi})$$

$$= -\sum_k \log(1 + e^{-\beta\epsilon_k})$$

$$= \beta\Omega_0$$

As the proof shows that $\sum_{k,n} \log(-G_0(i\omega_n)^-/(2\eta))$ is identically equal to the non interacting free energy for any number of discretization points N.

The functional $\Phi[G]$ is interpreted as the same set of diagrams i.e. the sum of all possible closed linked skeleton diagrams, but the lines of the diagrams correspond to the periodized Greens functions $G(i\omega_n)$ except the ones that begin and end at the same vertex which are given by $G^+(i\omega_n) \equiv G(i\omega_n) + \eta$ to properly count particle number, which corresponds to the interpretation of loops being evaluated at $\tau = 0^-$.

By taking into account the modifications to the ordinary Γ-functional we generalize it in the following form:

$$\Gamma = \Phi[G] - Tr(\Sigma(i\omega_n)G^+(i\omega_n)) + Tr\ \log(-G^-(i\omega_n)/(2\eta)) \tag{5.16}$$

The first two terms clearly have the proper limit as $N \to \infty$. Now, consider the last term in the same limit (the pre-factor $e^{i\omega_n 0^+}$ is for convergence in the

$N \to \infty$ limit and also is presented in Eq. 5.5):

$$\begin{aligned}
\lim_{\eta\to 0} Tr\, e^{i\omega_n 0^+} \log\left(-\frac{G^-(i\omega_n)}{2\eta}\right) &= \lim_{N\to\infty} Tr\, e^{i\omega_n 0^+} \log\left(\frac{1}{2} - \frac{N}{\beta} G(i\omega_n)\right) \\
&= \lim_{N\to\infty} Tr\, e^{i\omega_n 0^+} \log\left(-\frac{N}{\beta} G(i\omega_n)\right) \\
&= \lim_{N\to\infty} Tr\, e^{i\omega_n 0^+} \log\left(-\frac{G(i\omega_n)}{\beta}\right) + \\
&\quad + \lim_{N\to\infty} Tr\, e^{i\omega_n 0^+} \log N \\
&= \lim_{N\to\infty} Tr\, e^{i\omega_n 0^+} \log\left(-\frac{G(i\omega_n)}{\beta}\right) + \\
&\quad + \sum_k \lim_{N\to\infty} \beta\delta(0^+) \log N
\end{aligned}$$

here we used the relation$\sum_n e^{i\omega_n \tau} = \beta\delta(\tau)$. The second term in the last expression is zero due to the Dirac delta function $\delta(0^+)\,(=0)$ which is stronger than the logarithmic infinity.

$$\lim_{\eta\to 0} Tr\, e^{i\omega_n 0^+} \log\left(-\frac{G^-(i\omega_n)}{2\eta}\right) = \lim_{N\to\infty} Tr\, e^{i\omega_n 0^+} \log\left(-\frac{G(i\omega_n)}{\beta}\right)$$

The last expression is exactly the third term in Eq. 5.5.

In order to see what result the new Γ-functional yields, we demand two conditions to be satisfied: the variation of Γ and $\Phi[G]$ with respect to $G(i\omega_n)$ is zero and $\Sigma(i\omega_n)$, respectively. The variation of Eq. 5.16 gives:

$$\begin{aligned}
\frac{\partial\Gamma}{\partial G} &= \frac{\partial\Phi}{\partial G} - \frac{\partial\Sigma}{\partial G} G^+ - \Sigma + \frac{1}{G^-} \\
&= -\frac{\partial\Sigma}{\partial G} G^+ + \frac{1}{G^-}.
\end{aligned}$$

Since we demand that the variation of the Γ with respect to G is zero we find the following differential equation for the self-energy:

$$\frac{\partial\Sigma}{\partial G} = \frac{1}{G^+ G^-} = \frac{N}{\beta}\left(\frac{1}{G^-} - \frac{1}{G^+}\right). \tag{5.17}$$

As an initial condition for the equation above we note that $\Sigma(i\omega_n) = 0$ when $G(i\omega_n) = G_0(i\omega_n)$. So the solution to Eq. 5.17 is

$$\Sigma = \frac{N}{\beta} \log\left(\frac{G^-}{G_0^-}\frac{G_0^+}{G^+}\right). \tag{5.18}$$

After inverting this expression we find

$$e^{2\eta\Sigma}(G_0-\eta)(G+\eta)=(G-\eta)(G_0+\eta)$$

$$G[G_0(e^{2\eta\Sigma}-1)-\eta(e^{2\eta\Sigma}+1)]=\eta[\eta(e^{2\eta\Sigma}-1)-G_0(e^{2\eta\Sigma}+1)]$$

$$G=\eta\frac{\eta(e^{2\eta\Sigma}-1)-G_0(e^{2\eta\Sigma}+1)}{G_0(e^{2\eta\Sigma}-1)-\eta(e^{2\eta\Sigma}+1)}$$

$$G(i\omega_n)=\eta\frac{G_0(i\omega_n)-\eta\,\tanh(\eta\Sigma(i\omega_n))}{\eta-G_0(i\omega_n)\,\tanh(\eta\Sigma(i\omega_n))}. \tag{5.19}$$

Performing some trigonometric manipulations on Eq. 5.19 enables us to rewrite it in more familiar form:

$$\begin{aligned}
G&=\eta\frac{G_0-\eta\,\tanh(\eta\Sigma)}{\eta-G_0\,\tanh(\eta\Sigma)}\\
&=\eta\frac{\eta\,\coth\,\eta(i\omega_n-\epsilon)-\eta\,\tanh(\eta\Sigma)}{\eta-\eta\,\coth\,\eta(i\omega_n-\epsilon)\,\tanh(\eta\Sigma)}\\
&=\eta\frac{\coth\,\eta(i\omega_n-\epsilon)-\tanh(\eta\Sigma)}{1-\coth\,\eta(i\omega_n-\epsilon)\,\tanh(\eta\Sigma)}\\
&=\eta\,\coth\,\eta(i\omega_n-\epsilon-\Sigma)
\end{aligned}$$

where we used the following identity:

$$\coth(x-y)=\frac{\coth(x)-\tanh(y)}{1-\coth(x)\tanh(y)}.$$

It is important to note that the variational principle for the "periodized" Luttinger-Ward functional yields Eq. 5.19 which is exactly the same equation as Eq. 4.4 obtained by discretizing the imaginary time Greens function. This shows that the periodized Greens functions are consistent with the corresponding Luttinger-Ward variational principle.

Using the Γ-functional (Eq. 5.16) we approximate the free energy as the value of the Γ evaluated at the self-energy and Greens function obeying "periodized Dyson equation", Eq. 5.19.

The derivation of the particle number N_μ using periodized free energy leads to the following expression:

$$
\begin{aligned}
N_\mu &= -\frac{d\Omega}{d\mu} \\
&= -\frac{1}{\beta} Tr \left(\frac{\partial \Phi}{\partial G} \frac{dG}{d\mu} - \frac{dG}{d\mu}\Sigma - \frac{d\Sigma}{d\mu} G^+ + \frac{1}{G^-}\frac{dG}{d\mu} \right) \\
&= -\frac{1}{\beta} Tr \left(-\frac{d}{d\mu} \left(\frac{N}{\beta} \left(\log \frac{G^-}{G^+} + \log \frac{G_0^+}{G_0^-} \right) \right) G^+ + \frac{1}{G^-}\frac{dG}{d\mu} \right) \\
&= \frac{1}{\beta} Tr \left(\frac{N}{\beta} \left(G^+ \frac{1}{G_0^- G_0^+} \frac{dG_0}{d\mu} \left(-\frac{\beta}{N} \right) + G^+ \frac{1}{G^- G^+} \frac{dG}{d\mu} \frac{\beta}{N} \right) - \frac{1}{G^-}\frac{dG}{d\mu} \right) \\
&= -\frac{1}{\beta} Tr \left(G^+ \frac{1}{G_0^- G_0^+} \frac{dG_0}{d\mu} \right) \\
&= \frac{1}{\beta} Tr \left(G^+ \frac{1}{\eta^2 (\coth^2 \eta(i\omega_n - \epsilon + \mu) - 1)} \frac{\eta^2}{\sinh^2 \eta(i\omega_n - \epsilon + \mu)} \right) \\
&= \frac{1}{\beta} Tr\, G^+(i\omega_n)
\end{aligned}
$$

Let us check that this corresponds to the "microscopic" definition of N_μ. According to our definition of the discterized imaginary time Greens function at $\tau_j = 0$ we have:

$$G_k(\tau_j = 0) = n_k - \frac{1}{2} = \frac{1}{\beta} \sum_{n=0}^{N-1} G_k(i\omega_n)$$

In order to get the particle number one has to add a half to the both sides of the equation:

$$
\begin{aligned}
N_\mu = \sum_k n_k &= \sum_k \left(\frac{1}{2} + \frac{1}{\beta} \sum_{n=0}^{N-1} G_k(i\omega_n) \right) \\
&= \sum_k \left(\frac{1}{\beta} \sum_{n=0}^{N-1} \left(G_k(i\omega_n) + \frac{\beta}{2N} \right) \right) \\
&= \frac{1}{\beta} Tr\, G_k^+(i\omega_n).
\end{aligned}
$$

As one can see the thermodynamic and "microscopic" definitions of the particle number N_μ give same results which reduce to the standard expression Eq. 5.14 in the limit $\eta \to 0$.

Now we show that we have a corresponding definition of the energy by computing the expectation value of the Hamiltonian (see Appendix C for complete derivation):

$$\langle H - \mu N_\mu \rangle = \frac{1}{Z} Tr[(H - \mu N_\mu) e^{-\beta(H-\mu N_\mu)}]$$

$$= -\frac{d(\log Z)}{d\beta} = \frac{d(\beta\Omega)}{d\beta} =$$

$$= \frac{d}{d\beta}(\Phi[G] - Tr\, G^+(i\omega_n)\Sigma(i\omega_n) + Tr(\log(-G^-(i\omega_n)/2\eta)))$$

$$= \frac{1}{\beta} Tr\,[G(i\omega_n)(\Sigma(i\omega_n) + \epsilon - \mu) + \eta(\epsilon - \mu)]$$

The comparison of the latter to its standard counterpart 5.15 shows that it is a same expression except a contribution of $\eta\epsilon$ inside trace which vanishes in the limit $\eta \to 0$.

Note that during these derivations we imply that the Γ-functional is equal to $\beta\Omega$, which means that the self-energy and Greens function obey Eq. 5.19 and $\partial\Phi/\partial G = \Sigma$.

Chapter 6

Single-Particle Spectral Function

We now turn to the properties of the periodized Greens function. Suppressing the quantum index k ($A_k(\omega) \equiv A(\omega)$) we write it in the spectral representation by discretising imaginary time in Eq. 3.18 and then performing discrete Fourier transform taking into account Eq. 4.3:

$$G(i\omega_n) = \int_{-\infty}^{\infty} \frac{d\omega}{2\pi} A(\omega)\eta \coth \eta(i\omega_n - \omega) \tag{6.1}$$

where $A(\omega)$ is the spectral function, which is given in a standard form by

$$A(\omega) = \frac{1}{Z}\sum_{m,n} |\langle m|c^\dagger|n\rangle|^2 e^{-\beta E_n}(1 + e^{-\beta\omega})2\pi\delta(E_m - E_n - \omega). \tag{6.2}$$

Here we define $|n\rangle$ to be a complete set of eigenstates, $H|n\rangle = E_n|n\rangle$. Eq. 6.1 provides the analytic continuation for the periodized Greens function by letting $i\omega_n \to z$, z is the complex variable. Since coth $\eta(z - \omega)$ diverges at $z - \omega = in\pi/\eta$ and ω is real, $G(z)$ is analytic except where $Im(z)$ is an integer multiple of $\Omega_N = \pi/\eta$.

Defining $G(z = \omega + i0^+) \equiv G^R(\omega)$, $G(z = \omega + i0^-) \equiv G^A(\omega)$ and $\Sigma(\omega \pm i0^+) \equiv \Sigma^{R/A}(\omega)$ in analogy with the retarded and advanced Greens functions in the standard formalism and using the relations:

$$\lim_{\delta\to 0^+} \eta Im[\coth \eta(\omega + i\delta - \omega')] = \lim_{\delta\to 0^+} -\eta \frac{\sin(2\eta\delta)}{\cosh 2\eta(\omega - \omega') - \cos(2\eta\delta)} = -\pi\delta(\omega - \omega')$$

and

$$\coth(x - iy) = \frac{\cos(y)\cosh(x) - i\sin(y)\sinh(x)}{\cos(y)\sinh(x) - i\sin(y)\cosh(x)} \tag{6.3}$$

$$= \frac{\cosh(x)\sinh(x) + i\cos(y)\sin(y)}{\cosh^2(x) - \cos^2(y)} \tag{6.4}$$

we find that the spectral weight is given by the imaginary part of $G^{A/R}(\omega)$:

$$A(\omega) = \pm 2ImG^{A/R}(\omega) = \pm 2Im[\eta \coth \eta(\omega - \epsilon - \Sigma^{A/R}(\omega))]$$

$$= \pm 2\eta \frac{\cos(\eta Im[\Sigma^{A/R}(\omega)]) \sin(\eta Im[\Sigma^{A/R}(\omega)])}{\cosh^2 \eta(\omega - \epsilon - Re[\Sigma^{A/R}(\omega)]) - \cos^2 \eta(Im[\Sigma^{A/R}(\omega)])}$$

$$= \pm 2\eta \frac{\sin(2\eta Im[\Sigma^{A/R}(\omega)])}{\cosh 2\eta(\omega - \epsilon - Re[\Sigma^{A/R}(\omega)]) - \cos 2\eta(Im[\Sigma^{A/R}(\omega)])}$$

In the limit $\eta \to 0$ the spectral weight is

$$A(\omega) = \pm 2\eta \frac{2\eta Im[\Sigma^{A/R}(\omega)]}{1 + \frac{1}{2}(2\eta(\omega - \epsilon - Re[\Sigma^{A/R}(\omega)]))^2 - 1 + \frac{1}{2}(2\eta(Im[\Sigma^{A/R}(\omega)]))^2}$$

$$= \pm \frac{2Im[\Sigma^{A/R}(\omega)]}{(\omega - \epsilon - Re[\Sigma^{A/R}(\omega)])^2 + Im[\Sigma^{A/R}(\omega)]^2}$$

It follows that $-\Sigma^R(\omega) = \Sigma^A(\omega)$. So that $\Sigma(z)$ has a branch cut on the lines $Im(z) = n\Omega_N, n \in Z$ which coincides the real axis when $n = 0$.

By extracting the real part from the $G^R(\omega)$ and using the identity:

$$\frac{\sinh(x)}{\cosh(x) - 1} = \frac{e^x - e^{-x}}{e^x + e^{-x} - 2} = \frac{(e^{x/2} - e^{-x/2})(e^{x/2} + e^{-x/2})}{(e^{x/2} - e^{-x/2})^2} = \coth\left(\frac{x}{2}\right)$$

one obtains a generalized Kramers-Kronig relation:

$$Re[G^R(\omega)] = \int \frac{d\omega'}{2\pi} A(\omega')\, \eta\, Re[\coth\, \eta(\omega - \omega' + i0^+)]$$

$$= \frac{\eta}{2\pi} P \int d\omega' A(\omega') \frac{\sinh 2\eta(\omega - \omega')}{\cosh 2\eta(\omega - \omega') - \cos(2\eta 0^+)}$$

$$= -\frac{\eta}{\pi} P \int d\omega' ImG^R(\omega') \frac{\sinh 2\eta(\omega - \omega')}{\cosh 2\eta(\omega - \omega') - \cos(2\eta 0^+)}$$

$$= -\frac{\eta}{\pi} P \int d\omega' ImG^R(\omega') \frac{\sinh 2\eta(\omega - \omega')}{\cosh 2\eta(\omega - \omega') - 1}$$

$$= -\frac{\eta}{\pi} P \int d\omega' \frac{Im[G^R(\omega')]}{\tanh\, \eta(\omega - \omega')}$$

which reduces to the standard expression in the limit $\eta \to 0$:

$$\lim_{\eta\to 0} ReG^R(\omega) = -\frac{\eta}{\pi} P\int d\omega' \frac{Im[G^R(\omega')]}{\eta(\omega-\omega')}$$

$$= -\frac{1}{\pi} P\int d\omega' \frac{Im[G^R(\omega')]}{\omega-\omega'}$$

6.1 Spectral Function Ansatz

We model the spectral function with the following function:

$$L_{\epsilon,\gamma}(\omega) = \frac{i\eta}{\sinh\,\eta(\omega-\epsilon+i\gamma)} - \frac{i\eta}{\sinh\,\eta(\omega-\epsilon-i\gamma)}$$

which reduces to the Eq. 3.20 in the limit $\eta \to 0$. In order, $L_{\epsilon,\gamma}(\omega)$ to be positively defined, the real part of the first term should be positive because $L_{\epsilon,\gamma}(\omega)$ is a sum of two complex conjugate terms.

$$Re\left[\frac{i\eta}{\sinh\,\eta(\omega-\epsilon+i\gamma)}\right] = Re\left[\frac{i\eta}{\sinh\,\eta(\omega-\epsilon)\cos(\eta\gamma) + i\,\cosh\,\eta(\omega-\epsilon)\sin(\eta\gamma)}\right]$$

$$= \frac{\eta\cosh\,\eta(\omega-\epsilon)\sin(\eta\gamma)}{\sinh^2\eta(\omega-\epsilon)\cos^2(\eta\gamma) + \cosh^2\eta(\omega-\epsilon)\sin^2(\eta\gamma)} > 0$$

This condition together with the fact that $\sin(x)$ is symmetric around $\pi/2$ requires that $0 < \gamma < \Omega_N/2$.

Now, let us insert $L_{\epsilon,\gamma}(\omega)$ in Eq. 6.1 and perform the integration for $0 < Im[z] < \Omega_N$ using the periodicity and anti-periodicity of $\coth(z)$ and $L_{\epsilon,\gamma}(z)$, respectively (see Fig. 6.1):

$$G(z) = \int_{-\infty}^{\infty} \frac{d\omega}{2\pi} L_{\epsilon,\gamma}(\omega)\,\eta\,\coth\,\eta(z-\omega)$$

$$= \frac{1}{2}\oint_C \frac{dz'}{2\pi} L_{\epsilon,\gamma}(z')\,\eta\,\coth\,\eta(z-z'). \tag{6.5}$$

As shown in Fig. 6.1, there are exactly three poles to consider, z_i' $(i = 1, 2, 3)$ residing in the strip $0 < Im[z] < \Omega_N$. The Greens function is analytic in the strip $0 < Im[z] < \Omega_N$ and has poles outside the strip at $\epsilon - i\gamma$ and $\epsilon + i\gamma + i\Omega_N$

with the period of $2i\Omega_n$ (see. Fig. 8.2 a).

$$
\begin{aligned}
G(z) &= \frac{i\eta}{2}\sum_{i=1}^{3} Res_{z'=z'_i}[\coth\,\eta(z-z')L_{\epsilon,\gamma}(z')] \\
&= \frac{i\eta}{2}\left(-\frac{1}{\eta}L_{\epsilon,\gamma}(z) - i\,\coth\,\eta(z-z_2) - i\,\coth\,\eta(z-z_3)\right) \\
&= \frac{\eta}{2}\left(\coth\,\eta(z-\epsilon+i\gamma) + \coth\,\eta(z-\epsilon-i\gamma) + \right. \\
&\qquad \left. +1/\sinh(\eta(z-\epsilon+i\gamma)) - 1/\sinh(\eta(z-\epsilon-i\gamma))\right) \qquad (6.6) \\
&= \frac{\eta}{2}\left(\coth\frac{\eta}{2}(z-\epsilon+i\gamma) + \tanh\frac{\eta}{2}(z-\epsilon-i\gamma)\right).
\end{aligned}
$$

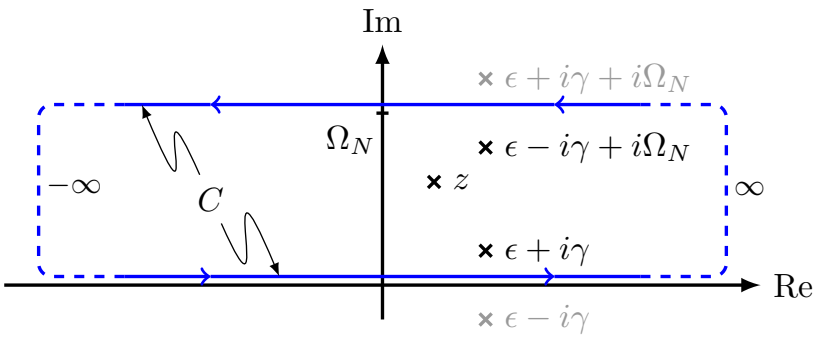

Figure 6.1: Contour for the integration of Eq. 6.5

were we used the identity

$$\coth(x) + \frac{1}{\sinh(x)} = \coth\left(\frac{x}{2}\right)$$

$$\coth(x) - \frac{1}{\sinh(x)} = \tanh\left(\frac{x}{2}\right).$$

In the limit $\eta \to 0$ the function $G(z)$ reduces to the usual retarded Greens function $1/(z-\epsilon+i\gamma)$ obtained by an ordinary Lorentzian spectral weight. If we evaluate the contour integral for the strip $-\Omega_N < Im[z] < 0$, which corresponds to the change of the sign of the inverse hyperbolic sine functions in Eq. 6.6, we find:

$$G(z) = \frac{\eta}{2}\left(\tanh\frac{\eta}{2}(z-\epsilon+i\gamma) + \coth\frac{\eta}{2}(z-\epsilon-i\gamma)\right)$$

which gives the ordinary advanced Greens function $1/(z-\epsilon-i\gamma)$ in the limit $\eta \to 0$. The Greens function $G(z)$ has the branch cuts repeated with the period

of $i\Omega_N$. The analytic Greens function can be obtained by cutting out those branches where $G(z)$ has the poles and then gluing together the branches where $G(z)$ is analytic (see. Fig. 8.2 b). In the limit $\eta \to 0$ $\Omega_N = \pi/\eta$ becomes infinitely large and therefore $G(z)$ has a branch cut on the real axis corresponding to the standard formalism.

Using the same contour as in Fig. 6.1 it can be shown that $L_{\epsilon,\gamma}(\omega)$ is properly normalised:

$$\begin{aligned}\int_{-\infty}^{\infty} \frac{d\omega}{2\pi} L_{\epsilon,\gamma}(\omega) &= \frac{1}{2} \oint_C \frac{dz}{2\pi} L_{\epsilon,\gamma}(z) \\ &= \frac{i}{2} \sum_{i=1}^{2} \lim_{z\to z_i} (z - z_i) \left(\frac{i\eta}{\sinh\, \eta(\omega - \epsilon + i\gamma)} - \frac{i\eta}{\sinh\, \eta(\omega - \epsilon - i\gamma)} \right) \\ &= \frac{i}{2} \left(-i\eta \frac{1}{\eta} - i\eta \frac{1}{\eta} \right) = 1\end{aligned}$$

$z_1 = \epsilon + i\gamma$ and $z_2 = \epsilon - i\gamma + i\Omega_N$ are the poles of $L_{\epsilon,\gamma}(z)$ in the strip $0 < Im[z] < \Omega_N$.

Let us now model the spectral function with a sum of the functions $L_{\epsilon_\nu,\gamma_\nu}$. In this case, for the interval $0 < Im[z] < \Omega_N$, $G(z)$ can be written as

$$G(z) = \frac{\eta}{2} \sum_{\nu} \left[a_\nu \coth \frac{\eta}{2}(z - \epsilon_\nu + i\gamma_\nu) + a_\nu^* \tanh \frac{\eta}{2}(z - \epsilon_\nu - i\gamma_\nu) \right] \qquad (6.7)$$

Taking the limit in the latter expression gives:

$$\lim_{z\to\infty} G(z) = \frac{\eta}{2} \sum_{\nu} [a_\nu + a_\nu^*]$$

On the other hand Eq. 6.1 yields:

$$\lim_{z\to\infty} G(z) = \eta \int_{-\infty}^{\infty} \frac{d\omega}{2\pi} A(\omega) = \eta$$

By combining the last two results we find that in order the total spectral weight to be properly normalised a_ν coefficients must satisfy $\sum_\nu (a_\nu + a_\nu^*) = 2$.

Next we derive the expression for the spectral function using

$$\begin{aligned}\tanh(x - iy) &= \frac{\sinh(x)\cos(y) - i\, \cosh(x)\sin(y)}{\cosh(x)\cos(y) - i\, \sinh(x)\sin(y)} \\ &= \frac{\cosh(x)\sinh(x) - i\, \cos(b)\sin(b)}{\cosh^2(x) + \cos^2(y) - 1}\end{aligned}$$

and Eq. 6.7, 6.3.

$$
\begin{aligned}
A(\omega) &= -2Im[G^R(\omega)] \\
&= -\eta \sum_\nu Im \left(a_\nu \frac{\cosh \frac{\eta}{2}(\omega-\epsilon_\nu)\sinh \frac{\eta}{2}(\omega-\epsilon_\nu) - i\,\cos(\frac{\eta}{2}\gamma_\nu)\sin(\frac{\eta}{2}\gamma_\nu)}{\cosh^2 \frac{\eta}{2}(\omega-\epsilon_\nu) - \cos^2(\frac{\eta}{2}\gamma_\nu)} \right. \\
&\qquad \left. + a_\nu^* \frac{\cosh \frac{\eta}{2}(\omega-\epsilon_\nu)\sinh \frac{\eta}{2}(\omega-\epsilon_\nu) - i\,\cos(\frac{\eta}{2}\gamma_\nu)\sin(\frac{\eta}{2}\gamma_\nu)}{\cosh^2 \frac{\eta}{2}(\omega-\epsilon_\nu) + \cos^2(\frac{\eta}{2}\gamma_\nu) - 1} \right) \\
&= -\eta \sum_\nu \left(-Re[a_\nu]\, M + Im[a_\nu]\, N \right)
\end{aligned}
$$

where the factors M and N are :

$$
\begin{aligned}
M &\equiv \frac{\cos(\frac{\eta}{2}\gamma_\nu)\sin(\frac{\eta}{2}\gamma_\nu)}{\cosh^2 \frac{\eta}{2}(\omega-\epsilon_\nu) - \cos^2(\frac{\eta}{2}\gamma_\nu)} + \frac{\cos(\frac{\eta}{2}\gamma_\nu)\sin(\frac{\eta}{2}\gamma_\nu)}{\cosh^2 \frac{\eta}{2}(\omega-\epsilon_\nu) + \cos^2(\frac{\eta}{2}\gamma_\nu) - 1} \\
&= \frac{1}{2} \frac{\cosh\, \eta(\omega-\epsilon_\nu)\, \sin(\eta\gamma_\nu)}{\cosh^2 \frac{\eta}{2}(\omega-\epsilon_\nu)(\cosh^2 \frac{\eta}{2}(\omega-\epsilon_\nu) - 1) + \cos^2(\frac{\eta}{2}\gamma_\nu)(1-\cos^2(\frac{\eta}{2}\gamma_\nu))} \\
&= \frac{1}{2} \frac{\cosh\, \eta(\omega-\epsilon_\nu)\, \sin(\eta\gamma_\nu)}{\frac{1}{4}\sinh^2 \eta(\omega-\epsilon_\nu) + \frac{1}{4}\sin^2(\eta\gamma_\nu)} \\
&= 2 \frac{\cosh\, \eta(\omega-\epsilon_\nu)\, \sin(\eta\gamma_\nu)}{\sinh^2 \eta(\omega-\epsilon_\nu) + \sin^2(\eta\gamma_\nu)}
\end{aligned}
$$

$$
\begin{aligned}
N &\equiv \frac{\cosh \frac{\eta}{2}(\omega-\epsilon_\nu)\sinh \frac{\eta}{2}(\omega-\epsilon_\nu)}{\cosh^2 \frac{\eta}{2}(\omega-\epsilon_\nu) - \cos^2(\frac{\eta}{2}\gamma_\nu)} - \frac{\cosh \frac{\eta}{2}(\omega-\epsilon_\nu)\sinh \frac{\eta}{2}(\omega-\epsilon_\nu)}{\cosh^2 \frac{\eta}{2}(\omega-\epsilon_\nu) + \cos^2(\frac{\eta}{2}\gamma_\nu) - 1} \\
&= \frac{1}{2} \frac{\sinh\, \eta(\omega-\epsilon_\nu)\, \cos(\eta\gamma_\nu)}{\frac{1}{4}\sinh^2 \eta(\omega-\epsilon_\nu) + \frac{1}{4}\sin^2(\eta\gamma_\nu)} \\
&= 2 \frac{\sinh\, \eta(\omega-\epsilon_\nu)\, \cos(\eta\gamma_\nu)}{\sinh^2 \eta(\omega-\epsilon_\nu) + \sin^2(\eta\gamma_\nu)}.
\end{aligned}
$$

Inserting M and N in the expression for the spectral weight gives:

$$A(\omega) = 2\eta \sum_\nu \frac{Re[a_\nu]\cosh\,\eta(\omega-\epsilon_\nu)\,\sin(\eta\gamma_\nu) - Im[a_\nu]\sinh\,\eta(\omega-\epsilon_\nu)\,\cos(\eta\gamma_\nu)}{\frac{1}{2}\cosh\,2\eta(\omega-\epsilon_\nu) - \frac{1}{2} + \frac{1}{2} - \frac{1}{2}\cos(2\eta\gamma_\nu)}$$

$$= 4\eta \sum_\nu \frac{Re[a_\nu]\cosh\,\eta(\omega-\epsilon_\nu)\,\sin(\eta\gamma_\nu) - Im[a_\nu]\sinh\,\eta(\omega-\epsilon_\nu)\,\cos(\eta\gamma_\nu)}{\cosh\,2\eta(\omega-\epsilon_\nu) - \cos(2\eta\gamma_\nu)} \tag{6.8}$$

$$A(\omega) \xrightarrow{\eta\to 0} 4\eta \sum_\nu \frac{Re[a_\nu]\,\eta\gamma_\nu - Im[a_\nu]\,\eta(\omega-\epsilon_\nu)}{1+\frac{1}{2}(2\eta(\omega-\epsilon_\nu))^2 - 1 + \frac{1}{2}(2\eta\gamma_\nu)^2}$$

$$= 2\sum_\nu \frac{Re[a_\nu]\,\gamma_\nu - Im[a_\nu]\,(\omega-\epsilon_\nu)}{(\omega-\epsilon_\nu)^2+\gamma_\nu^2} \tag{6.9}$$

6.2 Padé Method

To compute $G(\omega)$ one has to know coefficients $a_\nu, \epsilon_\nu, \gamma_\nu$ which are unknown so far. Below we describe a procedure which enables us to compute those coefficients: we start with the fitting of given Greens function values at some Matsubara frequencies $G_n \equiv G(i\omega_n)$ to Eq. 6.7. Since the Greens function is represented as a sum of the hyperbolic functions with periodically repeated poles we rewrite it as a sum of simple poles by means of the transformation

$$z' = \coth\left(\frac{\eta}{2}z - i\frac{\pi}{4}\right)$$

We perform transformation term by term using the identity $\coth(x+y) = (1+\coth(x)\coth(y))/(\coth(x)+\coth(y))$:

$$a_\nu \coth\frac{\eta}{2}\left(z - \frac{i\pi}{2\eta} - \epsilon_\nu + i\gamma_\nu + \frac{i\pi}{2\eta}\right) = a_\nu \frac{1+\coth(\frac{\eta}{2}z - \frac{i\pi}{4})\coth(\frac{\eta}{2}(-\epsilon_\nu+i\gamma_\nu)+\frac{i\pi}{4})}{\coth(\frac{\eta}{2}z-\frac{i\pi}{4}) + \coth(\frac{\eta}{2}(-\epsilon_\nu+i\gamma_\nu)+\frac{i\pi}{4})}$$

$$= a_\nu \frac{1-p_\nu z'}{z'-p_\nu}$$

$$a_\nu^* \tanh\frac{\eta}{2}\left(z-\frac{i\pi}{2\eta}-\epsilon_\nu-i\gamma_\nu+\frac{i\pi}{2\eta}\right) = a_\nu^*\frac{\coth(\frac{\eta}{2}z-\frac{i\pi}{4})+\coth(\frac{i\pi}{4}-\frac{\eta}{2}(\epsilon_\nu+i\gamma_\nu))}{1+\coth(\frac{\eta}{2}z-\frac{i\pi}{4})\coth(\frac{i\pi}{4}-\frac{\eta}{2}(\epsilon_\nu+i\gamma_\nu))}$$

$$= a_\nu^*\frac{z'-\coth(\frac{\eta}{2}(\epsilon_\nu+i\gamma_\nu)+\frac{i\pi}{4}-2\frac{i\pi}{4})}{1-z'\coth(\frac{\eta}{2}(\epsilon_\nu+i\gamma_\nu)+\frac{i\pi}{4}-2\frac{i\pi}{4})}$$

$$= a_\nu^*\frac{z'-\frac{1}{\coth(\frac{\eta}{2}(\epsilon_\nu+i\gamma_\nu)+i\frac{\pi}{4})}}{1-\frac{z'}{\coth(\frac{\eta}{2}(\epsilon_\nu+i\gamma_\nu)+i\frac{\pi}{4})}}$$

$$= a_\nu^*\frac{1-p_\nu^* z'}{z'-p_\nu^*}$$

where $p_\nu = \coth\left(\frac{\eta}{2}(\epsilon_\nu - i\gamma_\nu) - i\frac{\pi}{4}\right)$ is the pole in the z' basis. By combining the last two results we find

$$G(z') = \frac{\eta}{2}\sum_{\nu=1}^{n}\left(a_\nu\frac{1-p_\nu z'}{z'-p_\nu}+a_\nu^*\frac{1-p_\nu^* z'}{z'-p_\nu^*}\right) \tag{6.10}$$

After fitting given Greens function values G_n to Eq. 6.10 and computing the poles p_ν and residues $a_\nu(1-p_\nu^2)$ one can identify all unknown coefficients in Eq. 6.7. The transformation maps the domains containing the singularities of $G(z)$ to the unit circle in the z' basis, whereas the domains with no singularities ($0 < Im[z] < \Omega_N$, $2\Omega_N < Im[z] < 3\Omega_N$, $4\Omega_N < Im[z] < 5\Omega_N$, ...) are mapped outside the unit circle (see Fig. 6.2). Note that $z = \pm\infty$ and $z = i\omega_{(N-1)/2}$ map to $z' = \pm 1$ and $z' = \infty$, respectively.

$$z' = \coth\left(\frac{\eta}{2}\,i\frac{\pi}{\beta}((N-1)+1) - i\frac{\pi}{4}\right) = \coth\left(\frac{\beta}{4N}\,i\frac{\pi}{\beta}N - i\frac{\pi}{4}\right) = \coth(0) = \infty$$

Since $G(z'=\infty)$ is equal to $-\frac{\eta}{2}(a_\nu p_\nu + a_\nu^* p_\nu^*)$ Eq. 6.10 is equivalent to the following:

$$G(z') = const + \frac{P(z')}{Q(z')} = const + \frac{a_0 + a_1 z' + ... + a_M (z')^M}{1 + b_1 z' + b_2 (z')^2 + ... + b_{M+1}(z')^{M+1}} \tag{6.11}$$

where $const = -\frac{\eta}{2}(a_\nu p_\nu + a_\nu^* p_\nu^*)$ and $P(z')$ is an Mth order polynomial and $Q(z')$ is an $M+1$th order polynomial. Eq. 6.11 therefore fulfills the boundary condition at infinity:

$$G(z'=\infty) = const = G_{(N-1)/2}.$$

Since $z' = \infty$ corresponds to $i\omega_{(N-1)/2}$ in z basis it is important to pick N to be odd. We also demand

$$G(z'=1) = -G(z'=-1) = \frac{\eta}{2}\sum_\nu (a_\nu + a_\nu^*) = \eta \tag{6.12}$$

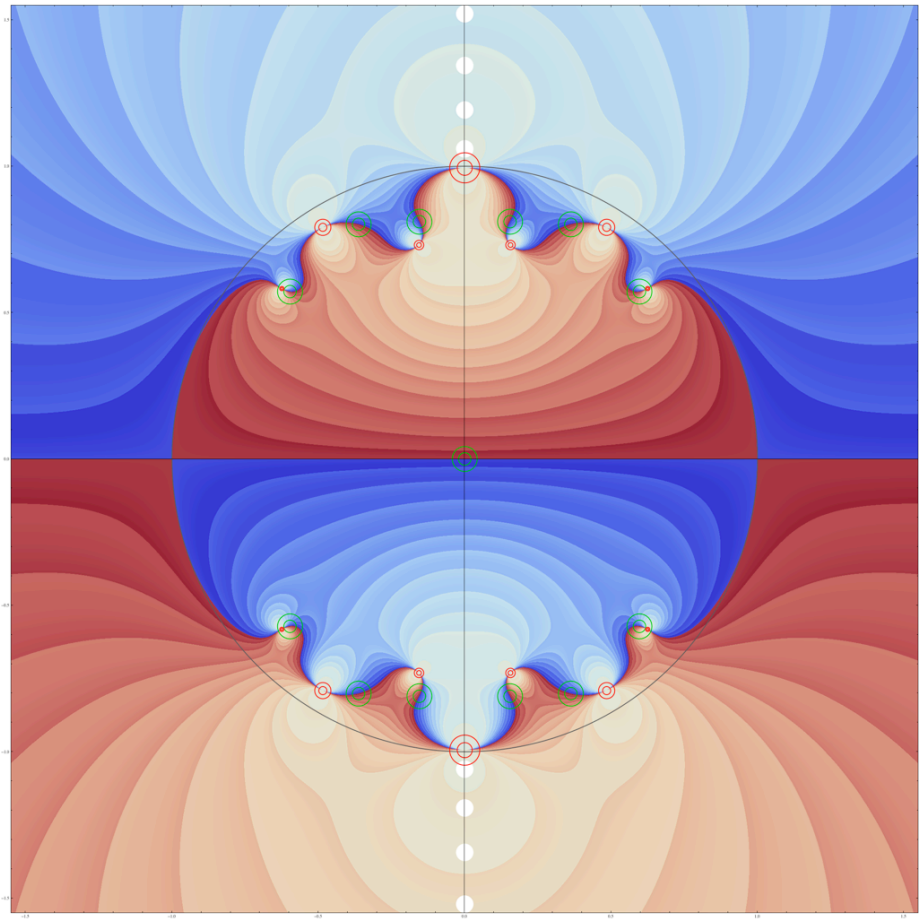

Figure 6.2: Greens function in the z' basis. White dots represent Matsubara frequencies while red circles - poles of the Greens function.

which ensures the proper normalisation of the total spectral weight. This requirement is analytically fulfilled by Eq. 4.8 independent of the self-energy $\Sigma(i\omega_n)$ so that the total spectral weight is conserved within the periodized Dyson equation.

It turns out that one can also put a constraint on the first derivative of $G(z')$ by considering z as a function of z'

$$z = \frac{2}{\eta}\left(\tanh^{-1}(z') + i\frac{\pi}{4}\right).$$

Taking the derivative of Eq. 6.1 with respect to z' we find

$$\frac{dG}{dz'} = \int_{-\infty}^{\infty} \frac{d\omega}{2\pi} A(\omega)\eta \frac{2}{\sinh^2\left(\log\left(\frac{1+z'}{1-z'}\right) + i\frac{\pi}{2} - \eta\omega\right)((z')^2 - 1)}$$

which vanishes in the limit $z' \to \pm 1$

$$\left.\frac{dG}{dz'}\right|_{z'=\pm 1} = 0. \tag{6.13}$$

Now, let us insert Eq. 6.11 in the latter equation and find what are the consequent requirements on the polynomials $P(z')$ and $Q(z')$:

$$\begin{aligned}
&\frac{1}{Q(z')}\left(\frac{dP}{dz'} - \frac{P(z')}{Q(z')}\frac{dQ}{dz'}\right)\Bigg|_{z'=\pm 1} = 0 \\
&\left.\frac{dP}{dz'}\right|_{z'=\pm 1} = \left.\frac{P(z')}{Q(z')}\frac{dQ}{dz'}\right|_{z'=\pm 1} \\
&\left.\frac{dP}{dz'}\right|_{z'=\pm 1} = (\pm\eta - G_{(N-1)/2})\left.\frac{dQ}{dz'}\right|_{z'=\pm 1}.
\end{aligned}$$

Next step is to fit $G(z') - G_{(N-1)/2}$ to $P(z')/Q(z')$ which implies to solve a set of equations for the coefficients of $P(z')$ and $Q(z')$ polynomials. The total number of equations and data points is $N+3$: originally we have N data points, then we drop $G_{(N-1)/2}$, because it is already taken into account in Eq. 6.11, and add η, $-\eta$ (Eq. 6.12) and two zeros (Eq. 6.13). After solving those equations we get an equal number of coefficients for both $P(z')$ and $Q(z')$ polynomials. So, the order of the denominator is $M+1 = (N+3)/2$. Since we also have the symmetry $G(i\omega_{N-1-n}) = G^*(i\omega_n)$ the roots of $Q(z')$ (the poles of $G(z')$) come in complex conjugate pairs. Thus, there are $(M+1)/2$ independent poles and residues and ν, in Eq. 6.10, runs from 1 through $(N+3)/4$. Defining the roots of $Q(z')$ by p_ν and the corresponding residues of $P(z')/Q(z')$ by $a_\nu(1-p_\nu^2)$ we can extract a_ν, γ_ν and ϵ_ν, which enables us to evaluate the spectral weight function (Eq. 6.8 and 6.9).

Since this procedure conserves the total spectral weight we will show that it also preserves the discontinuity at $\tau = 0$:

$$\begin{aligned}
G(\tau = 0^-) &= \frac{1}{\beta}\sum_n e^{-i\omega_n 0^-} G(i\omega_n) \\
&= \frac{1}{2\pi i}\left(\oint_{C_1} dz \frac{e^{-z0^-}}{e^{\beta z}+1} G^R(z) + \oint_{C_2} dz \frac{e^{-z0^-}}{e^{\beta z}+1} G^A(z)\right) \\
&= \frac{1}{2\pi i}\int_{-\infty}^{\infty} d\omega \frac{1}{e^{\beta\omega}+1}(-G^R(\omega) + G^A(\omega)) \\
&= \frac{1}{2\pi i}\int_{-\infty}^{\infty} d\omega\, n_f i A(\omega) \\
&= \int_{-\infty}^{\infty} \frac{d\omega}{2\pi}\, n_f A(\omega)
\end{aligned} \tag{6.14}$$

here we used the function $1/(e^{\beta z}+1)$ which has the poles exactly at the Matsubara frequencies with residues $-1/\beta$. It makes sure that the integrand converges at infinity and enables us to deform the contours C_1 and C_2 shown on Fig. 6.3 (a) into the ones shown on Fig. 6.3 (b). By analogy we compute $G(\tau = 0^+)$. The only difference is that in this case we use $1/(e^{-\beta z}+1)$ instead of $1/(e^{\beta z}+1)$ to make the integrand converge at $z = -\infty$:

$$G(\tau = 0^+) = \frac{1}{\beta}\sum_n e^{-i\omega_n 0^+} G(i\omega_n) = \frac{1}{2\pi i}\oint_C dz \frac{e^{-z0^+}}{e^{-\beta z}+1} G(z)$$

$$= \frac{1}{2\pi i}\int_{-\infty}^{\infty} d\omega \, \frac{1}{e^{-\beta\omega}+1} iA(\omega)$$

$$= \int_{-\infty}^{\infty} \frac{d\omega}{2\pi}\,(n_f - 1)A(\omega) \tag{6.15}$$

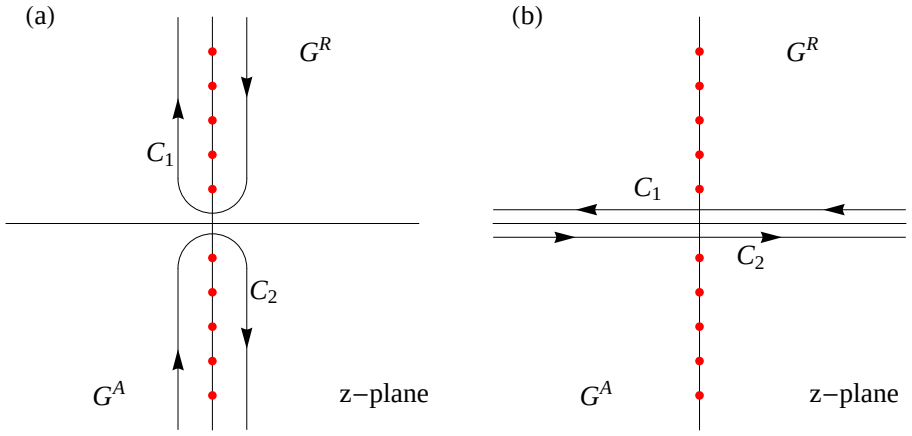

Figure 6.3: The indicated points are the Matsubara frequencies ω_n

After subtracting $G(\tau = 0^+)$ from $G(\tau = 0^-)$ one finds

$$G(\tau = 0^-) - G(\tau = 0^+) = \int_{-\infty}^{\infty} \frac{d\omega}{2\pi} A(\omega) = 1$$

which is the demonstration of the imaginary time Greens function discontinuity at $\tau = 0$.

APPLICATIONS

Chapter 7

Interaction Effects in Bilayer Graphene

We use the periodized Greens function formalism to study the Coulomb interaction effects in bilayer graphene in RPA and fully self-consistent approximation but first let us present the tight-binding description of the mono and bi-layer graphene.

7.1 Tight-Binding Approximation

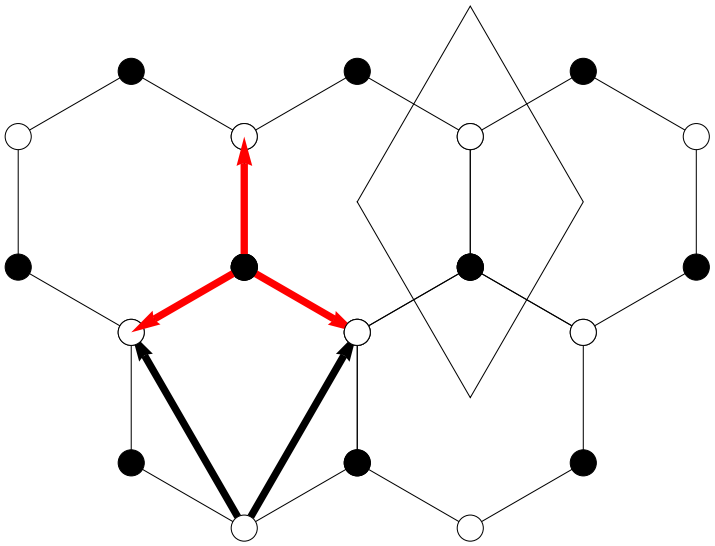

Figure 7.1: Monolayer graphene lattice structure. White and black dots denote carbon atoms residing on the different triangular sublattices.

Simplest way to describe graphene is to start with the corresponding tight-binding model. In order to write Hamiltonian in the tight-binding approxima-

tion creation and annihilation operators are introduced: $a^{\dagger}_{\sigma,\mathbf{R_i}}$ ($b^{\dagger}_{\sigma,\mathbf{R_i}}$) creates an electron at site $\mathbf{R_i}$ on sublattice A-white dots (B-black dots) on Fig. 7.1 with spin σ, while $a_{\sigma,\mathbf{R_i}}$ ($b_{\sigma,\mathbf{R_i}}$) annihilates it. The non-interacting Hamiltonian has the following form,

$$H_0 = -t\sum_{\sigma,i}\sum_{j=1}^{3}(a^{\dagger}_{\sigma,\mathbf{R_i}}b_{\sigma,\mathbf{R_i}+\mathbf{a_j}} + H.C.), \tag{7.1}$$

where $t \approx 2.8$ eV is the hopping energy between nearest neighbour carbon atoms and $\mathbf{a}_j$ are nearest neighbour vectors (red arrows on Fig. 7.1),

$$\begin{aligned}\mathbf{a}_1 &= a(0,1)\\ \mathbf{a}_2 &= \frac{a}{2}(\sqrt{3},-1)\\ \mathbf{a}_3 &= \frac{a}{2}(-\sqrt{3},-1)\end{aligned}$$

with $a \approx 0.14nm$ is the distance between nearest neighbour lattice sites. After applying Fourier transformation to the creation and annihilation operators

$$a_{\sigma,\mathbf{R_i}=\frac{1}{\sqrt{N}}}\sum_{\mathbf{k}} e^{i\mathbf{R_i}\cdot\mathbf{k}}a_{\sigma,k} \tag{7.2}$$

one can rewrite the Hamiltonian in the momentum space

$$\begin{aligned}H_0 &= -t\sum_{\mathbf{k}}(\phi_{\mathbf{k}}a^{\dagger}_{\sigma,\mathbf{k}}b_{\sigma,\mathbf{k}} + H.C.)\\ &= \sum_{\sigma,\mathbf{k}}\Psi^{\dagger}_{\sigma,\mathbf{k}}\begin{pmatrix}0 & -t\phi_{\mathbf{k}}\\ -t\phi^{*}_{\mathbf{k}} & 0\end{pmatrix}\Psi_{\sigma,\mathbf{k}},\end{aligned} \tag{7.3}$$

where $\Psi_{\sigma,\mathbf{k}} = (a_{\sigma,\mathbf{k}}, b_{\sigma,\mathbf{k}})$ and

$$\phi_{\mathbf{k}} = \sum_{i=1}^{3} e^{i\mathbf{a_i}\cdot\mathbf{k}}. \tag{7.4}$$

Diagonalizing the Hamiltonian H_0 yields the spectrum for graphene [10]

$$E(\mathbf{k}) = \pm t|\phi_{\mathbf{k}}|. \tag{7.5}$$

The plus and minus correspond to conductance (π^*) and valence (π) bands, respectively.

The Brillouin zone of graphene is presented in Fig. 7.2 showing high symmetry points Γ, M, K and K'. In the graphene the valence and conductance bands touch each other at, so called, Dirac points $K = (4\pi/(3\sqrt{3}a), 0)$ and $K' = -K$ resulting in the gapless spectrum. This situation is in contrast with the standard case in the condensed matter physics when a system is characterized by Fermi surface instead of Fermi points. At Dirac points the density of states vanishes linearly [12] and

$$E(\mathbf{K}) = \pm t|\phi_{\mathbf{K}}| = e^{iK_y a} + 2e^{-iaK_y/2}\cos\left(\frac{\sqrt{3}}{2}aK_x\right) = 0. \tag{7.6}$$

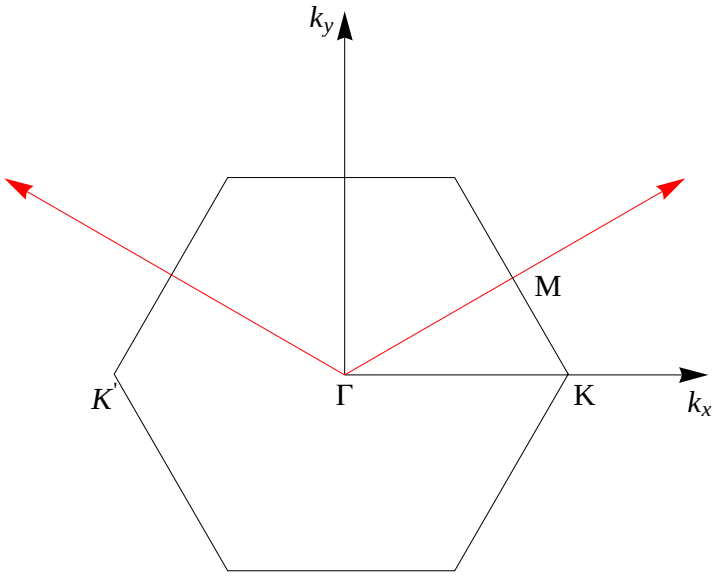

Figure 7.2: Hexagonal Brillouin zone of graphene. Red arrows show reciprocal lattice vectors. K and K' points represent two set of nonequivalent points which cannot be connected by the reciprocal lattice vectors.

Expanding $\phi_{\mathbf{k}}$ around K point yields

$$\begin{aligned}\phi_{\mathbf{k}} &= 1 + iak_y + 2(1 - ia\frac{p_y}{2})(-\frac{1}{2} - \frac{3}{4}k_x a) \\ &= -\frac{3}{2}a(k_x - ik_y)\end{aligned} \tag{7.7}$$

which results in the linearized energy spectrum

$$E(\mathbf{k}) = \pm v|\mathbf{k}| \tag{7.8}$$

where $v = (3/2)at \approx 10^6 m/s$ is the Fermi velocity. The form of Eq. 7.8 mimics the spectrum for massless Dirac Fermions [14].

The tight-binding Hamiltonian for the bilayer graphene which accounts for the interlayer nearest neighbour hopping and interlayer hopping between the atoms sitting on top of each other has the following form

$$H_0 = \sum_{\sigma,\mathbf{k}} \Psi^{\dagger}_{\sigma,\mathbf{k}} \begin{pmatrix} 0 & -t\phi_{\mathbf{k}} & -t_\perp & 0 \\ -t\phi^*_{\mathbf{k}} & 0 & 0 & 0 \\ -t_\perp & 0 & 0 & -t\phi^*_{\mathbf{k}} \\ 0 & 0 & -t\phi_{\mathbf{k}} & 0 \end{pmatrix} \Psi_{\sigma,\mathbf{k}}, \tag{7.9}$$

where $t_\perp \approx 0.39$ eV is the interlayer hopping parameter, $\phi_{\mathbf{k}}$ is given by Eq. 7.4 and $\Psi_{\sigma,\mathbf{k}} = (a_{\sigma,\mathbf{k}}, b_{\sigma,\mathbf{k}}, \overline{b}_{\sigma,\mathbf{k}}, \overline{a}_{\sigma,\mathbf{k}})$ (overbar refers to, let's say, upper layer). H_0 gives four non-degenerate bands

$$E(\mathbf{k}) = \pm\frac{1}{2}\left(t_\perp \pm \sqrt{t_\perp^2 + 4t^2|\phi_{\mathbf{k}}|^2}\right). \tag{7.10}$$

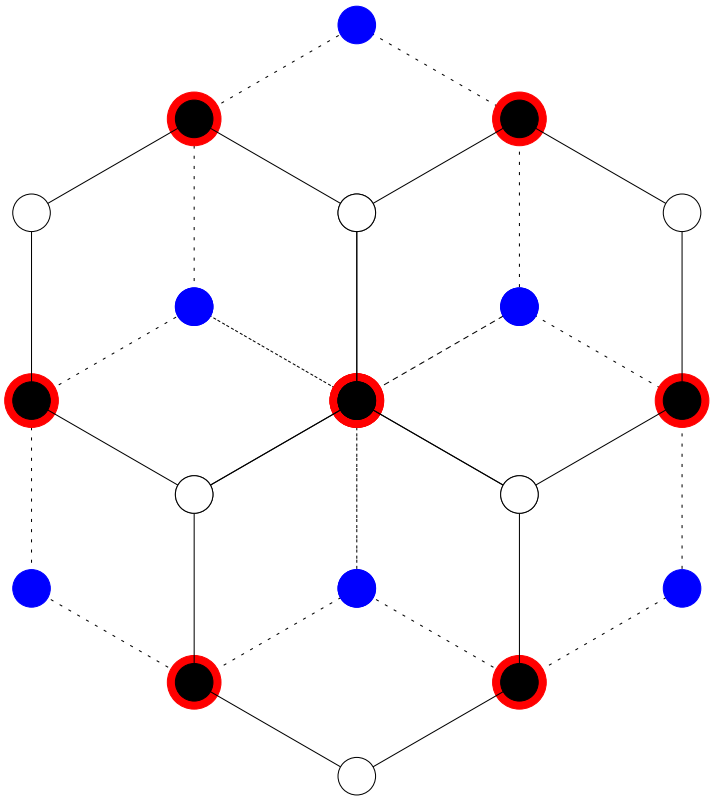

Figure 7.3: Bilayer graphene lattice structure. White (sublattice A) and black (sublattice B) dots belong to the upper plane whereas blue (sublattice B) and red (sublattice A) ones belong to the lower plane.

In order to study the low energy properties of the bilayer graphene we make, as in the case of monolayer graphene, an expansion around K point and using Eq. 7.7 one can obtain

$$E(\mathbf{k}) = \pm\frac{t_\perp}{2}\left(1 \pm \sqrt{1+4\left(\frac{v|\mathbf{k}|}{t_\perp}\right)^2}\right). \tag{7.11}$$

These bands are sketched in Fig. 7.4. This shows that a similar situation holds in this case as in the single layer graphene, the fermi surface is represented by two Fermi points at K and K', however spectrum being parabolic at these locations.

Next approximation one can make is to assume that $v|\mathbf{k}| \ll t_\perp$. Since two outer bands in Fig. 7.4 do not affect the low energy physics and are therefore irrelevant this approximations is called two-band limit. To write the Hamiltonian

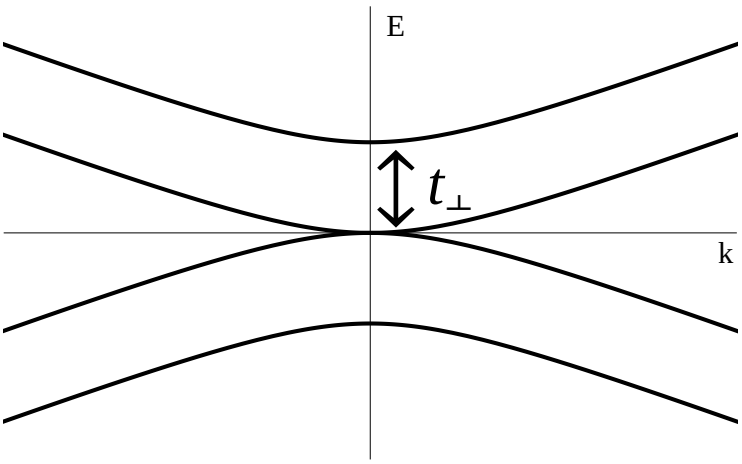

Figure 7.4: Four bands of the bilayer graphene expanded around the Brillouin zone corner.

Eq. 7.9 in this limit we decompose it as $H_0 = H_0^{(1)} + H_0^{(2)}$, where

$$H_0^{(1)} = \begin{pmatrix} 0 & 0 & -t_\perp & 0 \\ 0 & 0 & 0 & 0 \\ -t_\perp & 0 & 0 & 0 \\ 0 & 0 & 0 & 0 \end{pmatrix} \tag{7.12}$$

and

$$H_0^{(2)} = \begin{pmatrix} 0 & -t\phi_{\mathbf{k}} & 0 & 0 \\ -t\phi_{\mathbf{k}}^* & 0 & 0 & 0 \\ 0 & 0 & 0 & -t\phi_{\mathbf{k}}^* \\ 0 & 0 & -t\phi_{\mathbf{k}} & 0 \end{pmatrix} \tag{7.13}$$

with $\phi_{\mathbf{k}} = -(3/2)(k_x - ik_y)a$, and then use the perturbation theory for degenerate case [29] up to second order. The result is the effective Hamiltonian $H_{eff} = -P_0 H_0^{(2)} P_1 (1/H_0^{(1)}) P_1 H_0^{(2)} P_0$ where

$$P_0 = \begin{pmatrix} 0 & 0 & 0 & 0 \\ 0 & 1 & 0 & 0 \\ 0 & 0 & 0 & 0 \\ 0 & 0 & 0 & 1 \end{pmatrix} \tag{7.14}$$

and

$$P_1 = 1 - P_0 \tag{7.15}$$

$$= \begin{pmatrix} 1 & 0 & 0 & 0 \\ 0 & 0 & 0 & 0 \\ 0 & 0 & 1 & 0 \\ 0 & 0 & 0 & 0 \end{pmatrix} \tag{7.16}$$

are projection operators onto the degenerate and non degenerate subspaces, respectively. It is crucial to mention that the matrix elements of H_{eff} must be

computed in the non degenerate subspace resulting in

$$H_{eff} = \frac{v^2}{t_\perp} \begin{pmatrix} 0 & 0 & 0 & 0 \\ 0 & 0 & 0 & (k_x - ik_y)^2 \\ 0 & 0 & 0 & 0 \\ 0 & (k_x + ik_y)^2 & 0 & 0 \end{pmatrix}. \tag{7.17}$$

After multiplying H_{eff} by $\Psi_{\sigma,\mathbf{k}}$ from the left and right it becomes clear that H_{eff} actually is a 2×2 matrix in the $\Psi_{\sigma,\mathbf{k}} = (b_{\sigma,\mathbf{k}}, \overline{a}_{\sigma,\mathbf{k}})$ basis,

$$H_{eff} = \frac{1}{2m} \begin{pmatrix} 0 & (k_x - ik_y)^2 \\ (k_x + ik_y)^2 & 0 \end{pmatrix}. \tag{7.18}$$

with $m = t_\perp/(2v^2) \approx 0.0054 m_e$ being the effective mass of the electron. Using the values of $t_\perp$ and v one can show that $m \approx (0.03 - 0.05)m_e$ [9]. At very low densities, which are not considered in this thesis, the term linear in k (associated with trigonal warping) should be added to H_{eff} [30]. H_{eff} gives parabolic spectrum

$$E(\mathbf{k}) = \pm \frac{k^2}{2m} \tag{7.19}$$

whereas in the opposite limit $v|\mathbf{k}| \gg t_\perp$ it would give a linear energy spectrum as it is for the monolayer graphene. The crossover between these two regimes of the energy spectrum is controlled by the carrier density (chemical potential) and if it is smaller than $5 \times 10^{12} cm^{-2}$ (experimentally realized densities range from approximately $10^{11} cm^{-2}$ to $10^{13} cm^{-2}$) parabolic dispersion is valid otherwise the spectrum is linear [9].

The hopping between two Dirac points, K and K', is very weak and it can be ignored which means that it is sufficient to consider only one of the valleys and the second one can be taken into account by introducing a degeneracy factor of 2. There exists another degeneracy due to the spin and thus the overall degeneracy factor g would be 4.

H_{eff} describes system with chiral particles (as in the monolayer graphene) which is due to the presence of two equivalent but independent A and B sublattices [31].

So far, I have discussed only kinetic energy of the bilayer graphene Hamiltonian. The term in the full Hamiltonian which accounts for the interactions is, in its most general form, given by

$$\begin{aligned} H_I = & \frac{1}{2} \int d^2\mathbf{r} d^2\mathbf{r}' [V(\mathbf{r} - \mathbf{r}')(\rho_1(\mathbf{r})\rho_1(\mathbf{r}') + \rho_2(\mathbf{r})\rho_2(\mathbf{r}')) + \\ & + \overline{V}(\mathbf{r} - \mathbf{r}')(\rho_1(\mathbf{r})\rho_2(\mathbf{r}') + \rho_2(\mathbf{r})\rho_1(\mathbf{r}'))] \end{aligned} \tag{7.20}$$

where $\rho_i(\mathbf{r})$ is a density operator in sublattice i, $V(\mathbf{r}-\mathbf{r}')$ is a intralayer Coulomb interaction between electrons residing on the same sublattice and $\overline{V}(\mathbf{r} - \mathbf{r}')$ describes interlayer interaction between electrons on the different sublattices. Fourier transformation of H_I yields

$$H_I = \frac{1}{2} \sum_{\mathbf{q} \neq 0} [V_\mathbf{q}(\rho_1(\mathbf{q})\rho_1(-\mathbf{q}) + \rho_2(\mathbf{q})\rho_2(-\mathbf{q})) + \overline{V}_\mathbf{q}(\rho_1(\mathbf{q})\rho_2(-\mathbf{q}) + \rho_2(\mathbf{q})\rho_1(-\mathbf{q}))] \tag{7.21}$$

where

$$\rho(\mathbf{q}) = \int d^2\mathbf{r} e^{-i\mathbf{rq}} c^\dagger_{\mathbf{r}} c_{\mathbf{r}} = \sum_{\mathbf{k}} c^\dagger_{\mathbf{k}+\mathbf{q}} c_{\mathbf{k}}, \tag{7.22}$$

$V_{\mathbf{q}} = 2\pi e^2/\kappa q$ and $\overline{V}_{\mathbf{q}} = V_{\mathbf{q}} e^{-qd}$, $d \approx 2.4a \approx 0.335\,nm$ being the interlayer distance. There is no $q = 0$ term in the latter equation because its contribution in case of long-range Coulomb interaction is cancelled by positive background charge [32]. H_I can be rewritten in terms of the symmetric and antisymmetric combinations of density operators:

$$\begin{aligned} H_I = & \frac{1}{2} \sum_{\mathbf{q}\neq 0} \Bigg(\frac{V_{\mathbf{q}} + \overline{V}_{\mathbf{q}}}{2} (\rho_1(\mathbf{q}) + \rho_2(\mathbf{q}))(\rho_1(-\mathbf{q}) + \rho_2(-\mathbf{q})) + \\ & + \frac{V_{\mathbf{q}} - \overline{V}_{\mathbf{q}}}{2} (\rho_1(\mathbf{q}) - \rho_2(\mathbf{q}))(\rho_1(-\mathbf{q}) - \rho_2(-\mathbf{q})) \Bigg). \end{aligned} \tag{7.23}$$

It is customary to approximate $\overline{V}_{\mathbf{q}}$ to be $V_{\mathbf{q}}$ because the exponent e^{-qd} in $\overline{V}_{\mathbf{q}}$ is close to unity. Finally, the interacting part of the Hamiltonian has the following form

$$H_I = \frac{1}{2} \sum_{\mathbf{q}\neq 0} V_{\mathbf{q}} (\rho_1(\mathbf{q}) + \rho_2(\mathbf{q}))(\rho_1(-\mathbf{q}) + \rho_2(-\mathbf{q})). \tag{7.24}$$

Since our calculation is done in the units of k_F and ϵ_F we will write the Coulomb potential $V_{\mathbf{q}}$ in those units. We note that because of the Fourier transform the dimension of $V_{\mathbf{q}}$ is $[\epsilon]/[k^2]$. To factor out the dimensionless part from $V_{\mathbf{q}}$ it is multiplied and divided by ϵ_F/k_F^2:

$$V_{\mathbf{q}} = \frac{2\pi e^2}{\kappa q} \frac{k_F^2}{\epsilon_F} \frac{\epsilon_F}{k_F^2}. \tag{7.25}$$

The interaction in the units of ϵ_F and k_F is then given by

$$\begin{aligned} V_q &= \frac{2\pi e^2}{\kappa q} \frac{k_F^2}{\epsilon_F} \\ &= \frac{2\pi e^2}{\kappa q k_F} 2m \\ &= \frac{4\pi}{gq} \frac{g e^2 m}{\kappa k_F} \\ &= \frac{4\pi}{gq} r_s \end{aligned} \tag{7.26}$$

where r_s is a dimensionless coupling parameter and g is the degeneracy factor. In 7.26, q is replaced with $q \times k_F$ which means that q is dimensionless in the final expression.

The dimensionless coupling r_s is defined as the ratio of the average Coulomb potential $\langle V \rangle = e^2/\kappa r_0$ and Fermi energy where r_0 is an average inter particle distance defined through

$$\frac{1}{n} = \pi r_0^2 \tag{7.27}$$

with n being a carrier density. The Fermi energy ϵ_F at $T = 0$ can expressed as a function of n using the relation

$$n = g \int_0^{k_F} \frac{dkd\theta k}{(2\pi)^2} = \frac{gm\epsilon_F}{2\pi}. \tag{7.28}$$

Since we have the expressions for ϵ_F and r_0 we derive the expression for r_s:

$$\begin{aligned} r_s &= \sqrt{g}\frac{\langle V \rangle}{\epsilon_F} \\ &= \frac{g^{3/2}me^2}{2\kappa}\frac{1}{\sqrt{\pi n}} \\ &= \frac{e^2 mg}{\kappa k_F}. \end{aligned} \tag{7.29}$$

7.2 GW and RPA

In order to describe the properties of this system we have to employ appropriate approximation. One of the earliest approximations based on the Greens function method is Hartree-Fock approximation which implies that self-energy of a given system is computed using only first order (direct and exchange) Feynman diagrams. The direct diagram (Fig. 7.5 a)) is local i.e. does not describe the propagation of the electron while the exchange diagram (Fig. 7.5 b)) is nonlocal and reflects the Pauli exclusion principle. The Hartree-Fock approximations completely ignores the correlations between electrons and thus is not a reasonable approximation when these correlations are important.

The Coulomb potential repels electrons from each other which gives rise to the formation of holes around each electron whose effective positive charge screens reduces the interaction magnitude. This screening is not taken into account in the Hartree-Fock approximation.

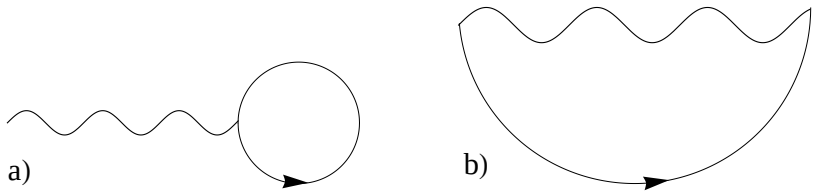

Figure 7.5: a) Hartree (direct) diagram, b) Fock (exchange) diagram. Solid lines represent Greens function and wavy one - interaction.

Density functional theory (DFT) together with local density approximation (LDA) is a standard method to describe the ground state properties of a given system which takes into account correlations [33, 34, 35]. DFT+LDA together with methods beyond LDA were successfully applied to various models but in some cases they reveal discrepancies (wrong estimates for bandwidth, bandgaps, quasiparticle energies, etc.).

Quasiparticle energies, single-particle spectral functions and total energies are properly computed within the thermal Greens function technique, where all correlations are, in principle, included in a self-energy Σ. However, it is very

difficult to compute Σ and usually it is calculated in different approximations. The approximation to compute self-energy which is used in this thesis is called the GW approximation [36, 37, 38]. It is the method beyond the Hartree-Fock approximation that takes screening into account. The GW approximation was derived perturbatively by Hedin from the so called Hedin's equations (see Appendix E). Hedin showed how the self-energy should be expanded in a fully screened potential W where the first terms represents the GW approximation.

The GW approximation can be implemented in a fully and partially self-consistent way. In the former case Greens function G and screened interaction W are both updated after each iteration while in the latter case only G (W) is updated whereas W (G) is fixed. There is a specific and simplest case of the GW approximation when we do only one iteration, no self-consistency, which in the literature is known as random phase approximation (RPA). Therefore in RPA polarization, building block of the diagrams involved in GW approximation, is approximated by the product of two bare Greens functions which is the zeroth order term in the expansion of $\Pi_{\vec{q}}(i\omega_n)$ in the bare interaction. Consequently, the RPA self-energy and dressed interaction consists of exactly same diagrams as those in GW approximation (see Fig. E.6 and E.4 in Appendix E) but the dressed Greens functions are replaced by the non-interacting ones.

Although the GW approximation has been successfully applied to wide range of models it has been observed, in contrast to the non self-consistent GW, that the fully self-consistent GW approximation is not able to capture a number of satellite features because of the lack of the vertex corrections in GW self-energy [39, 40, 41]. There are methods (quasi-particle self-consistent GW, GW+DMFT) based on the standard GW and it has been shown that including the vertex corrections even within those methods is crucial to get reasonable results [41]. It also has been shown that performing GW calculation self-consistently yields improved values for the total energy than RPA [40]. We think that our results obtained in the fully self-consistent GW approximation can be used as a benchmark for those obtained using more sophisticated methods. In addition, calculations showed the feasibility of the periodized Greens function method by implementing it in the heavy numerical calculation such as the fully self-consistent GW approximation.

7.3 Plasma, Plasmons and Plasmarons

A plasma is a matter constituting of equal concentration of negatively and positively charged particles and at least the particles belonging to one of those categories are mobile. Usually, the negative charge of the conductance electrons is compensated by positively charged ions.

Suppose there is a plasma in a thin metallic slab or film and the entire electron gas, as a whole, is displaced with respect to the background positive charge of ions resulting in the formation of a surface charge on the upper and lower surfaces of the slab. This produces an electric field inside the slab which acts as a restoring force on the electron gas, trying to bring it back to equilibrium state and thus leads to the plasma oscillation. This is a simple model explaining charge density waves in plasma. Plasma oscillation is considered as a collective excitation of the electron gas. The quantum of this excitation is called plasmon. Experimentally, plasmons can be excited by impacting a beam

of electrons on the thin metallic film. The reflected or transmitted electrons show energy loss due to inelastic collisions equal to multiples of the plasmon energy. This experiment is called electron energy loss spectroscopy (EELS).

In order to see how plasmons emerge as the charge density oscillations let us introduce the density-density correlation function at zero temperature [23, 42]

$$\chi(x,t;x',t') = -i\langle Tc^\dagger(x,t)c(x,t)c^\dagger(x',t')c(x',t')\rangle. \tag{7.30}$$

The equation for $\chi(x,t;x',t')$ is analogous to Eq. E.3 with Π and Γ^* replaced by $\chi(x,t;x',t')$ and full vertex Γ. In RPA particle-hole vertex Γ_{ph} is equal to V_q thus $\Gamma = W_q$, Eq. E.7, and consequently density-density response function is given by

$$\chi(q,\omega) = \sum_{k_1,\omega_1} G_0(k_1+q,\omega_1+\omega)G_0(k_1,\omega)\,(1+ \\ +\frac{V_q}{1-V_q\Pi_q(\omega)}\sum_{k_2,\omega_2} G_0(k_2+q,\omega_2+\omega)G_0(k_2,\omega)\Bigg). \tag{7.31}$$

The poles of the density-density response function give excitations in the system which represents collective charge density oscillations in the electron gas (plasmon). Plasmon has its own dispersion relation defined by the pole of the Greens function:

$$1 = V_q\Pi_q(\omega) \tag{7.32}$$

As these excitations occur for small momenta [42, 43, 44] to simplify derivation of the plasmon dispersion relation let us take the limit $q \to 0$ in the polarization $\Pi_q(\omega)$. For simplicity let us consider the polarization for a two dimensional single-band electron system with parabolic dispersion relation which in the RPA has the following form

$$\Pi_q(\omega) = g\int \frac{d^2k}{(2\pi)^2}\frac{n_F(\epsilon_{\mathbf{k}}) - n_F(\epsilon_{\mathbf{k+q}})}{\omega+\epsilon_{\mathbf{k}}-\epsilon_{\mathbf{k+q}}} \tag{7.33}$$

where $n_F(\epsilon_{\mathbf{k}}) = (e^{\beta\epsilon_{\mathbf{k}}}+1)^{-1}$ is a Fermi-Dirac distribution and $\epsilon_{\mathbf{k}} = k^2/2m$. Changing the integration variable in the second integral to $\mathbf{k}' = \mathbf{k}+\mathbf{q}$ enables us to rewrite $\Pi_q(\omega)$ in the following form

$$\Pi_q(\omega) = g\int \frac{d^2k}{(2\pi)^2} n_F(\epsilon_{\mathbf{k}})\left(\frac{1}{\omega+\epsilon_{\mathbf{k}}-\epsilon_{\mathbf{k+q}}} - \frac{1}{\omega-\epsilon_{\mathbf{k}}+\epsilon_{\mathbf{k-q}}}\right). \tag{7.34}$$

Taking the limit $q \to 0$ yields

$$\Pi(q\to 0,\omega) = g\int \frac{d^2k}{(2\pi)^2} n_F(\epsilon_{\mathbf{k}})\left[\left(\frac{1}{\omega}+\frac{kq\cos(\theta)}{m\omega^2}+\frac{q^2}{2m\omega^2}+\frac{(kq\cos(\theta))^2}{m^2\omega^3}\right) - \right. \\ \left. -\left(\frac{1}{\omega}+\frac{kq\cos(\theta)}{m\omega^2}-\frac{q^2}{2m\omega^2}+\frac{(kq\cos(\theta))^2}{m^2\omega^3}\right)\right] \\ = g\int \frac{d^2k}{(2\pi)^2} n_F(\epsilon_{\mathbf{k}})\frac{q^2}{m\omega^2} \\ = \frac{n}{m}\frac{q^2}{\omega^2}. \tag{7.35}$$

Inserting $\Pi(q \to 0, \omega)$ in Eq. 7.32 gives the plasmon dispersion relation

$$\omega_p = \sqrt{\frac{2\pi e^2 n}{\kappa m}} q^{1/2}. \tag{7.36}$$

Lundqvist investigated the effects of plasmon pole on the self-energy in the case of three-dimensional electron gas [45]. Analogous study was carried out by Paul von Allmen for two-dimensional electron gas [46]. In both cases imaginary part of the self-energy is characterized by the strong resonances below (above) the Fermi energy when momentum k smaller (greater) than a critical value k_0. Due to the Kramers-Kronig relation the resonances in the imaginary part of the self-energy is reflected by the strong oscillations in the real part of the self-energy which means that apart from the main quasiparticle peak spectral function has additional peak. To find the location of that peak the solution to

$$\omega - \epsilon_k - Re[\Sigma_k(\omega)] = 0 \tag{7.37}$$

should be found. Intersections of $\omega - \epsilon_k$ and $Re[\Sigma_k(\omega)]$ represent the solutions to Eq. 7.37 and they can be identified with the corresponding peaks in the spectral function. Using this method it was shown that the oscillations in the real part of the self-energy results in the additional peak in the spectral weight which at small k values sharpens with decreasing momentum and becomes a delta function if the corresponding damping is zero ($Im[\Sigma] = 0$). This peak and correspondingly a new quasiparticle was identified by Lundqvist. He called it a plasmaron which can be interpreted as a composite quasiparticle consisting of hole (electron if $\epsilon > 0$) and plasmon or as a hole (electron) altered by the cloud of hole-plasmon pairs. With increasing momentum the plasmaron peak broadens, becomes invisible around $k = k_f$ but at $k \gtrsim k_F$ it appears again. The difference between 3D and 2D plasmarons is that 3d plasmaron vanishes around $k = k_F$ while 2D plasmaron merges with the main quasiparticle peak.

In the following section we will see how plasmaron is revealed in graphene through the single particle spectral function.

7.4 Electronic Structure of Bilayer Graphene

The electronic structure of bilayer graphene [47, 19] is characterised by the single particle spectral function $A_{\vec{k}}(\omega)$, which can be measured experimentally by angle resolved photo-emission spectroscopy (ARPES)[48, 49]. Sensarma *et al.* [22] studied how Coulomb interaction affects the single particle spectral function of bilayer graphene away from half-filling. The authors used RPA to calculate that doped bilayer graphene is a Fermi liquid in the low energy limit, with a sharp quasiparticle peak. They also found additional weaker peak structures that they interpreted as plasmarons.

Studying the physics of interaction between electrons and plasmons in graphene is particularly interesting because of recently proposed "plasmonic" devices that could merge photonics and electronics [49].

Experimentally plasmarons in the single layer graphene were observed by A. Bostwick *et al* [49] using angle-resolved photoemission spectroscopy. Apart from the two single particle crossing bands, two additional bands were observed and interpreted as a spectrum of plasmarons. The experimentally measured spectral function compares qualitatively with that obtained within RPA.

We compute numerically the single-particle spectral function $A_{\vec{k}}(\omega)$ for doped bilayer graphene in the low energy two-band approximation in both RPA and the fully self-consistent GW approximation [36, 37, 38] using the periodized thermal Greens function formalism described in Chapter 4 and [50].

Before presenting the results I will generalize the GW equations and periodized Greens function formalism to the two-band case.

The non-interacting Greens function corresponding to Eq. 7.18 is

$$\hat{G}^0_{\vec{k}}(i\omega_n) = (i\omega_n - H_{eff} + \mu)^{-1} = \frac{1}{2}\sum_{s=\pm}\frac{\mathbb{1} + s\hat{\sigma}_{\vec{k}}}{i\omega_n - s|\epsilon_k| + \mu}, \tag{7.38}$$

s indexes the conductance and valence bands, μ is the chemical potential, $\sigma_{\vec{k}}$ is given by

$$\hat{\sigma}_{\vec{k}} = \sum_{j=\pm}\frac{k_j^2}{k^2}\hat{\sigma}_j = \sum_{j=\pm} e^{j2i\theta_{\vec{k}}}\hat{\sigma}_j = \begin{pmatrix} 0 & e^{2i\theta_{\vec{k}}} \\ e^{-2i\theta_{\vec{k}}} & 0 \end{pmatrix}, \tag{7.39}$$

where $k_\pm = k_x \pm ik_y$, $\hat{\sigma}_\pm = (\hat{\sigma}_1 \pm i\hat{\sigma}_2)/2$, $\hat{\sigma}_1$ and $\hat{\sigma}_2$ are Pauli matrices, $\theta_{\vec{k}}$ is the angle of the vector $\vec{k}$ with respect to the x-axis and ϵ_k represents parabolic dispersion relation, Eq. 7.19.

To generalize Eq. E.16 for two-band model one should take into account that the Greens function $\hat{G}_{\vec{k}}(i\omega_n)$ and vertex has additional sublattice index. Thus the bubble diagram (second diagram on the second line in Fig. E.4) yields

$$\begin{aligned} &-\frac{g}{\beta}V_q^2\sum_{m=-\infty}^{\infty}\sum_{s'',s'''}\int\frac{d^2k}{(2\pi)^2}G^{s''s'''}_{\vec{k}+\vec{q}}G^{s'''s''}_{\vec{k}} = \\ &-\frac{g}{\beta}V_q^2\sum_{m=-\infty}^{\infty}\int\frac{d^2k}{(2\pi)^2}Tr(\hat{G}_{\vec{k}}(i\omega_m)\hat{G}_{\vec{k}+\vec{q}}(i\omega_n + i\omega_m)) \equiv V_q^2\Pi_{\vec{q}}(i\omega_n). \end{aligned} \tag{7.40}$$

Here we used the fact that due to the approximation $V_q = \overline{V}_q$ the vertex does not depend on the sublattice index. Based on the rotational symmetry of bands in the low energy limit once can conclude that polarization $\Pi_{\vec{q}}(i\omega_n)$ is an angle independent function. This can also be shown by assuming that the Greens functions in Eq. 7.40 are the non-interacting ones then rotating the integration variable $\vec{k}$ with an angle $\theta_{\vec{q}}$ yielding

$$\begin{aligned} e^{2i\theta_{\vec{k}}} &= e^{2i\theta_{\vec{k}'}}e^{2i\theta_{\vec{q}}} \\ e^{2i\theta_{\vec{k}+\vec{q}}} &= e^{2i\theta_{\vec{k}'+\vec{q}'}}e^{2i\theta_{\vec{q}}} \end{aligned}$$

where $\vec{k}'$ and $\vec{q}'$ are $\vec{k}$ and $\vec{q}$ in the new basis and finally performing trace. As a result the screened interaction is an angle independent and, in addition, it remain a scalar function as it is in the single-band case due to the trace in Eq. 7.40.

The GW self-energy for the two-band case is generalized to

$$\hat{\Sigma}^{GW}_{\vec{k}}(i\omega_n) = \frac{1}{\beta}\sum_{\vec{q}}\sum_{m=-\infty}^{\infty}W_q(i\omega_m)\hat{G}_{\vec{k}-\vec{q}}(i\omega_n - i\omega_m). \tag{7.41}$$

Since we are dealing with the self-consistent calculation it is important to investigate the matrix structure of $\hat{\Sigma}^{GW}_{\vec{k}}(i\omega_n)$. To do that let us first replace

$\hat{G}_{\vec{k}-\vec{q}}(i\omega_n - i\omega_m)$ by its noninteracting version then shift and rotate the integration variable in Eq. 7.41 in the following manner

$$\vec{q}_1 = \vec{k} - \vec{q} \tag{7.42}$$

$$\vec{q}_2 = \mathcal{R}(\pi + \theta_{\vec{k}})\vec{q}_1, \tag{7.43}$$

where $\mathcal{R}(\pi + \theta_{\vec{k}})$ denotes the rotation matrix with the angle $\pi + \theta_{\vec{k}}$. Therefore the self-energy can be rewritten as

$$\hat{\Sigma}^{GW}_{\vec{k}}(i\omega_n) = \frac{1}{2}\begin{pmatrix} \Sigma_0 & \Sigma_+ e^{i2\theta_{\vec{k}}} \\ \Sigma_- e^{-i2\theta_{\vec{k}}} & \Sigma_0 \end{pmatrix}, \tag{7.44}$$

with

$$\Sigma_0 = \int \frac{d^2q}{(2\pi)^2} a^+_{q_2} W(|\vec{k} - \vec{q_2}|), \tag{7.45}$$

$$\Sigma_\pm = \int \frac{d^2q}{(2\pi)^2} a^-_{q_2} W(|\vec{k} - \vec{q_2}|) e^{\pm i2\theta_{\vec{q}_2}} \tag{7.46}$$

and

$$a^\pm_k \equiv (i\omega_n - |\epsilon_k| + \mu)^{-1} \pm (i\omega_n + |\epsilon_k| + \mu)^{-1}. \tag{7.47}$$

It is obvious that $\Sigma_+ = \Sigma_-$ after changing $\theta_{\vec{q}_2}$ with $-\theta_{\vec{q}_2}$ in Σ_+ or Σ_-. Hence the self-energy $\hat{\Sigma}^{GW}_{\vec{k}}(i\omega_n)$ and consequently the dressed Greens function $\hat{G}_{\vec{k}}(i\omega_n)$ have and keep the same structure as that of the free Greens function

$$\hat{G}^0_{\vec{k}}(i\omega_n) = \frac{1}{2}\begin{pmatrix} a^+_k & a^-_k e^{i2\theta_{\vec{k}}} \\ a^-_k e^{-i2\theta_{\vec{k}}} & a^+_k \end{pmatrix} \tag{7.48}$$

throughout the self-consistent procedure which makes it sufficient to set up the calculation only at $\theta_{\vec{k}} = 0$.

7.4.1 Periodized Greens Function Formalism for Two-Band models

Since bilayer graphene is described by two-band Hamiltonian I will generalize the periodized Greens function method presented in Chapter 4 to use it for performing the self-consistent GW calculation.

Based on Eq. 7.38 one can easily write the bare periodized Greens function

$$\hat{G}^0_{\vec{k}}(i\omega_n) = \frac{1}{2}\sum_{s=\pm} \eta \coth \eta (i\omega_n - s|\epsilon_k| + \mu)(\mathbb{1} + s\hat{\sigma}_{\vec{k}}) \tag{7.49}$$

whereas by analogy the periodized Dyson equation is generalized to

$$\hat{G}_{\vec{k}}(i\omega_n) = \eta \coth \eta ((\hat{G}^0_{\vec{k}}(i\omega_n))^{-1} - \hat{\Sigma}_{\vec{k}}(i\omega_n)), \tag{7.50}$$

where

$$\begin{aligned}(\hat{G}^0_{\vec{k}}(i\omega_n))^{-1} &= \begin{pmatrix} i\omega_n + \mu & -|\epsilon_k| e^{i2\theta_{\vec{k}}} \\ -|\epsilon_k| e^{-i2\theta_{\vec{k}}} & i\omega_n + \mu \end{pmatrix} \\ &= (i\omega_n + \mu)\mathbb{1} - |\epsilon_k|\hat{\sigma}_{\vec{k}}.\end{aligned}$$

The periodized Greens function is consistent with the corresponding Luttinger-Ward variational principle [25, 26]:

$$0 = \frac{\partial \Gamma}{\partial G} = \frac{\Phi}{G} - \frac{\partial \Sigma}{\partial G}\hat{G}^{-} - \hat{\Sigma} + (\hat{G}^{-})^{-1}$$

$$= -\frac{\partial \Sigma}{\partial G}\hat{G}^{-} + (\hat{G}^{-})^{-1}$$

$$\frac{\partial \Sigma}{\partial G} = (\hat{G}^{+}\hat{G}^{-})^{-1}$$

$$= (\hat{G}^{+}\hat{G}^{-})^{-1}(\hat{G}^{+} - \hat{G}^{-})(\hat{G}^{+} - \hat{G}^{-})^{-1}$$

$$= 2\eta((\hat{G}^{-})^{-1} - (\hat{G}^{+})^{-1}).$$

Γ-functional is given by Eq. 5.16. Solving the differential equation with the initial condition $\hat{\Sigma} = 0$ at $\hat{G} = \hat{G}_0$ yields

$$\hat{\Sigma} = 2\eta \log\left((\hat{G}^{+})^{-1}\hat{G}^{-}(\hat{G}_0^{-})^{-1}\hat{G}_0^{+}\right)$$

$$\hat{G} = \eta(\hat{G}_0 - \eta \tanh(\eta\hat{\Sigma}))(\eta - \hat{G}_0 \tanh(\eta\hat{\Sigma}))^{-1}.$$

By writing $\tanh(\eta\hat{\Sigma})$ in the form of matrix using the diagonalisation of $\hat{\Sigma}$, applying hyperbolic tangent and then transforming back to the old basis we obtain the matrix elements of $\hat{G}$:

$$G_{11} = G_{22} = \frac{\eta}{2}(\coth\eta(i\omega_n + |\epsilon_k| + \mu - 2\Sigma_2) + \coth\eta(i\omega_n - |\epsilon_k| + \mu - 2\Sigma_1))$$

$$G_{12} = \frac{\eta}{2}e^{2i\theta_{\vec{k}}}(\coth\eta(i\omega_n - |\epsilon_k| + \mu - 2\Sigma_1) - \coth\eta(i\omega_n + |\epsilon_k| + \mu - 2\Sigma_2))$$

$$G_{21} = \frac{\eta}{2}e^{-2i\theta_{\vec{k}}}(\coth\eta(i\omega_n - |\epsilon_k| + \mu - 2\Sigma_1) - \coth\eta(i\omega_n + |\epsilon_k| + \mu - 2\Sigma_2))$$

where

$$\Sigma_1 = \int \frac{d^2q}{(2\pi)^2}\frac{a_{q_2}^{+} + a_{q_2}^{-}}{2}W(|\vec{k} - \vec{q_2}|),$$

$$\Sigma_2 = \int \frac{d^2q}{(2\pi)^2}\frac{a_{q_2}^{+} - a_{q_2}^{-}}{2}W(|\vec{k} - \vec{q_2}|).$$

Then the inverse procedure of finding the matrix structure of $\tanh(\eta\hat{\Sigma})$ is performed which allows to write $\hat{G}$ in the form of Eq. 7.50. Using the same manipulations described above it can be shown that Eq. 7.49 reduces to Eq. 7.50 in the non-interacting limit.

We start the self-consistent calculation by discretising momenta and angles. Since our interest is focused on the low energy properties the absolute value of $\vec{k}$ ranging from 0 to 4 is discretised into 40 points logarithmically giving denser

number of points around k_F. The rest of the integration variables ($|\vec{q}|$, $\theta_{\vec{k}}$ and $\theta_{\vec{q}}$) are discretized linearly. $|\vec{q}|$ is discretized into 80 points and lies in the interval [1/80, 4] while the number of the discretization points for $\theta_{\vec{k}}$ and $\theta_{\vec{q}}$ is 10. First, the free Greens's function is evaluated at $\theta_{\vec{k}} = 0$ and then it is rotated by an angle $\theta_{\vec{k}}$ in order to obtain the polarization (Eq. 7.40). Then the screened interaction is computed using Eq. E.17 which enables us to evaluate the GW self-energy (Eq. 7.41). After calculating $\hat{\Sigma}^{GW}_{\vec{k}}(i\omega_n)$ at $\theta_{\vec{k}} = 0$ we update the Greens function through Eq. 7.50. This is done repeatedly: if the procedure converges to a fixed point, a solution has been found. The calculations are done at $T/\epsilon_F = 1/10$ with $N = 121$ number of Matsubara frequencies.

7.4.2 Spectral Function

The spectral function is given by

$$A_{\vec{k}}(\omega) = -\frac{1}{\pi} Im[Tr\hat{G}_{\vec{k}}(\omega + i0^+)]. \tag{7.51}$$

where we perform analytic continuation after applying trace to $\hat{G}_{\vec{k}}(i\omega_n)$. Since we are interested in the low energy properties and the Fermi energy lies in the conduction band it is convenient to focus only on the conduction band which is achieved by diagonalizing the Greens function $\hat{G}_{\vec{k}}(i\omega_n)$, picking up the eigenvalue corresponding to the conduction band and performing analytic continuation to the real frequency axis yielding the spectral function projected on the conduction band

$$A_{\vec{k}}(s = +, \omega) = -\frac{1}{\pi} Im[G_{\vec{k}}(s = +, \omega + i0^+)], \tag{7.52}$$

where

$$G_{\vec{k}}(s = +, \omega) = (U^\dagger \hat{G}_{\vec{k}}(i\omega_n) U)_{22} \tag{7.53}$$

represents the eigenvalue of $\hat{G}_{\vec{k}}(i\omega_n)$ corresponding to the upper band.

In order to derive the sum rules for both spectral functions let us first evaluate $\hat{G}^{i,j}_{\vec{k}}(\tau = 0^-) - \hat{G}^{ij}_{\vec{k}}(\tau = 0^+)$ which is equal to

$$\langle c_i^\dagger c_j \rangle + \langle c_j c_i^\dagger \rangle,$$

where i and j represent matrix indicies. If $i = j$ the last expression is equal to one whereas if $i \neq j$ it is zero. So, we have

$$\hat{G}_{\vec{k}}(\tau = 0^-) - \hat{G}_{\vec{k}}(\tau = 0^+) = \begin{pmatrix} 1 & 0 \\ 0 & 1 \end{pmatrix}. \tag{7.54}$$

Now, by carrying out the same derivation as in Eq. 6.14 and 6.15 for the diagonal entries of $\hat{G}_{\vec{k}}(\tau = 0^\pm)$ and taking into account Eq. 7.51 one can show that

$$Tr\hat{G}_{\vec{k}}(\tau = 0^-) - Tr\hat{G}_{\vec{k}}(\tau = 0^+) = \int d\omega \, A_{\vec{k}}(\omega). \tag{7.55}$$

On the other hand

$$Tr\hat{G}_{\vec{k}}(\tau = 0^-) - Tr\hat{G}_{\vec{k}}(\tau = 0^+) = 2 \tag{7.56}$$

due to the Eq. 7.54. Thus, the sum rule for the two-band spectral function has the following form,

$$\int d\omega \, A_{\vec{k}}(\omega) = 2. \tag{7.57}$$

Again, in analogy with Eq. 6.14 and 6.15 and using Eq. 7.52 we get

$$G_{\vec{k}}(s = +, \tau = 0^-) - G_{\vec{k}}(s = +, \tau = 0^+) = \int d\omega \, A_{\vec{k}}(s = +, \omega). \tag{7.58}$$

Eq. 7.53 and 7.54 yield

$$G_{\vec{k}}(s = +, \tau = 0^-) - G_{\vec{k}}(s = +, \tau = 0^+) = 1, \tag{7.59}$$

which means that the sum rule for the projected spectral function is

$$\int d\omega \, A_{\vec{k}}(s = +, \omega) = 1. \tag{7.60}$$

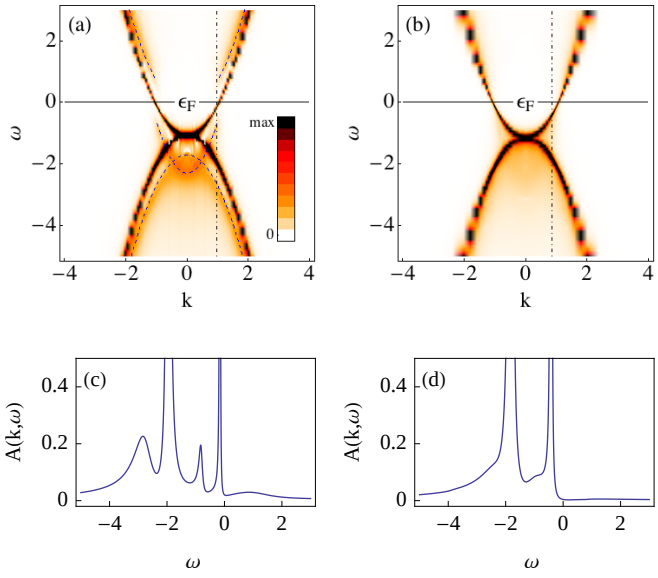

Figure 7.6: (Color online) Single particle spectral function for bilayer graphene in the low energy limit at $r_s = 3$. (a) - RPA, (b) - GW. The bare bands $\epsilon_{\vec{k}} = \pm k^2$ (in units $k_F = 1$, $\epsilon_F = 1$) are rotationally symmetric (the patchy appearance is due to the finite k-space resolution). (c) and (d) are the cuts (dash-dotted lines) in (a) and (b), respectively. Dashed lines are guides to the eye for plasmaron dispersions.

The results, presented in Fig. 7.6, 7.7, 7.8, show the spectral function with long lived Landau quasiparticles and satellite plasmaron peaks in RPA away from k_F (Fig. 7.6 (a) and left column of Fig. 7.7 and 7.8) and confirm the

results of analytic calculations [22, 51, 19]. The Fermi momentum is slightly shifted because of the interaction and the spectral functions in Fig. 7.7b and 7.8b are plotted at $k_F^* \neq k_F = 1$ (k_F - Fermi momentum in the non-interacting case) . The presence of the plasmaron excitation also give jumps in the real and imaginary parts of the corresponding self-energies. The RPA plasmaron excitation has lower weight at $r_s = 7$ than the one at $r_s = 3$, although the spectral functions have qualitatively same behaviour which is also noticeable in the case of the GW approximation where most of the structure obtained in the RPA is not present, the plasmaron peaks are replaced by broad shoulders (Fig. 7.6 (b) and left column of Fig. 7.7 and 7.8).

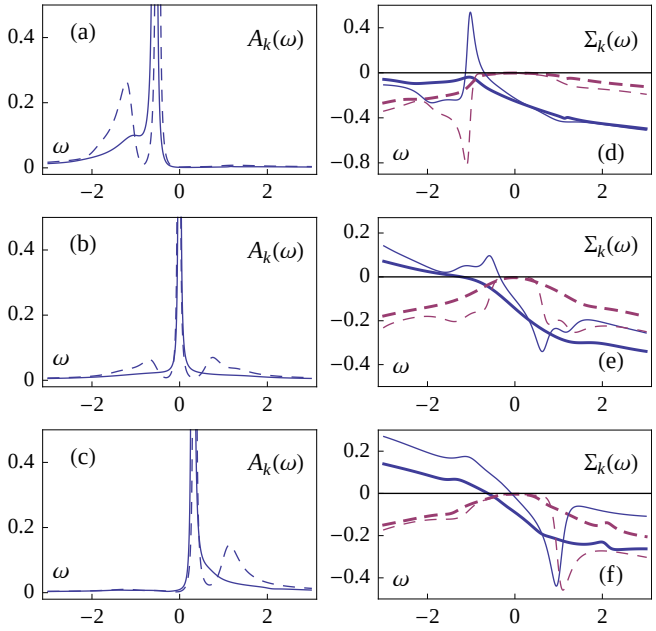

Figure 7.7: (Color online) $r_s = 3$. Left column: spectral weight in RPA (dashed line) and GW approximation (solid line) at $k \approx 0.76k_F$ (a), $k = k_F^*$ (b), $k \approx 1.20k_F$ (c). Right column: the real (blue solid line) and imaginary (red dashed line) part of the self-energy at $k \approx 0.76k_F$ (d), $k = k_F^*$ (e), $k \approx 1.20k_F$ (f) in RPA (thin line) and GW approximation (thick line).

In Fig. 7.9 (a) the electron energy loss spectrum $Im[-\epsilon_q^{-1}(\omega)]$ ($\epsilon_q(\omega) = 1 + V_q\Pi_{\vec{q}}(\omega)$ - dielectric function) in RPA is plotted showing the plasmaron dispersion relation (black color) which is in a quite good agreement for small q-values with its analytic version (solid line) expanded up to second order in q [9, 51],

$$\omega_q \simeq e\sqrt{\frac{g\epsilon_F q}{\kappa}}\left(1 - \frac{r_s q}{8k_F}\right).$$

$Im[-\epsilon_q^{-1}(\omega)]$ was also calculated in the GW approximation (Fig. 7.9 (b)) where the plasmon mode is less coherent than that in RPA which is in agreement with the fact that the plasmaron features in the GW spectral function are weaker than in RPA.

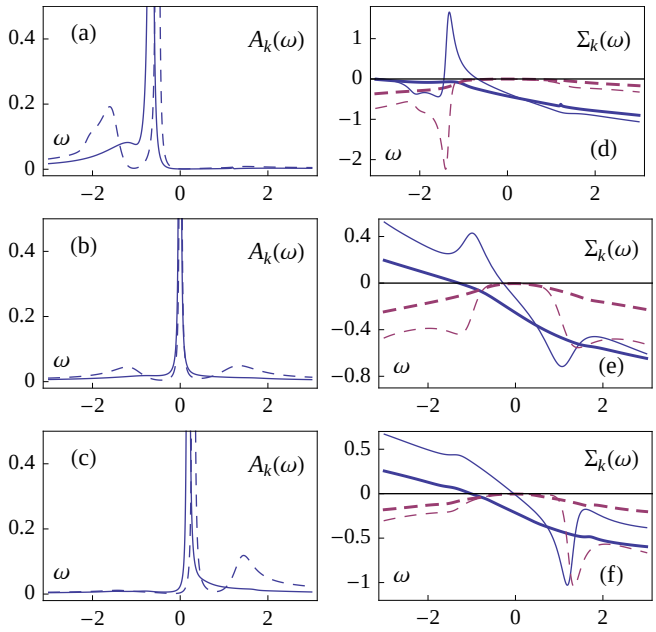

Figure 7.8: (Color online) $r_s = 7$. Left column: spectral weight in RPA (dashed line) and GW approximation (solid line) at $k \approx 0.76k_F$ (a), $k = k_F^*$ (b), $k \approx 1.20k_F$ (c). Right column: the real (blue solid line) and imaginary (red dashed line) part of the self-energy at $k \approx 0.76k_F$ (d), $k = k_F^*$ (e), $k \approx 1.20k_F$ (f) in RPA (thin line) and GW approximation (thick line).

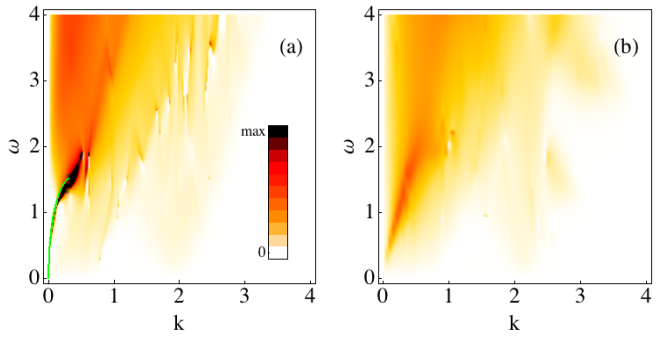

Figure 7.9: (Color online) $Im[-\epsilon_q^{-1}(\omega)]$ in RPA (a) and GW approximation (b) at $r_s = 7$ (same color intensity scale on both plots). Green solid line in (a) represents the plasmon dispersion expanded up to the second order in q. The unexpected discontinuities are artificial and due to difficulties with the analytic continuation of a two-particle function.

7.4.3 Quasiparticle weight and effective mass

Two important quantities that characterize interaction effects in a Fermi liquid are quasiparticle weight and effective mass. To derive the formulas for those quantities let us assume that $Im[\Sigma] \to 0$ (this approximation replaces Lorentzian

peaks by sharp delta peaks so we do not expect drastic changes in physics although it violates the Kramers-Kronig relation) in

$$A_k(\omega) = -2Im[G_k(\omega)] = \frac{-2Im[\Sigma_k(\omega)]}{(\omega - \epsilon_k - Re[\Sigma_k(\omega)])^2 + (Im[\Sigma_k(\omega)])^2} \tag{7.61}$$

yielding

$$A_k(\omega) = 2\pi\delta(\omega - \epsilon_k - Re[\Sigma_k(\omega)]). \tag{7.62}$$

Let E_k be the solution to the equation

$$\omega - \epsilon_k - Re[\Sigma_k(\omega)] = 0 \tag{7.63}$$

which represents a new quasiparticle dispersion relation. Using the well known property of the Dirac delta function

$$\delta[g(x)] = \frac{\delta(x - x_0)}{|g'(x_0)|} \tag{7.64}$$

where x_0 is zero of $g(x)$, the spectral function can be written as

$$A_k(\omega) = 2\pi Z_k \delta(\omega - E_k) \tag{7.65}$$

$$Z_k = \frac{1}{|1 - \frac{\partial}{\partial\omega} Re[\Sigma_k(\omega = E_k)]|}. \tag{7.66}$$

Eq. 7.65 has the same form as the non-interacting spectral function except the pre-factor Z_k called the renormalization factor. It represents the magnitude of Dirac delta function and thus gives an estimate of how much weight is contributed by a quasiparticle to the total spectral weight. Since the spectral function of a system obeys the sum rule quasiparticle weight Z_k corresponding to specific quasiparticle is smaller or equal to unity.

Eq. 7.63 can be used to define the effective mass. Since we are interested in low energy properties let us expand the dispersion relations for free and interacting particles around Fermi energy.

$$\epsilon_k = \frac{k^2}{2m} \approx \frac{k_F}{m}(k - k_F) \tag{7.67}$$

$$E_k \approx \frac{k_F}{m^*}(k - k_F) \tag{7.68}$$

The last equation serves as a definition of the efective mass reflecting the fact that E_k is a quasiparticle dispersion and not that of free particles. Next let us apply the derivative with respect to k to Eq. 7.63

$$\frac{dE_k}{dk} = \frac{d\epsilon_k}{dk} + \frac{\partial}{\partial k} Re[\Sigma_k(\omega = E_k)] + \frac{\partial}{\partial\omega} Re[\Sigma_k(\omega = E_k)] \frac{dE_k}{dk}$$

$$\frac{k_F}{m^*} = \frac{\frac{k_F}{m} + \frac{\partial}{\partial k} Re[\Sigma_k(\omega = E_k)]}{1 - \frac{\partial}{\partial\omega} Re[\Sigma_k(\omega = E_k)]}$$

$$\frac{m^*}{m} = \frac{Z_k^{-1}}{1 + \frac{m}{k_F}\frac{\partial}{\partial k} Re[\Sigma_k(\omega = E_k)]} \tag{7.69}$$

The quasiparticle weight Z and renormalized mas m^*, given in Table I, are computed for both the GW and RPA approximations at the Fermi energy and momentum using Eq. 7.66 and Eq. 7.69. As expected, the quasiparticle weight decreases with increasing interaction strength because the interaction shifts the weight from the coherent quasiparticle peak through incoherent scattering. Since the GW approximation does not yield the plasmaron peaks and the interaction gets more screened, most of the weight is concentrated in the Landau quasiparticle which results in a bigger quasiparticle weight than that in the case of RPA. The mass renormalization is less than 7% in both approximations meaning that we are dealing with a weakly interacting system.

	Z	m^*/m
RPA	0.798	0.978
GW	0.851	0.946

	Z	m^*/m
RPA	0.685	0.986
GW	0.806	0.929

Table 7.1: Quasiparticle weight Z and effective mass relative to the one of the free electron m^*/m at $r_s = 3$ (left) and $r_s = 7$ (right).

By comparing our RPA results with the ones obtained analytically, $Z \approx 0.722, m^*/m \approx 0.958$ at $r_s = 3$ and $Z \approx 0.625, m^*/m \approx 0.966$ at $r_s = 7$ [22], one can see that the agreement is quite good indicating that the periodized Greens function formalism works well.

Chapter 8

Paramagnetic Hubbard Model

Another application of the periodized Greens function method explored in this thesis is to Dynamical Mean Field Theory [3] fot the half-filled paramagnetic Hubbard model. As already mentioned in the introduction, DMFT method implies a set of equations which have to be solved self-consistently. As a solver of the DMFT equations we used IPT (Iterative Perturbation Theory) [3], [52], [53]. IPT is based on the diagrammatic expansion of a self-energy up to the second order with respect to the Hubbard interaction U, yielding the following set of diagrams,

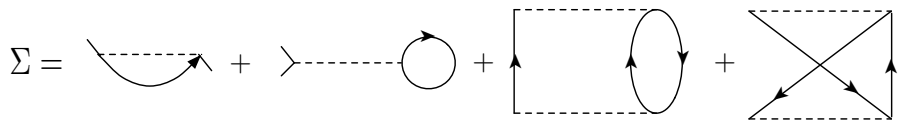

The Hubbard interaction $Un_\uparrow n_\downarrow$ requires same spin label for the Greens functions on each side of the interaction vertex. So, the first and second order exchange diagrams give zero contribution and thus we are left with the direct diagrams,

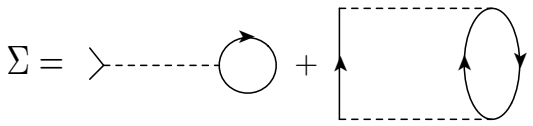

The contribution coming from these diagrams are

$$\Sigma^{(1)}(i\omega_n) = Un$$

$$\Sigma^{(2)}(i\omega_n) = -U^2 FT[G^2(\tau)G(-\tau)],$$

where n is an occupation number and FT stands for Fourier transform. The first order contribution is constant so it can be absorbed in the chemical potential.

Since IPT is based on the perturbation theory it is expected to work only in the weak coupling regime but as it turns out this method is relevant for strongly correlated cases, as well. The reason is that the IPT self-energy has correct atomic limit at half-filling. So, the application of IPT is limited to half-filling.

We observed that the convergence of the recursion for finding the fixed point for the DMFT equations using the periodized Greens functions was improved significantly by computing the self-energy as

$$\Sigma^{(2)}(i\omega_n) = \frac{1}{\eta}\text{arctanh}\left(-\eta U^2 FT[G^2(\tau)G(-\tau)]\right)$$

One can see that the expansion of $\tanh(\eta\Sigma(i\omega_n))$ is equivalent to the standard perturbative expansion up to second order in U and the function arctanh ensures that the imaginary part of the self-energy lies between 0 and π.

Fig. 8.1 shows the spectral function $A(\epsilon_k, \omega)$ for bare energies $\epsilon_k = -1, 0, 1$, at $\beta = 25$ ($T = W/50$), in the metallic $U = 2$ ($N = 25$) (a) and insulating $U = 4$ ($N = 45$) (b) phases which was computed using standard semicircular bare density of states. To solve the set of equations involved in the Padé procedure one has to do a matrix inversion. Since for the given parameters the entries of the matrix range from 10^{-33} to 10^{33} the calculation was done to the precision of 40 significant digits which allows us to do well defined numerical inversion and thus to solve the set of equations accurately. The locations of the poles on Fig. 8.1 c and 8.1 d are for $\epsilon_k = 0$. Since the self-energy is momentum independent in the DMFT formalism we do only one Padé fit for $\epsilon_k = 0$, then we express the self-energy through the periodized Dyson equation (Eq. 4.8) and reinsert it in the same equation where ϵ_k is not zero anymore. Thus, we can do the analytic continuation of the Greens function for any value of ϵ_k by performing just one Padé fit. The computation of the spectral function at low temperatures such as $\beta = 500$ also was performed and is presented on Fig 8.1 by dashed curve. It should be mentioned that the calculation at low temperatures requires more computational time because the number of frequencies needed to converge the IPT recursion algorithm is roughly $N \gtrsim \beta$ and a number of significant digits is order of N.

We also computed critical points for the metal-insulator phase transition which takes place in the above mentioned model. This phase transition has been studied by many authors [54], [55], [56] and it was shown that it is a first order phase transition, caused by the variation of the Hubbard coupling U, terminated at a critical point. The low temperature first order transition line $U_c(T)$ is inside the hysteresis region which contains both a metallic and an insulating states. At the critical temperature T_c the lines $U_c(T)$, $U_{c_1}(T)$ and $U_{c_2}(T)$ merge at the critical point $(U_c(T_c), T_c)$ (see, Fig. 8.4). $U_{c_1}(T)$ and $U_{c_2}(T)$ are the borders of the hysteresis region.

The DMFT equations are solved self-consistently, which is equivalent to finding a fixed point $\Sigma^*(i\omega_n)$ for those equations:

$$F_{U,\beta}(\Sigma^*) = \Sigma^*$$

$F_{U,\beta}$ is a formal representation of the DMFT equations and Σ is is an N-dimensional vector $(\Sigma(i\omega_0), \Sigma(i\omega_1), ..., \Sigma(i\omega_{N-1}))$. In order to carry out the fixed point analysis we calculate the Jacobian for the function $F_{U,\beta}$:

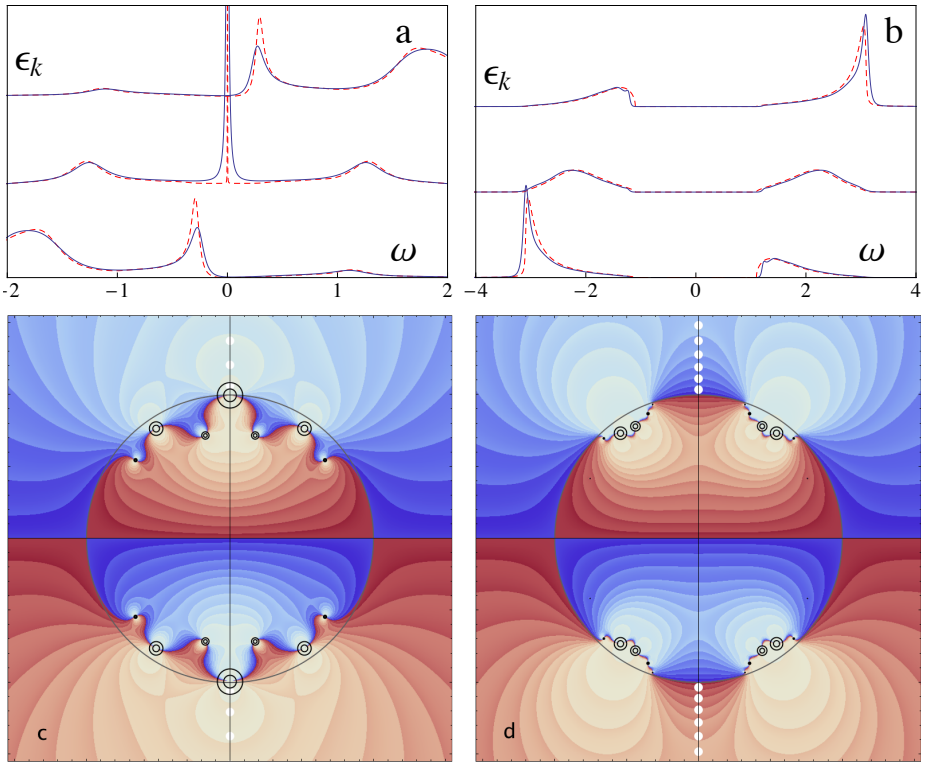

Figure 8.1: Spectral weight functions $A(\epsilon_k, \omega)$ for metal $U = 2$ (a) and insulator $U = 4$ (b) with bare energy in the full bandwidth $\epsilon_k = -1, 0, 1$. The locations of the poles are indicated by crosses and correspond to Padé fit in the case of $\epsilon_k = 0$. White dots represent the Matsubara frequencies.

$$J_F(\Sigma) \approx \frac{F_{U,\beta}(\Sigma + h\hat{z}_n) - F_{U,\beta}(\Sigma - h\hat{z}_n)}{2h}$$

where $\hat{z}_n$ is an unit vector in the periodized self-energy space and h is a finite discretization. The convergence of the recursion for finding the fixed point to the DMFT equations is determined by the largest eigenvalue, ϵ, of the Jacobian J_F. The common algorithm for searching the fixed point to the DMFT equations is the forward recursion, which provides the convergence only if $|\epsilon| < 1$. The more powerful algorithm is Newton's method [57] with better stability properties than forward recursion. Since the Newton's method is a root solver the fixed problem is reformulated in the following way:

$$R_{U,\beta}(\Sigma) \equiv F_{U,\beta}(\Sigma) - \Sigma$$

The fixed point of the function $F_{U,\beta}$ is the root of the function $R_{U,\beta}$. The Jacobian for $R_{U,\beta}$ can be calculated using J_F

$$J_R(\Sigma) = J_F - 1$$

It can be shown that the convergence can be achieved if the largest eigenvalue of J_F differs from one, $\epsilon \neq 1$. ϵ is equal to 1 exactly at the hysteresis boundaries

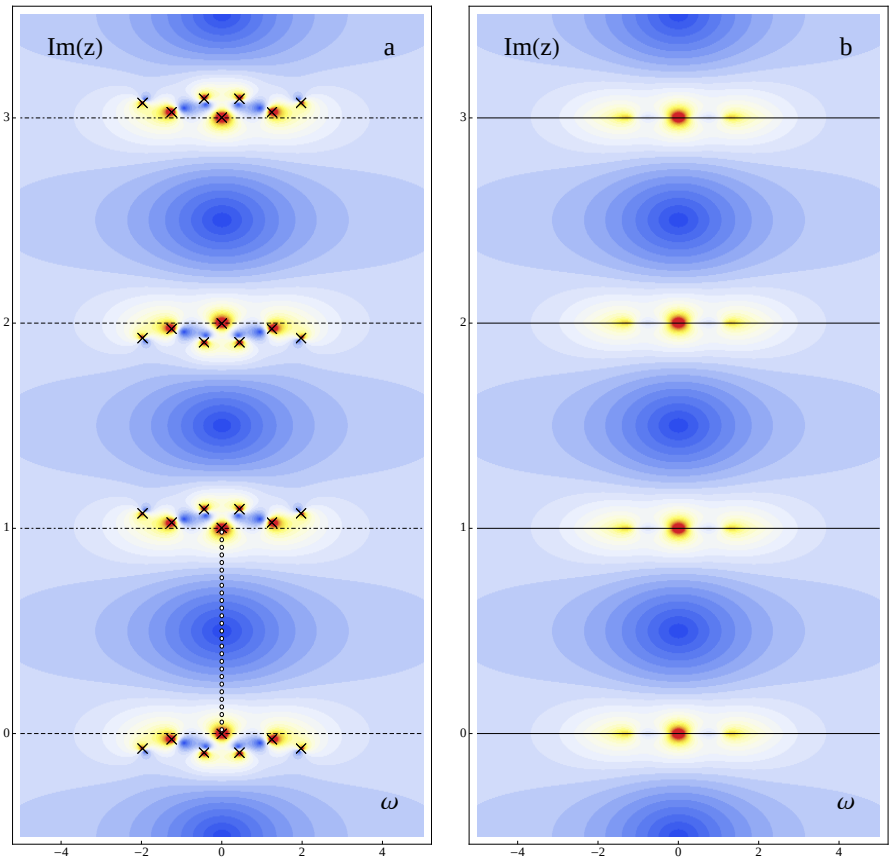

Figure 8.2: Analytic structure of the Greens function $G_{\epsilon_k=0}(z)$ in the metallic phase $U = 2$ ($Im[z]$ in units of Ω_N). In (a) the branch $Im[z] > 0$ is the domain for G^R which is analytic in $0 < Im[z] < \Omega_N$. Crosses indicate the locations of the poles (repeated with period of $i2\Omega_N$) and dot - the location of the Matsubara frequencies. In (b) the full Greens function with branch cuts at integer multiples of $i\Omega_N$

of the metall-insulator phase transition and it becomes larger than one inside the hysteresis region. To make the recursion converge for all values of the given parameter, ϵ, we define a new function:

$$f_{\beta,\Sigma(i\omega_0)}(U,\Sigma(i\omega_1),...,\Sigma(i\omega_{N-1})) = F_{U,\beta}(\Sigma(i\omega_0),\Sigma(i\omega_1),...,\Sigma(i\omega_{N-1}))-$$
$$-(\Sigma(i\omega_0),\Sigma(i\omega_1),...,\Sigma(i\omega_{N-1}))$$

It is clear that the root for the function $f_{\beta,\Sigma(i\omega_0)}$ is the fixed point for $F_{U,\beta}$. As one can see the free parameter is the first entry of the vector Σ instead of the Hubbard coupling U. We vary $\Sigma(i\omega_0)$ and obtain the vector $(U,\Sigma(i\omega_1),...,\Sigma(i\omega_{N-1}))$ as an output of the function $f_{\beta,\Sigma(i\omega_0)}$. $f_{\beta,\Sigma(i\omega_0)}$ is free of numerical instabili-

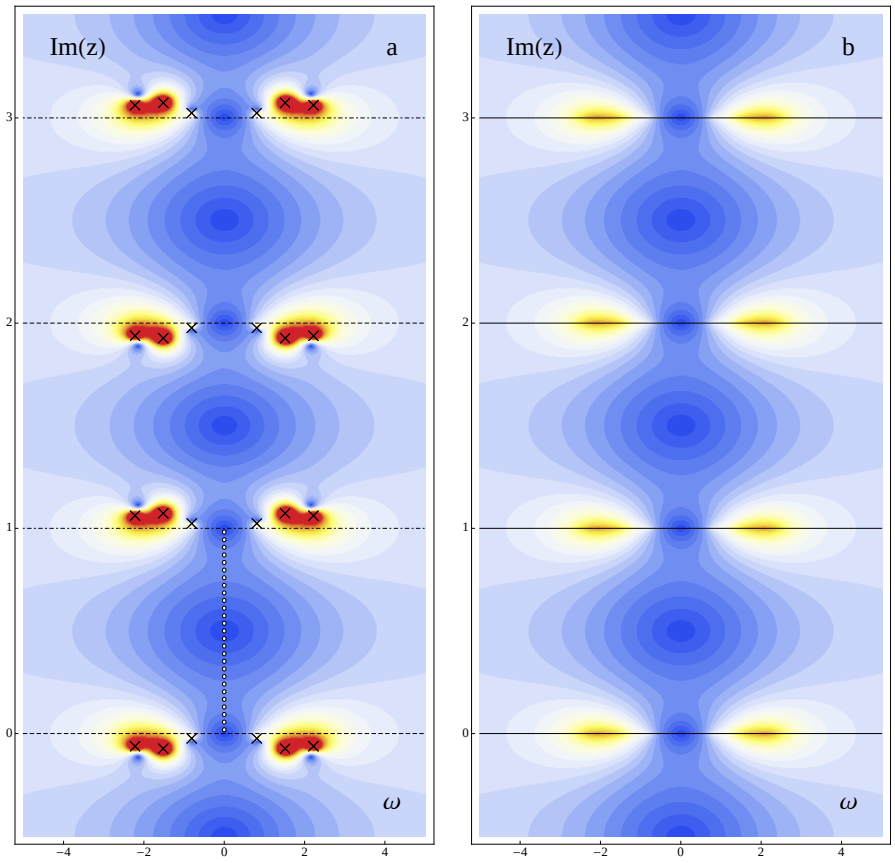

Figure 8.3: Analytic structure of the Greens function $G_{\epsilon_k=0}(z)$ in the insulating phase $U = 3$ ($Im[z]$ in units of Ω_N). In (a) the branch $Im[z] > 0$ is the domain for G^R which is analytic in $0 < Im[z] < \Omega_N$. Crosses indicate the locations of the poles (repeated with period of $i2\Omega_N$) and dot - the location of the Matsubara frequencies. In (b) the full Greens function with branch cuts at integer multiples of $i\Omega_N$

ties because it is a single-valued function (for each value of the parameter $\Sigma(i\omega_0)$ there is an unique solution $(U, \Sigma(i\omega_1), ..., \Sigma(i\omega_{N-1}))$), whereas $R_{U,\beta}(\Sigma)$ is a multivalued function inside the hysteresis region, $U_{c_1} < U < U_{c_2}$ and the solution to $f_{\beta,\Sigma(i\omega_0)}(U, \Sigma(i\omega_1), ..., \Sigma(i\omega_{N-1})) = 0$ is easily obtained using Newton's method . Thus, the new algorithm doesn't have trouble getting all the unstable and stable fixed points. As a demonstration of the existence of the unstable solution in the hysteresis region we compute a double occupancy $D = \sum_i n_{i,\uparrow} n_{i,\downarrow}$ (see Fig. 8.5) through the expectation value of the Hubbard interaction, $\langle V \rangle = \frac{1}{2} \sum_{\alpha,\beta,\gamma,\delta} V_{\alpha,\beta,\gamma,\delta} \langle c^\dagger_\alpha c^\dagger_\beta c_\delta c_\gamma \rangle$. First we write $\langle V \rangle$ in terms of the self-energy and thermal Greens function:

$$\langle V\rangle = \frac{1}{Z}Tr\left(e^{-\beta H}\frac{1}{2}\sum_{\alpha,\beta,\gamma,\delta}V_{\alpha,\beta,\gamma,\delta}\,c^{\dagger}_{\alpha}c^{\dagger}_{\beta}c_{\delta}c_{\gamma}\right)$$

$$= \frac{1}{Z}Tr\left(e^{-\beta H}\frac{1}{4}\sum_{\alpha,\beta,\gamma,\delta,\sigma}V_{\alpha,\beta,\gamma,\delta}\,c^{\dagger}_{\sigma}\left(\delta_{\sigma,\alpha}c^{\dagger}_{\beta}c_{\delta}c_{\gamma}-\delta_{\sigma,\beta}c^{\dagger}_{\alpha}c_{\delta}c_{\gamma}\right)\right) \tag{8.1}$$

Now, let us consider the derivative of $c_\sigma(\tau)$ with respect to τ:

$$\begin{aligned}\frac{\partial c_\sigma(\tau)}{\partial\tau} &= \frac{\partial}{\partial\tau}\left(e^{\tau H}c_\sigma\,e^{-\tau H}\right)\\ &= H\,c_\sigma(\tau)-c_\sigma(\tau)\,H\\ &= e^{\tau H}[H,c_\sigma]e^{-\tau H}\\ &= -\epsilon_\sigma c_\sigma(\tau)+e^{\tau H}\frac{1}{2}\sum_{\alpha,\beta,\gamma,\delta}V_{\alpha,\beta,\gamma,\delta}\left(-\delta_{\sigma,\alpha}c^{\dagger}_{\beta}c_{\delta}c_{\gamma}+\delta_{\sigma,\beta}c^{\dagger}_{\alpha}c_{\delta}c_{\gamma}\right)e^{-\tau H}\end{aligned} \tag{8.2}$$

where $H=\sum_\sigma\epsilon_\sigma c^{\dagger}_{\sigma}c_\sigma+\frac{1}{2}\sum_{\alpha,\beta,\gamma,\delta}V_{\alpha,\beta,\gamma,\delta}c^{\dagger}_{\alpha}c^{\dagger}_{\beta}c_{\delta}c_{\gamma}$ (chemical potential is included in ϵ_σ) and we used following commutators:

$$[c^{\dagger}_{\sigma}c_\sigma,c_\sigma]=-c_\sigma$$

$$[c^{\dagger}_{\alpha}c^{\dagger}_{\beta}c_{\delta}c_{\gamma},c_\sigma]=-\delta_{\sigma,\alpha}c^{\dagger}_{\beta}c_{\delta}c_{\gamma}+\delta_{\sigma,\beta}c^{\dagger}_{\alpha}c_{\delta}c_{\gamma}$$

Using Eq. 8.2 it is possible to rewrite Eq. 8.1 in the following way:

$$\begin{aligned}\langle V\rangle &= -\frac{1}{Z}Tr\left(e^{-\beta H}\frac{1}{2}\sum_{\sigma}c^{\dagger}_{\sigma}e^{-\tau H}(\partial_\tau+\epsilon_\sigma)c_\sigma(\tau)e^{\tau H}\right)\\ &= -\lim_{\tau'\to\tau^+}\frac{1}{Z}Tr\left(e^{-\beta H}\frac{1}{2}\sum_{\sigma}c^{\dagger}_{\sigma}(\tau')(\partial_\tau+\epsilon_\sigma)c_\sigma(\tau)\right)\end{aligned} \tag{8.3}$$

$$= -\frac{1}{2}\sum_{\sigma}\lim_{\tau'\to\tau^+}(\partial_\tau + \epsilon_\sigma)G_\sigma(\tau-\tau')$$

$$= -\frac{1}{2}\sum_{\sigma}\lim_{\tau'\to\tau^+}\int d\tau''\delta(\tau''-\tau)(\partial_{\tau''} + \epsilon_\sigma)G_\sigma(\tau''-\tau')$$

$$= \frac{1}{2}\sum_{\sigma}\lim_{\tau'\to\tau^+}\int d\tau'' G^{-1}_{0,\sigma}(\tau-\tau'')G_\sigma(\tau''-\tau')$$

$$= \frac{1}{2}\sum_{\sigma}\lim_{\tau'\to\tau^+}\int d\tau''(G^{-1}_{\sigma}(\tau-\tau'') + \Sigma_\sigma(\tau-\tau''))G_\sigma(\tau''-\tau')$$

$$= \frac{1}{2}\sum_{\sigma}\lim_{\tau'\to\tau^+}\left(\delta(\tau-\tau') + \int d\tau''\Sigma_\sigma(\tau-\tau'')G_\sigma(\tau''-\tau')\right)$$

$$= \frac{1}{2}\sum_{\sigma}\int d\tau''\Sigma_\sigma(\tau-\tau'')G_\sigma(\tau''-\tau)$$

$$= \frac{1}{2}\sum_{\sigma}\int d\tau\,\Sigma_\sigma(\tau)G_\sigma(-\tau) \tag{8.4}$$

here we used time translation invariance of the self-energy and Greens function and the following relation

$$\delta(\tau-\tau')(\partial_\tau + \epsilon_\sigma) = -G_0^{-1}(\tau'-\tau) \tag{8.5}$$

which follows from Eq. 8.6 (solving the differential equation in the Matsubara frequency space and then transforming back to imaginary time space with the help of the contour integral technique yields the expression for the free Greens function, Eq. 2.5. By plugging Eq. 2.5 in Eq. 8.6 one can see, without solving the differential equation, that the free Greens function obeys that relation)

$$(\partial_\tau + \epsilon_\sigma)G_0(\tau-\tau') = -\delta(\tau-\tau') \tag{8.6}$$

$$\int d\tau''\delta(\tau''-\tau)(\partial_{\tau''} + \epsilon_\sigma)G_0(\tau''-\tau') = -\int d\tau'' G_0^{-1}(\tau-\tau'')G_0(\tau''-\tau')$$

$$\delta(\tau''-\tau)(\partial_{\tau''} + \epsilon_\sigma) = -G_0^{-1}(\tau-\tau'')$$

Eq. 8.4 enables us to compute the double occupancy through the following relation

$$\langle D\rangle = \sum_i \langle n_{i,\uparrow}n_{i,\downarrow}\rangle = \frac{\langle V\rangle}{U}$$

Table 8.1: Comparison of (U_c, T_c) for the second order critical end-point.

	U_c (eV)	T_c (meV)
ED[53]	2.3398 ± 0.0030	25.5625 ± 0.0125
HF-QMC[59]	2.3325 ± 0.015	27.5 ± 0.2
HF-QMC[60]	2.38 ± 0.02	25.0 ± 3.0
ED[58]	2.34	25
NRG[54]	-	40
This work, IPT	2.46083 ± 0.00050	46.8940 ± 0.0544
IPT[61]	2.46315	46.895
IPT[62]	2.51	44.0

Since the first order diagram of the self-energy gives a constant contribution in this framework and acts like a chemical potential $\Sigma(\tau)$ actually represents only the second order diagram in U. Thus, the contribution of n_f^2, coming from the corresponding first order diagram for $\langle V \rangle$, is added to $\langle D \rangle$ in order to make $\langle V \rangle$ complete and restore the contribution coming from the first oder diagram of the self-energy, which is absorbed in the chemical potential.

Using new algorithm for finding the fixed points to the DMFT equations we find that the fixed point solutions form a continuous surface in (U, T, D) phase space, which previously was reported by Tong et. al. [58].

We also compute the maximum eigenvalue of J_f, the Jacobian for $f_{\beta,\Sigma(i\omega_0)}$, as a function of U around the critical temperature T_c, which, together with the double occupancy isotherms, helps us to understand the behaviour of the algorithm used to solve the DMFT equations. One can see from Fig. 8.5 that when $T > T_c$ the maximum eigenvalue ϵ is smaller than one and both the forward recursion and Newton's method converge. As T approaches to T_c ϵ tends to one causing a slowing down of the forward iteration and right at the critical point (U_c, T_c) when $\epsilon = 1$ Newton's method also becomes unstable for the first time. Below the critical temperature $T < T_c$ and for $U < U_{c_1}$ the metallic solution is found, which is annihilated by the unstable one through a saddle-node bifurcation at the second hysteresis boundary U_{c_2}. This coincides with $\epsilon \to 1^-$ which explains the slowing down of the forward recursion close to the hysteresis boundary. Since $\epsilon \geq 1$ in the hysteresis region the forward recursion is not able to find the unstable solution and the Newton's method is unstable at the hysteresis boundaries ($\epsilon = 1$). The much better alternative is the algorithm described above, which can find all solutions because it converges for any value of ϵ. The behaviour of the insulating solution at the first hysteresis boundary is analogous to that of the metallic solution.

Since the largest eigenvalue of the Jacobian J_f is equal to one $\epsilon = 1$ exactly at the critical point it is possible to compute T_c and $U_c(T_c)$. Let us define $U_\epsilon(T)$ which maximizes ϵ for a given temperature, see Fig. 8.5. It is obvious that $U_\epsilon(T_c) = U_c(T_c)$, which is not true away from the critical temperature T_c. We calculate $U_\epsilon(T)$ and ϵ for the different values of temperature, than using this data and the interpolation method two functions $T(\epsilon)$ and $U_\epsilon(\epsilon)$ are obtained, which enable us to determine the critical point $(T_c \equiv T(\epsilon = 1), U_c(T_c) \equiv U_\epsilon(\epsilon = 1))$. Our result is presented and compared to others in Tab. 8.1.

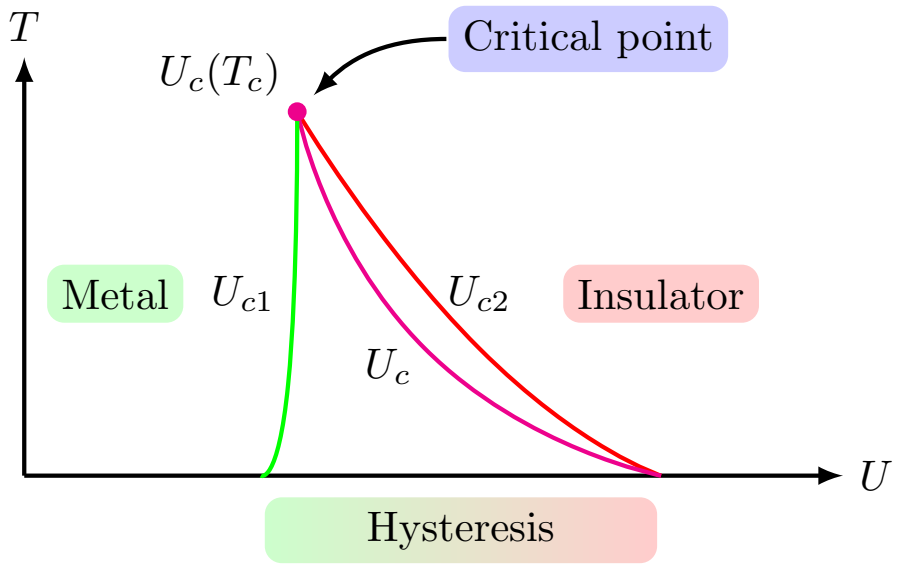

Figure 8.4: Phase diagram od the metall-insulator transition with the first order phase transition line U_c and the hysteresis boundaries U_{C_1}, U_{C_2}

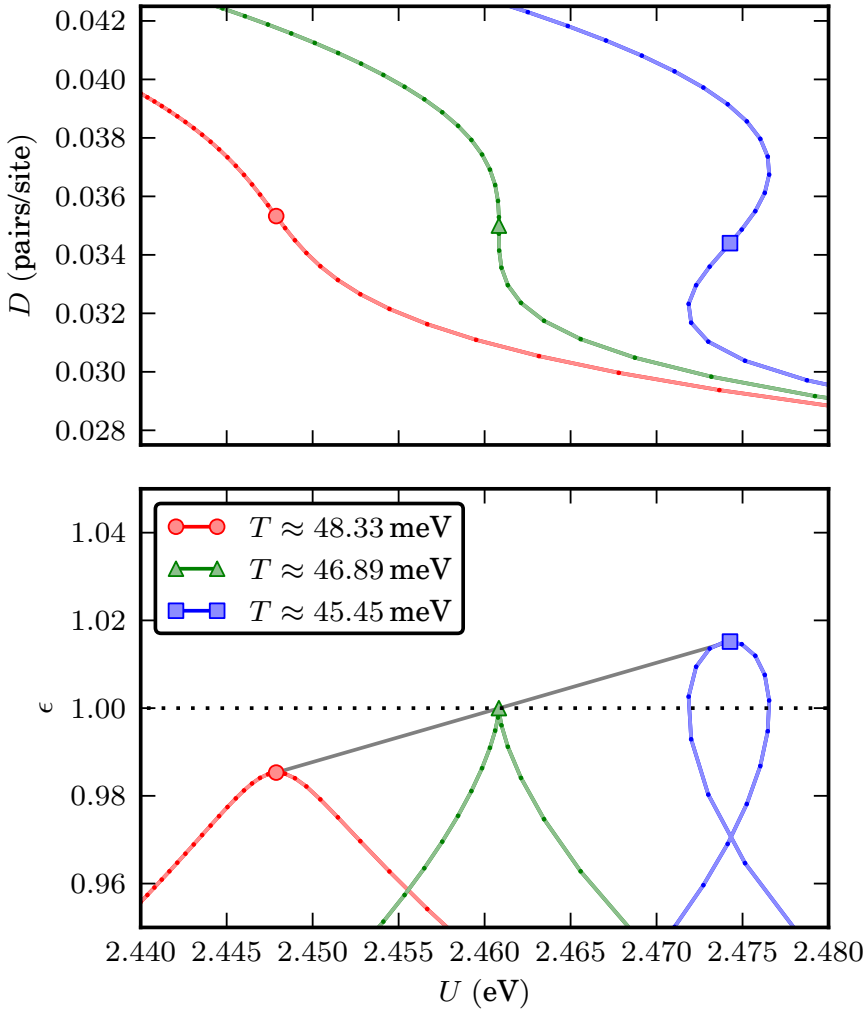

Figure 8.5: DMFT-IPT results for the double occupancy (upper panel) and maximum eigenvalue ϵ of J_f (lower panel) plotted against U above, close to and below the critical point (circles, triangles and squares respectively)

Chapter 9

Summary

This thesis describes a new approach to treat thermal Greens functions in numerical calculations. Self-consistent calculations involving thermal Greens functions are very demanding because large number of frequencies are required to capture the characteristics of the Greens function properly. The difficulties also arise when performing analytic continuation from the imaginary to real frequency axis.

The formalism described in this thesis differs from the standard methods in a sense that we can obtain a proper Greens functions and other related physical quantities within this formalism with a relatively small number of Matsubara frequencies (27 frequencies was used in the example presented in Chapter 6).

We start with the discretization of the non-interacting imaginary time Greens function $G_0(\tau)$ into N evenly spaced points. After performing the discrete Fourier transform we find that the Greens function in the imaginary frequency space is described by hyperbolic cotangent (Eq. 4.4) which is periodic along the imaginary axis and periodized Greens function reduces to the standard expression in the limit of infinitely large number of frequencies. Since $\lim_{\tau\to 0^-} G(\tau)$ and $\lim_{\tau\to 0^+} G(\tau)$ are not equal to each other (discontinuity at $\tau = 0$) we define the value of the Greens function at $\tau_j = 0$ in the following way $G(0) = (G(0^-) + G(0^+))/2 = n_f - 1/2$.

The Dyson equation $\Sigma = G_0^{-1} - G^{-1}$, which effectively represents G by an infinite series involving the free Greens function and self-energy, ordinarily enables us to compute the full Greens function. An alternative way to think of the Dyson series is the Taylor expansion of $G = 1/(G_0^{-1} - \Sigma) \equiv g(i\omega_n - \epsilon - \Sigma)$ in Σ around the free Greens function, where g denotes the inverse function. By defining g to be hyperbolic cotangent we write the periodized Dyson equation as Eq. 4.8, which yields standard Dyson equation in the limit $N \to \infty$. This form of the periodized Dyson equation preserves the property that the momentum and frequency independent self-energy acts as a chemical potential.

Next, we establish the variational principle in terms of the periodized Greens functions (Eq. 5.16) analogously to the Luttinger-Ward variational principle (Eq. 5.5). The Free energy corresponds to the stationary point of the Γ-functional . Demanding $\partial\Gamma/\partial G = 0$ and $\partial\Phi/\partial G = \Sigma$ yields the periodized Dyson equation, Eq. 4.8. It is remarkable that in the non-interacting limit the Γ-functional gives exact free energy for all values of N. In the limit $N \to \infty$ Eq. 5.16 gives standard Luttinger-Ward functional.

We also describe how to perform analytic continuation within the formalism. In analogy with the standard formalism the analytic continuation of the imaginary frequency Greens function is defined using Eq. 6.1, where $i\omega_n$ is replaced by complex variable z. We then model the spectral weight with properly normalised $L_{\epsilon,\gamma}(\omega)$ and after integration the analytic expression for $G(z)$ is obtained, which involves the coefficients that have to be determined. An example of the function $G(z)$ is plotted on Fig. 8.2. One can see that $G(z)$ is periodic $G(z) = G(z + 2i\Omega_N)$ and has branch cuts repeated with the period of $i\Omega_N$. It is analytic inside the strip $0 \leq Im[z] \leq i\Omega_N$ and has the poles outside that strip repeated with period of $2i\Omega_N$. In the limit $N \to \infty$ the periodized Greens function reproduces standard Greens function structure. To find those unknown coefficients $G(z)$ we transform Eq. 6.7 to Eq. 6.10 and do the Padé fit of the given Greens function values at N number of the Matsubara frequencies to Eq. 6.10. Working with a high precision is necessary to accurately solve the set of equations involved in the Padé fit and thus obtain a reliable analytic continuation from the imaginary to real frequency axis. Due to the periodicity the working space is relatively small which enables us to perform extremely high precision calculations efficiently. The fitting procedure preserves the normalisation of the total spectral weight, therefore the Greens function discontinuity in the imaginary time space and allows us to find the above mentioned coefficients which fully determines the function $G(z)$ and correspondingly the spectral function.

As an application of our formalism we studied the electronic structure for doped bilayer graphene in low energy limit. First of all low energy effective Hamiltonian is derived from the standard tight-binding 4×4 Hamiltonian. This derivation requires two approximations: expansion around one of the K points of the Brillouin zone and assumption that all relevant energy scales are much smaller than interlayer hopping parameter $t_\perp \approx 0.4$ eV. The resulting effective Hamiltonian is given by 2×2 matrix yielding two bands with parabolic dispersion. The interaction described by Coulomb potential is taken into account through the RPA and fully self-consistent GW approximation. After performing analytic continuation using the Padé method and taking the imaginary part of the trace of the dressed Greens function the full spectral function is obtained. As Fig. 7.6 shows in RPA there are satellite plasmaron peaks in the spectral function whereas plasmaron band in the fully self-consistent GW is washed out. Since we are interested in low energy properties it is instructive to look at the conductance band spectral function where the Fermi energy resides. The eigenvalue of the dressed Greens function corresponding to the conductance band gives us the spectral function projected on the conductance band. Same tendency is seen by looking at the projected spectral functions (left columns of Fig. 7.7 and 7.8): in RPA prominent plasmaron peaks are present while in the GW spectral function the plasmaron peaks are replaced by broad shoulders. Plasmaron peak moves towards the main quasiparticle with increasing k, around $k = k_F$ they merge and when k becomes greater than some specific value plasmaron peak reappears again. The right columns of Fig. 7.7 and 7.8 show real and imaginary parts of the corresponding self-energies. The strong oscillations in the real and imaginary parts of the RPA self-energy is associated with the plasmaron peak in the spectral function. There ar no oscillations in the GW self-energy. In addition we computed electron energy loss function, Fig. 7.9. In analogy with the picture we have for the spectral functions the RPA electron

energy loss function shows coherent plasmon mode and in GW plasmon mode is less coherent. Our RPA results obtained using periodized Greens function method is in a good agreement with other studies based on the standard Greens function theory and the RPA calculation.

Another application of the formalism is the computation of the DMFT-IPT recursions in terms of the periodized Greens functions and applied to the half-filled paramagnetic Hubbard Model with $N = 27$. The results are presented on Fig. 8.1. We believe that the method presented in this thesis can be used in the variety of problems which involve and require numerical evaluation of the thermal Greens functions.

Appendices

Appendix A

Imaginary Time Greens Function Symmetries

From the definition of the imaginary time Greens function definition we can see that it is real. This gives symmetry in the periodized Matsubara frequency Greens function. To see this we start with the discrete Fourier transformation

$$G(i\omega_n) = \frac{\beta}{N} \sum_{j=0}^{N-1} e^{i\omega_n \tau_j} G(\tau_j) \tag{A.1}$$

Since $e^{i\Omega_N \tau_j}$ ($\Omega_N = 2\pi N/\beta$) is identically one. It allows us to write the following equality $e^{-i\tau_j \omega_n} = e^{-i\tau_j(\omega_n + \Omega_N)}$. Using the definition for the Matsubara frequencies ω_n one can show that

$$\begin{aligned} \omega_n + \Omega_N &= \pi/\beta(2n + 1 + 2N) = \omega_{n+N} \\ e^{-i\tau_j \omega_n} &= e^{-i\tau_j(\omega_{n+N})} \end{aligned}$$

Using the latter relation one can see that

$$G(i\omega_0) = \frac{\beta}{N} \sum_{j=0}^{N-1} e^{i\omega_0 \tau_j} G(\tau_j) = \frac{\beta}{N} \sum_{j=0}^{N-1} e^{i\frac{\pi}{\beta}\tau_j} G(\tau_j)$$

is complex conjugate to

$$G(i\omega_{N-1}) = \frac{\beta}{N} \sum_{j=0}^{N-1} e^{i\omega_{N-1} \tau_j} G(\tau_j) = \frac{\beta}{N} \sum_{j=0}^{N-1} e^{-i\frac{\pi}{\beta}\tau_j} G(\tau_j)$$

It is clear that if we do the same calculation for the pairs: $G(i\omega_1)$ and $G(i\omega_{N-2})$, $G(i\omega_2)$ and $G(i\omega_{N-3})$ etc. we get analogous result: each pair represents complex conjugate quantities. This means that the discretized thermal Greens function in the frequency space has the following symmetry: $G(i\omega_n) = G^*(i\omega_{N-1-n})$, $n = 0, .., N-1$.

The imaginary time Greens function is antiperiodic, $G(-\tau) = -G(\beta - \tau)$. For the discretized thermal Greens function we have:

$$G(-\tau_j) = \begin{cases} -G(\beta - \tau_j) & if \quad \beta > \tau_j > 0 \\ G(\tau_j) & if \quad \tau_j = 0 \end{cases}$$

where, $G(\tau_j = 0) = n_f - 1/2$ (See Fig. A.1).

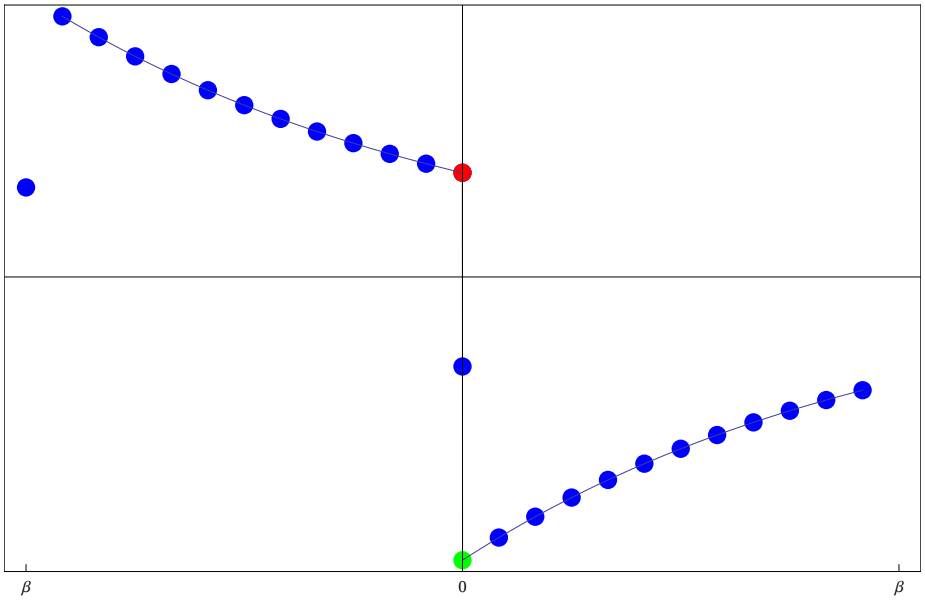

Figure A.1: The blue dots represent discretized non interacting Greens function $G_0(\tau_j)$ for $N = 12$. The red and green dots correspond to the $G_0(\tau = 0^-) = n_f$ and $G_0(\tau = 0^+) = n_f - 1$ limits, respectively, while the blue one on the Y axis represents our definition of the $G(\tau = 0)$, which is $n_f - 1/2$.

Let us show that in the case of particle-hole symmetry and for $\tau_j \neq 0$ the summation over momentum k in the Greens functions yields: $G(\beta - \tau) = G(\tau)$. To do this first we define the particle-hole transformation in terms of annihilation and creation operators provided that a corresponding Hamiltonian is defined on the lattice:

$$c_j^\dagger \rightarrow (-1)^j d_j$$

$$c_j \rightarrow (-1)^j d_j^\dagger$$

which can be transformed in momentum space using $c_j = \frac{1}{\sqrt{N}} \sum_k e^{ikj} c_k$:

$$c_k^\dagger \rightarrow d_{\pi - k}$$

$$c_k \rightarrow d_{\pi - k}^\dagger$$

Using these transformations one can see how the Greens function transforms under particle-hole transformation:

$$
\begin{aligned}
G_{\pi-k}(i\omega_n) &= \int_0^\beta d\tau\, e^{i\omega_n\tau} G_{\pi-k}(\tau) \\
&= -\int_0^\beta d\tau\, e^{i\omega_n\tau} \langle c_{\pi-k}(\tau) c^\dagger_{\pi-k}(0)\rangle \\
&= -\int_0^\beta d\tau\, e^{i\omega_n\tau} \langle c^\dagger_{k}(\tau) c_{k}(0)\rangle \\
&= -\int_0^\beta d\tau\, e^{i\omega_n\tau} \langle c^\dagger_{k}(0) c_{k}(-\tau)\rangle \\
&= -\int_0^\beta d\tau\, e^{i\omega_n\tau} G_k(-\tau) \\
&= \int_0^\beta d\tau\, e^{i\omega_n\tau} G_k(\beta-\tau) \\
&= \int_0^\beta d\tau\, e^{i\omega_n(\beta-\tau)} G_k(\tau) \\
&= -\int_0^\beta d\tau\, e^{-i\omega_n\tau} G_k(\tau) \\
&= -G^*_k(i\omega_n)
\end{aligned}
\tag{A.2}
$$

here we used that the Greens function is anti-periodic, real and has time translation symmetry. After performing the summation over k in Eq. A.2 one can see that the Greens function components in the Matsubara frequency space are purely imaginary: $G(i\omega_n) = -G^*(i\omega_n)$. By applying the Fourier transformation to both sides of the latter equality we get:

$$
\frac{1}{\beta}\sum_0^{N-1} e^{-i\omega_n\tau} G(i\omega_n) = -\frac{1}{\beta}\sum_0^{N-1} e^{-i\omega_n\tau} G^*(i\omega_n)
$$

$$
G(\tau) = -G^*(-\tau)
$$

$$
G(\tau) = -G(-\tau)
$$

$$
G(\tau) = G(\beta-\tau)
$$

Appendix B

Derivation of the Delta Function

In order to prove $\sum_n e^{i\omega_n \tau} = \beta\delta(\tau)$ consider the integral

$$\int_0^\beta d\tau \sum_n e^{i\omega_n \tau} f(\tau) = \int_0^\beta d\tau \sum_{n,n'} e^{i\omega_n \tau} \frac{1}{\beta} e^{-i\omega'_n \tau} f(i\omega_n)$$

$$= \frac{1}{\beta} \int_0^\beta d\tau \sum_{n,n'} e^{i\frac{2\pi}{\beta}(n-n')\tau} f(i\omega_n)$$

when $n = n'$ the integral yields $\sum_n f(i\omega_n) = \beta f(\tau = 0)$. If $n \neq n'$ the integral is just zero. So,

$$\int_0^\beta d\tau \sum_n e^{i\omega_n \tau} f(\tau) = \beta f(\tau = 0) \Rightarrow \sum_n e^{i\omega_n \tau} = \beta\delta(\tau)$$

Appendix C

Calculation of the expectation value of a Hamiltonian

$$
\begin{aligned}
\langle H-\mu N_\mu\rangle &= \frac{1}{Z}Tr[(H-\mu N_\mu)e^{-\beta(H-\mu N_\mu)}] \\
&= -\frac{d(\log Z)}{d\beta} = \frac{d(\beta\Omega)}{d\beta} = \\
&= \frac{d}{d\beta}(\Phi[G] - Tr\, G^+(i\omega_n)\Sigma(i\omega_n) + Tr(\log(-G^-(i\omega_n)/2\eta))) \\
&= \frac{\partial\Phi}{\partial G}\frac{dG}{d\beta} - Tr\left[\frac{dG^+}{d\beta}\Sigma\right] - Tr\left[\frac{d\Sigma}{d\beta}G^+\right] + \\
&\quad + Tr\left[\left(-\frac{2\eta}{G^-}\right)\frac{d}{d\beta}\left(-\frac{N}{\beta}G^-\right)\right] \\
&= -Tr\left[\frac{\Sigma}{2N}\right] - Tr\left[G^+\frac{d}{d\beta}\left(\frac{N}{\beta}\log\left(\frac{G^-}{G^+}\frac{G_0^+}{G_0^-}\right)\right)\right] + \\
&\quad + Tr\left[\frac{1}{G^-}\left(\frac{dG}{d\beta} - \frac{1}{2N} - \frac{G^-}{\beta}\right)\right] \\
&= -Tr\left[\frac{\Sigma}{2N}\right] - Tr\left[G^+\left\{-\frac{\Sigma}{\beta} + \frac{N}{\beta}\left(\frac{G^+}{G^-}\frac{d}{d\beta}\left(\frac{G^-}{G^+}\right) + \frac{G_0^-}{G_0^+}\frac{d}{d\beta}\left(\frac{G_0^+}{G_0^-}\right)\right)\right\}\right] +
\end{aligned}
$$

$$+ Tr\left[\frac{1}{G^-}\left(\frac{dG}{d\beta} - \frac{1}{2N} - \frac{G^-}{\beta}\right)\right]$$

$$= Tr\left[\frac{G^+\Sigma}{\beta} - \frac{\Sigma}{2N}\right] - Tr\left[G^+\left(\frac{1}{G^-G^+}\frac{dG}{d\beta} - \frac{1}{\beta}\frac{G}{G^-G^+} + \frac{1}{\beta}\frac{G_0}{G_0^-G_0^+} - \right.\right.$$

$$\left.\left. - \frac{1}{G_0^-G_0^+}\frac{dG_0}{d\beta}\right)\right] + Tr\left[\frac{1}{G^-}\left(\frac{dG}{d\beta}\right)\right] + Tr\left[\frac{1}{G^-}\left(-\frac{1}{2N} - \frac{G^-}{\beta}\right)\right]$$

$$= \frac{1}{\beta}Tr\left[G\Sigma\right] + Tr\left[\frac{1}{\beta}\frac{G}{G^-} - \frac{1}{2NG^-} - \frac{1}{\beta}\right] + Tr\left[\frac{G^+}{G_0^-G_0^+}\left(\frac{dG_0}{d\beta} - \frac{G_0}{\beta}\right)\right]$$

$$= \frac{1}{\beta}Tr\left[G\Sigma\right] + Tr\left[\frac{G^+}{G_0^-G_0^+}\left(\frac{d}{d\beta}(\eta\ \coth\ \eta(i\omega_n - \epsilon + \mu)) - \frac{G_0}{\beta}\right)\right]$$

$$= \frac{1}{\beta}Tr\left[G\Sigma\right] + Tr\left[\frac{G^+}{G_0^-G_0^+}\left(\frac{G_0}{\beta} + \frac{\beta}{(2N)^2}\frac{\epsilon - \mu}{\sinh^2\eta(i\omega_n - \epsilon + \mu)} - \frac{G_0}{\beta}\right)\right]$$

$$= \frac{1}{\beta}Tr\left[G\Sigma\right] + Tr\left[\left(\frac{2N}{\beta}\right)^2\frac{G^+}{(\coth^2(i\omega_n - \epsilon + \mu) - 1)}\frac{\beta}{(2N)^2}\frac{\epsilon - \mu}{\sinh^2\eta(i\omega_n - \epsilon + \mu)}\right]$$

$$= \frac{1}{\beta}Tr\left[G\Sigma\right] + \frac{1}{\beta}Tr[G^+(\epsilon - \mu)]$$

$$= \frac{1}{\beta}Tr\left[G(i\omega_n)(\Sigma(i\omega_n) + \epsilon - \mu) + \eta(\epsilon - \mu)\right]$$

Appendix D

Review of the Padé Method Applications

In 1977 H. J. Vidberg and J. W. Serene published a paper where they apply the Padé technique to the solutions of the imaginary frequency Eliashberg equations [5]. The authors fit given Greens function values at N Matsubara frequencies to the continued fraction, called N-point Padé approximant. The recursive algorithm presented in the paper allows us to write the continued fraction as a ratio of the two polynomials $C_N(z) = A_N(z)/B_N(z)$ and compute the value of the Padé approximant at a given point. The method works better at low temperatures because the distance between the Matsubara frequencies decreases. The polynomials A_N and B_N are of order $(N-1)/2$ and $(N-1)/2$ for odd N, while A_N is order of $(N-2)/2$ and B_N - $N/2$ for even N [6]. The authors conclude that in order to get a good approximation the number of input points need to be such that it should capture the asymptotic of the function. Appearance of the unnecessary pole-zero pairs which cancel each other does not affect the function behaviour on the real axis and it means that the number of input points could be lowered. In addition, they mention that the Padé method is very sensitive to the precision of the data used in the recursion. Due to the insufficient level of the precision they can not describe the fine structure of the Greens function on the real axis. Since the difference between Matsubara points increases with increasing temperature the Padé method described in [5] is not reliable at high temperatures.

R. Blaschke and R. Blocksdorf [63] improved the Padé method introduced by Vidberg and Serene. In order to handle the problems related to the appearance of the spurious poles near the real axis and in the upper half plane and the pole of the imaginary part of the renormalization function (which is one of the terms in the Eliashberg equations [5]) at zero energy they use small number of points sufficient to describe the main structure of the renormalization function and additional points at higher energies. The authors also remove the part, containing the pole, from the renormalization function. As a result Padé approximant a gives very good agreement with the real axis solutions, in particular at larger energies.

C. R. Leavens and D. S. Ritchie [64] suggested another improvement over the Padé technique presented in [5]. In order to get accurate results for the

high temperatures these authors replace one of the original points with one which describes exact finite temperature behaviour for small frequencies. The recursion procedure [5] with the modified data gives divergence. To overcome this difficulty authors modify the values of the gap function by adding some constant (which shouldn't differ too much from the given data) or dividing by the Matsubara frequencies. The new data yields correct finite temperature limit as frequency goes to zero.

F. Marsiglio and co-authors [65] introduced a different approach to the analytic continuation for self-energy defined on the imaginary frequency axis. Using the spectral representation of the propagators and Poisson summation formula (used to sum over Matsubara frequencies) the self-energy equation can be written in terms of the real frequency. This equation can be solved by representing it with principal-value integrals and residues, which is quite hard task. In order to avoid these problems authors perform integration over complex variable z (this integral appears in the self-energy equation after replacing imaginary frequency Greens function with its spectral representation) in the real-frequency self-energy equation thereby they obtain the self-energy written in terms of the spectral function and retarded Greens function defined on the Matsubara frequencies. The Greens function values at the Matsubara frequencies can be calculated using imaginary frequency equations and therefore one can solve real-frequency self-energy equation self-consistently on the real axis. According to [65] in the zero temperature limit no iterations are required and at finite temperatures only a few iterations are sufficient for convergence. The results obtained with this procedure at low temperatures are in a good agrement with those computed directly with the real axis equations.

Apart from the Padé method there are other techniques available to do the analytic continuation of the thermal Greens functions in the specific many-body problems [66], [7]. In [7] the maximum-entropy method is used to perform the analytic continuation from the imaginary to real frequencies.

In the paper by K. S. D. Beach, R. J. Gooding and F. Marsiglio [67] it is shown that representing the Padé approximant as terminating continued fraction is equivalent to a rational polynomial form. The authors work with the rational polynomials due to the computational purposes. In this case one writes a linear set of equations for the polynomial and therefore the problem is reduced to the matrix inversion. Once the polynomial coefficients are found the equivalent continued fraction coefficients can be calculated, which with theorem by Wall and Wetzel [68] gives an information about the sign and integrability for the spectral function and analyticity of the Greens function. As they claim one can use the convergence of the imaginary part of the specific continued fraction coefficient (which has to be real and positive according to the Wall and Wetzel theorem) to zero to determine the threshold of the accuracy which gives more or less exact Padé fit and the number of poles for the true Greens function.

In [69] and [70] authors conclude that the Padé method is reliable only at zero temperature and small interactions and it can not give the fine structure of the spectral weight. Namely, [69] provides us with the test which is the following: authors consider an infinite tight-binding chain with a single site impurity, which is an exactly solvable system and a special case of the single impurity Anderson model without Coulomb interaction. They compute the spectral function using the Padé method which comes out very inaccurate compare to the exact spectral function. We did the same test using our method with 61 Matsubara

frequencies and 60 significant digits at $\beta = 25$. The result is represented on Fig. D.1 upper panel . As one can see the spectral function obtained with the Padé method is very accurate. In fact, exact $A(\omega)$ and the one computed by performing the analytic continuation sit on top of each other, they are almost indistinguishable to eye. Both the continuous part and delta function fits the exact curve. The lower panel of the same figure shows exactly same Padé fit but with 17 Matsubara frequencies and smaller precision (16 significant digits). As one can see the result extremely depends on the precision of the given data and number of Matsubara frequencies.

In the end I should mention that the Padé method is a useful tool not only in condensed matter physics. It is used in the various problems of physics: quantum field theory, nuclear physics [71], etc. So, it is important to improve the Padé technique by making it more stable and less ill-posed method which will helps us to solve various problems.

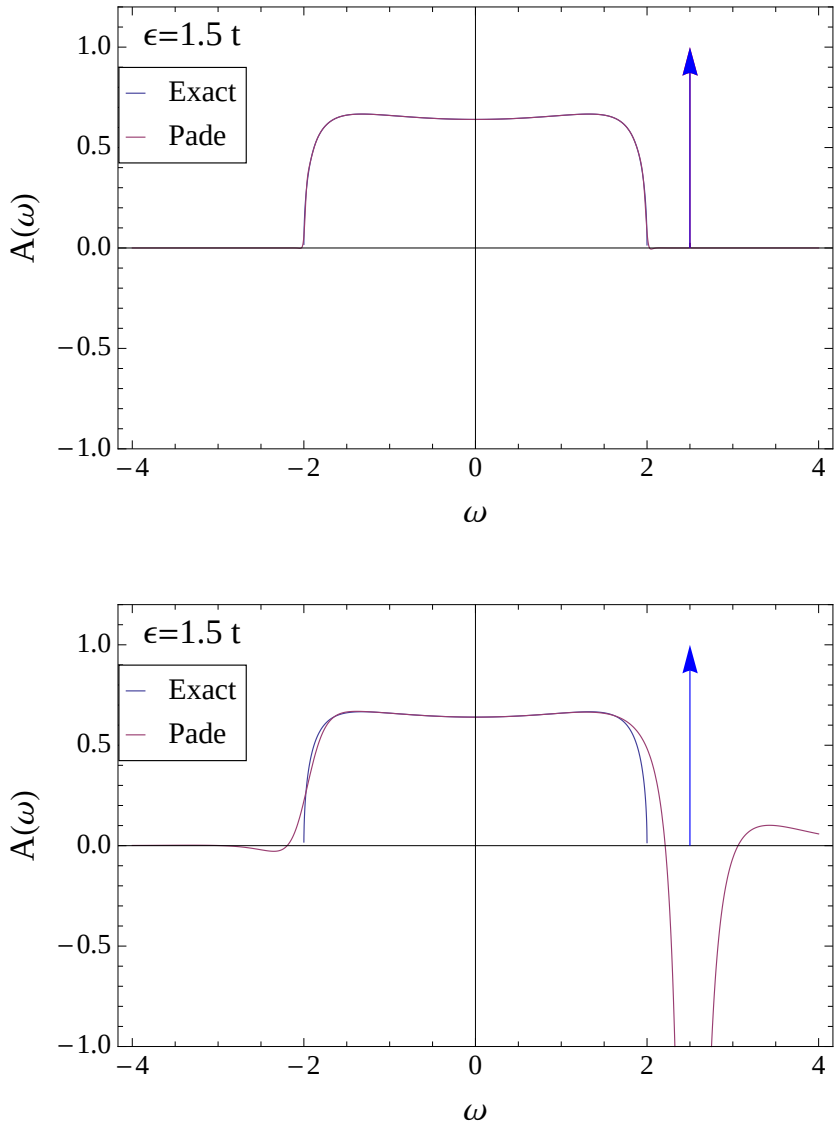

Figure D.1: Upper panel: comparison between the exact spectral function and the one computed by the Padé method with the precision of 60 significant digits for an infinite tight-binding chain with a single impurity at $\beta = 25$. An arrow indicates the presence of the delta function. Lower panel: Same comparison as in the upper panel but the Padé fit is done with the precision of 16 significant digits

Appendix E

Hedin's Equations

The first Hedin's equation is the well known Dyson equation, Eq. E.1. The second one relates the screened interaction with polarization Π and bare interaction V, Eq. E.2. Π is in general two-particle Green's function. In terms of the Feynman diagrams it is a set of digrams with left and right sides connected by two Green's functions including vertex corrections Γ^* and no external interaction lines [23, 32], Eq. E.3. In addition, Π and Γ^* represent irreducible diagrams which implies that those diagrams can not be separated into left and right parts by cutting one interaction line.

$$G(x,x') = G_0(x,x') + \sum_{x'',x'''} G_0(x,x'')\Sigma(x'',x''')G(x''',x') \tag{E.1}$$

$$W(x,x') = V(x-x') + \sum_{x'',x'''} V(x-x'')\Pi(x'',x''')W(x''',x') \tag{E.2}$$

$$\begin{aligned}\Pi(x,x') = &\sum_{x''} G(x,x'')G(x'',x')+ \\ &+ \sum_{x'',x''',x^{IV},x^{V}} G(x,x'')G(x'',x''')\Gamma^*(x''',x^{IV})G(x^{IV},x^{V})G(x^{V},x')\end{aligned} \tag{E.3}$$

where $x = (\mathbf{r}, \tau)$. The last equation of Hedin is equation of motion for the self-energy. It can be derived by computing the derivative of $G(x,x')$ with respect

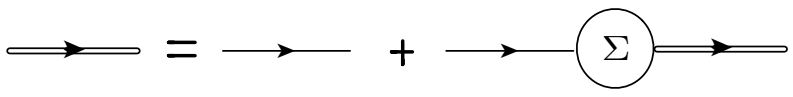

Figure E.1: Dyson equation (Eq. E.1) in terms of the Feynman diagrams.

to the imaginary time,

$$-\frac{\partial G(x,x')}{\partial \tau_1} = \delta(x-x') + H_0 G(x,x') - V(x-x'')\langle T c(x) c^\dagger(x'') c(x'') c^\dagger(x')\rangle. \tag{E.4}$$

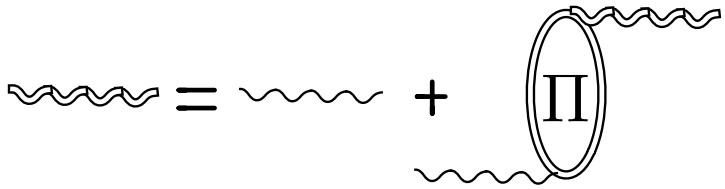

Figure E.2: Effective interaction (Eq. E.2) in terms of the Feynman diagrams.

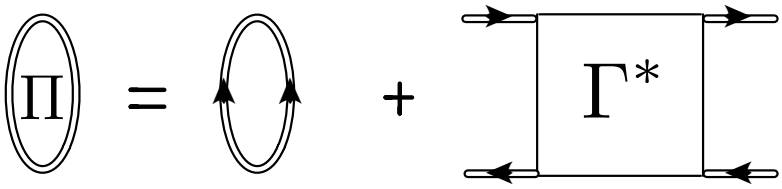

Figure E.3: Polarization (Eq. E.3) in terms of the Feynman diagrams.

The latter expresion was derived using Heisenberg equation of motion,

$$-\frac{\partial c(x)}{\partial \tau} = [c(x), H]. \tag{E.5}$$

The last term in Eq. E.4, interaction times a two-particle Green's function, is defined to be the product of the self-energy and Green's function. Using Eq. E.3 which relates two-particle Green's function to vertex one can obtain the following expression for the self-energy

$$\Sigma(x,x') = -\sum_{x''} V(x,x'')G(x'',x')- \\ - \sum_{x'',x''',x^{iV},x^{V}} V(x,x'')G(x'',x''')G(x''',x^{IV})G(x^{IV},x^{V})\Gamma(x^{V},x'), \tag{E.6}$$

where Γ is full vertex i.e. includes both reducible and irreducible vertices.

In order to rewrite the latter expression in terms of the screened interaction let us introduce particle-hole irreducible vertex Γ_{ph} (during this derivation space-time label x is dropped for the brevity). It is a set of diagrams which can not be separated into two parts by cutting two Green's function lines. Using Γ_{ph} and $\Gamma^*_{ph} = \Gamma_{ph} - V$ we obtain the following relations

$$\Gamma = \Gamma_{ph} + \Gamma_{ph}GG\Gamma \tag{E.7}$$

$$\Gamma^* = \Gamma^*_{ph} + \Gamma^*_{ph}GG\Gamma^*. \tag{E.8}$$

SInce Γ^* is in Eq. E.3 and the polarization is supposed to be irreducible we have to exclude the bare interaction and that is why Γ^*_{ph} is introduced. After

writing Γ in terms of Γ^* by means of the last two equation we get

$$\Gamma = \left(\Gamma^*(1+GG\Gamma^*)^{-1}+V\right)\left(1-GG\left(\Gamma^*(1+GG\Gamma^*)^{-1}+V\right)\right)^{-1} \tag{E.9}$$

which after inserting identities $1=(1+GG\Gamma^*)^{-1}(1+GG\Gamma^*)$ and $1=V^{-1}V$ transforms to

$$\Gamma = \left(\Gamma^*(1+GG\Gamma^*)^{-1}+V\right)V^{-1}V(1-\Pi V)^{-1}(1+GG\Gamma^*) \tag{E.10}$$

where Eq. E.3 was used. Using the relations

$$W = V(1-\Pi V)^{-1} \tag{E.11}$$

$$V^{-1} = W^{-1}+\Pi = W^{-1}+GG+GG\Gamma^*GG \tag{E.12}$$

in the last expression we arrive to

$$\Gamma = \Gamma^*+\Gamma^*GGW+\Gamma^*GGWGG\Gamma^*+WGG\Gamma^*+W. \tag{E.13}$$

Inserting the latter equation in Eq. E.6 and then using $V\Pi W = W-V$ yields

$$\Sigma = -GW-GW\Gamma^*. \tag{E.14}$$

In order to generate GW approximation from Hedin's equations $\Gamma^*(x,x')$ is set to be zero. As a result of this approximation one obtains

$$\Sigma^{GW}_{\vec{k}}(i\omega_n) = \frac{1}{\beta}\int\frac{d^2q}{(2\pi)^2}\sum_{m=-\infty}^{\infty}W_{\vec{q}}(i\omega_m)G_{\vec{k}-\vec{q}}(i\omega_n-i\omega_m). \tag{E.15}$$

Here the self-energy (and all expression below) is written in the momentum$\vec{k}$ and imaginary (Matsubara) frequency space $i\omega_n$. Quantum numbers like momentum and spin are combines in $\vec{k}$ and $\vec{q}$ labels.

Eq. E.3 reduces to

$$\Pi_{\vec{q}}(i\omega_n) = -g\int\frac{d^2k}{(2\pi)^2}\frac{1}{\beta}\sum_{m=-\infty}^{\infty}G_{\vec{k}}(i\omega_m)G_{\vec{k}+\vec{q}}(i\omega_n+i\omega_m) \tag{E.16}$$

where g is a degeneracy factor. Since we are dealing with fermionic Green's functions they are functions of fermionic Matsubara frequencies and consequently the polarization $\Pi_{\vec{q}}(i\omega_n)$ together with the screened interaction $W_{\vec{q}}(i\omega_n)$ are functions of bosonic Matsubara frequencies, $\omega_n = 2\pi n/\beta$.

Equation for $W_{\vec{q}}(i\omega_n)$ in the GW approximation has the same form as Eq. E.2 but the polarization is computed through Eq. E.16,

$$W_{\vec{q}}(i\omega_n) = \frac{V_q}{1+V_q\Pi_{\vec{q}}(i\omega_n)}. \tag{E.17}$$

V_q is a bare interaction Fourier transformed in the momentum space. It is evident that Eq. E.17 is a sum of infinite geometric sieres which diagrammatically has the following form

After computing $\Sigma^{GW}_{\vec{k}}(i\omega_n)$ (first diagram in Fig. E.5) one should, in general, add the Hartree diagram (second diagram in Fig. E.5) to it which gives $q=0$

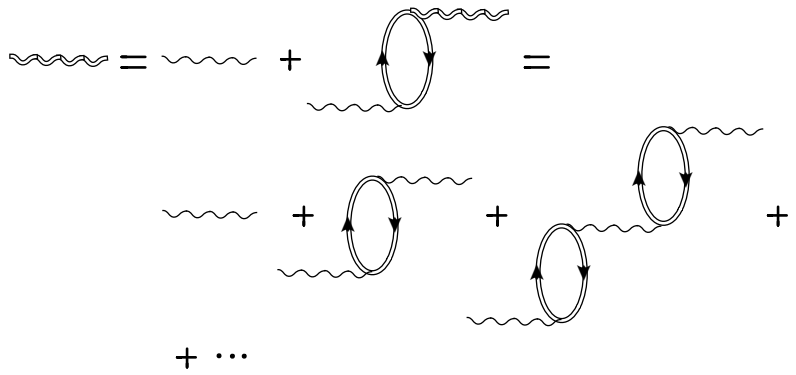

Figure E.4: Screened interaction in the GW approximation is given by geometric series. Bubble diagram represents polarization $\Pi_{\vec{q}}(i\omega_n)$. Double solid (wiggly) line represents dressed Greens function (screened interaction) whereas single wiggly corresponds to bare interaction.

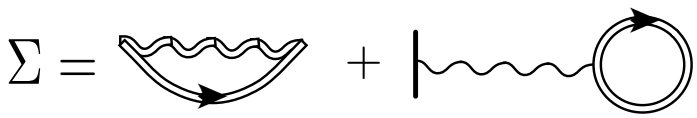

Figure E.5: Self-energy in the GW approximation plus Hartree term.

contribution but as it was already mentioned above this contribution is cancelled by the positive background charge [32]. As one can see the GW approximation has the same form as the Hartree-Fock one (Fig. 7.5) but the latter uses only bare Greens function and potential. This means that the GW approximations takes into account infinitely many diagrams in addition to the Hartree-Fock ones, see Fig. E.6.

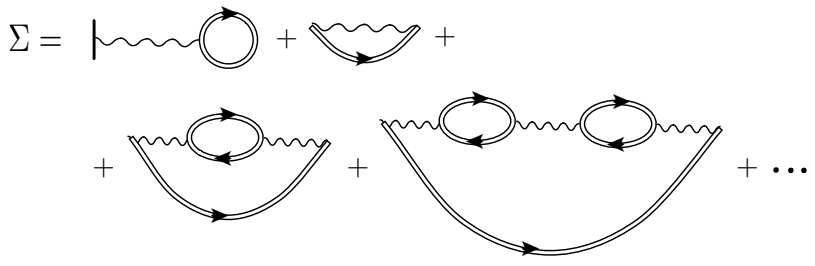

Figure E.6: Diagrammatic expansion of Σ obtained by replacing wiggly line (screened interaction) in Fig. E.5 with the series of diagrams presented in Fig. E.4.

GW approximation in general implies self-consistent calculation: self-energy is calculated using non-interacting Greens function through Eq. E.16, E.17, E.15 and then Greens function is updated using the Dyson equation which is used to calculate the new self-energy. This procedure is repeated until calculation is converged.

Bibliography

[1] N. F. Mott. *Metal-Insulator Transitions.* Taylor & Francis, 1990.

[2] J. Hubbard. Electron correlations in narrow energy bands. *Proc. Roy. Soc. London Ser. A*, 276, 1963.

[3] A. Georges, G. Kotliar W. Krauth, and M. Rozenberg. Dynamical mean-field theory of strongly correlated fermion systems and the limit of infinite dimensions. *Rev. Mod. Phys.*, 68, 1996.

[4] W. Metzner and D. Vollhardt. Correlated lattice fermions in $d = \infty$ dimensions. *Phys. Rev. Lett.*, 62, 1989.

[5] H. J. Vidberg and J. W. Serene. Solving the eliashberg equations by means of n-point padé approximant. *J. Low Temp. Phys.*, 29, 1977.

[6] G. A. Baker. *Essentials of Padé Approximants.* Academic Press, New York, 1975.

[7] R. N. Silver, D. S. Sivia, and J. E. Gubernatis. Maximum-entropy method for analytic continuation of quantum monte carlo data. *Phys. Rev. B*, 41, 1990.

[8] K. S. Novoselov *et al.* Electric field effect in atomically thin carbon films. *Science*, 306, 2004.

[9] S. Das Sarma, Sh. Adam, E. H. Hwang, and E. Rossi. Electronic transport in two-dimensional graphene. *Rev. Mod. Phys.*, 83, 2011.

[10] P. R. Wallace. The band theory of graphite. *Phys. Rev.*, 71, 1947.

[11] J. W. McClure. Band structure of graphite and de haas-van alphen effect. *Phys. Rev.*, 108, 1954.

[12] A. H. castro Neto, F. Guinea, N. M. R. Peres, K. S. Novoselov, and A. K. Geim. The electronic properties of graphene. *Rev. Mod. Phys.*, 81, 2009.

[13] A. K. Geim and K. S. Novoselov. The rise of graphene. *Nature Mater.*, 6, 2007.

[14] G. W. Semenoff. Condensed-matter simulation of a three-dimensional anomaly. *Phys. Rev. Lett.*, 53, 1984.

[15] J. C. Slonczewski and P. R. Weiss. Band structure of graphite. *Phys. Rev.*, 109, 1958.

[16] W. Andreoni. *The Physics of Fullerene-Based and Fullerene-Related Materials*. Springer, Berlin, 2000.

[17] R. Saito, G. Dresselhaus, and M. S. Dresselhaus. *Physical Properties of Carbon Nanotubes*. Imperial college press, London, 1998.

[18] M. Lv and Sh. Wan. Screening-induced transport at finite temperature in bilayer graphene. *Phys. Rev. B*, 81, 2010.

[19] V. N. Kotov, B. Uchoa, V. M. Pereira, F. Guinea, and A. H. Castro Neto. Electron-electron interactions in graphene: Current status ans perspectives. *Rev. Mod. Phys.*, 84, 2012.

[20] T. Ohta *et al.* Controlling the electronic structure of bilayer graphene. *Science*, 313, 2006.

[21] E. V. Castro *et al.* Biased bilayer graphene: Semiconductor with a gap tunable by the electric field effect. *Phys. Rev. Lett.*, 99, 2007.

[22] R. Sensarma, E. H. Hwang, and S. Das Sarma. Quasiparticles, plasmarons, and quantum spectral function in bilayer graphene. *Phys. rev. B*, 84, 2011.

[23] John W. Negele and Henri Orland. *Quantum Many-Particle Systems*. Addison-Wesley, 1988.

[24] G. Baym and N. D. Mermin. Determination of thermodynamic Green's functions. *J. Math. Phys.*, 2, 1961.

[25] J. M. Luttinger and J. C. Ward. Ground-state energy of a many-fermion system. *Phys. Rev. Lett.*, 118:1417–1427, 1960.

[26] G. Baym. *Progress in nonequilibrium Greens functions*. Proceedings of the conference Kadanoff-Baym Equations Progress and Perspectives for Many-body Physics, Rostock Germany, September 1999.

[27] G. Baym and L. P. Kadanoff. Conservation laws and correlation functions. *Phys. Rev.*, 124, 1961.

[28] G. Baym. Self-consistent approximations in many-body systems. *Phys. Rev.*, 127, 1962.

[29] J. J. Sakurai. *Modern Quantum Mechanics*. Addison-Wesley Publishing Company, Inc., 1994.

[30] Xue-Feng Wang and Tapash Chakraborty. Coulomb screening and collective excitations in a graphene bilayer. *Phys. Rev. B*, 75, 2007.

[31] E. McCann and V. Fal'ko. Landau-level degeneracy and quantum hall effect in a graphite bilayer. *Phy. Rev. Lett.*, 96, 2006.

[32] R. D. Mattuck. *A guide to Feynman diagrams in the many-body problem*. 2nd edition, Dover Publications, INC., New York, 1992.

[33] R. O. Jones and O. Gunnarsson. The density functional formalism, its applications and prospects. *Rev. Mod. Phys.*, 61, 1989.

[34] R. M. Dreizler and E. K. U. Gross. *Density Functional Theory*. New York: Springer, 1990.

[35] W. Kohn and L. J. Sham. Self-consistent equations including exchange and correlation effects. *Phys. Rev.*, 140, 1965.

[36] L. Hedin. New method for calculating the one-particle green's function with application to the electron-gas problem. *Phys. Rev.*, 139, 1965.

[37] L. Hedin and S. Lundqvist. *Solid State Physics*. Acedemic Press, INC., 1969.

[38] F. Aryasetiawany and O. Gunnarsson. The gw method. *Rep. Prog. Phys.*, 61, 1998.

[39] U. von Barth and B. Holm. Self-consistent gw_0 results for the electron gas: Fixed screened potential w_0 within the random-phase approximation. *Phys. Rev. B*, 54, 1996.

[40] B. Holm and U. von Barth. Fully self-consistent gw self-energy of the electron gas. *Phys. Rev. B*, 57, 1998.

[41] Th. Ayral, Ph. Werner, and S. Biermann. Spectral properties of correlated materials: Local vertex and nonlocal two-particle correlations from combined gw and dynamical mean field theory. *Phys. Rev. Lett.*, 109, 2012.

[42] Gerald D. Mahan. *Many-Particle Physics*. Plenum Press, New York, 1981.

[43] Q. P. Li and S. Das Sarma. Elementary excitation spectrum of one-dimensional electron systems in confined semiconductor structures: Zero magnetic field. *Phys. Rev. B*, 43, 1991.

[44] T. Ando, A. B. Fowler, and F. Stern. Electronic properties of two-dimensional systems. *Rev. Mod. Phys.*, 54, 1982.

[45] B. I. Lundqvist. Single-particle spectrum of the degenerate electron gas. *Phys. Kondes. Materie.*, 6, 1967.

[46] Paul von Allmen. Plasmaron excitation and band renormalization in a two-dimensional gas. *Phys. Rev. B*, 46, 1991.

[47] J. Nilsson, A. H. Castro Neto, N. Peres, and F. Guinea. Electron-electron interactions and phase diagram of a graphene bilayer. *Phy. Rev. B*, 73, 2006.

[48] A. Botswick, T. Ohta, T. Seyller, K. Horn, and E. Rotenberg. Quasiparticle dynamics in graphene. *Nat. Phys.*, 3, 2007.

[49] A. Bostwick *et al.* Observation of plasmarons in quasi-freestanding doped graphene. *Science*, 328, 2010.

[50] M. Granath, A. Sabashvili anad H. U. R. Strand, and S. Ostlund. Discretized thermal green's functions. *Ann. Phys.*, 524, 2012.

[51] R. Sensarma, E. H. Hwang, and S. Das Sarma. Dynamic screening and low-energy collective modes in bilayer graphene. *Phys. Rev. B*, 82, 2010.

[52] A. Georges and G. Kotliar. Hubbard model in infinite dimensions. *Phys. Rev. B*, 45:6479, 1992.

[53] H.U.R. Strand, A. Sabashvili, M. Granath, B. Hellsing, and S. Ostlund. Dynamical mean field theory phase-space extension and critical properties of the finite temperature mott transition. *Phys. Rev. B*, 83, 2011.

[54] R. Bulla, T. A. Costi, and D. Vollhardt. Finite-temperature numerical renormalization group study of the mott transition. *Phys. Rev. B*, 64, 2001.

[55] M. Capone, L. de'Medici, and A. Georges. Solving the dynamical mean-field theory at very low temperatures using the lanczos exact diagonalization. *Phys. Rev. B*, 72, 2007.

[56] J. Joo and V. Oudovenko. Quantum monte carlo calculation of the finite temperature mott-hubbard transition. *Phys. Rev. B*, 64, 2001.

[57] M. T. Heath. *Scientific Computing An Introductory Survey.* McGraw-Hill Book Company, 2002.

[58] Ning-Hua Tong, Shun-Qing Shen, and Fu-Cho Pu. Mott-hubbard transition in infinite dimensions. *Phys. Rev. B*, 64, 2001.

[59] N. Blumer. *Mott-Hubbard Metal-Insulator Transition and Optical conductivity in High Dimension.* Ph.D. thesis, University of Augsburg, 2002.

[60] M. J. Rozenberg, R. Chitra, and G. Kotliar. Finite temperature mott transition in the hubbard model in infinite dimensions. *Phys. Rev. Lett.*, 83, 1999.

[61] G. Kotliar, E. Lange, and M. J. Rozenberg. Landau theory of the finite temperature mott transition. *Phys. Rev. Lett.*, 84, 2000.

[62] M. J. Rozenberg, G. Kotliar, and X. Y. Zhang. Mott-hubbard transition in infinite dimensions. *Phys. Rev. B*, 49, 1994.

[63] R. Blaschke and R. Blocksdorf. Influence of the inelastic electron-phonon scattering on the superconducting surface resistance. *Z. Phys. B*, 49, 1982.

[64] C. R. Leavens and D. S. Ritchie. Extension of the n-point padé approximants solution of the eliashberg equations to t tc. *Solid State Commun.*, 53, 1985.

[65] F. Marsiglio, M. Schossmann, and J. P. Carbotte. Iterative analytic continuation of the electron self-energy to the real axis. *Phys. Rev. B*, 37, 1988.

[66] J. Schmalian, M. Langer, S. Grabowski, and K.H. Bennemann. Self-consistent summation of many-particle diagrams on the real frequency axis and its application to the flex approximation. *Comput. Phys. Commun.*, 93, 1996.

[67] K. S. Beach, R. J. Gooding, and F. Marsiglio. Reliable padé analytical continuation method based on a high-accuracy symbolic computation algorithm. *Phys. Rev. B*, 61, 2000.

[68] H. S. Wall and M. Wetzel. Contributions to the analytic theory of j-fractions. *Trans. Am. Math. Soc.*, 55, 1944.

[69] C. Karrasch, V. Meden, and K. Schönhammer. Finite-temperature linear conductance from the matsubara Greens function without analytic continuation to the real axis. *Phys. Rev. B*, 82, 2010.

[70] C. Karrasch, R. Hedden, R. Peters, Th. Pruschke, K. Schönhammer, and V. Meden. A finite-frequency functional renormalization group approach to the single impurity anderson model. *J. Phys. Condens. Matter*, 20, 2008.

[71] K. Hartt. Padé approximants, nn scattering, and hard core repulsions. *Phys. Rev. C*, 22, 1980.